Kinematics of Parsec-scale Jets of Gamma-Ray Blazars at 43 GHz during 10 yr of the VLBA-BU-BLAZAR Program

Zachary R. Weaver[1] , Svetlana G. Jorstad[1,2] , Alan P. Marscher[1] , Daria A. Morozova[2] , Ivan S. Troitsky[2] , Iván Agudo[3] ,
José L. Gómez[4] , Anne Lähteenmäki[5,6] , Joni Tammi[5] , and Merja Tornikoski[5]

[1] Institute for Astrophysical Research, Boston University, 725 Commonwealth Avenue, Boston, MA 02215, USA; zweaver@bu.edu
[2] Astronomical Institute, St. Petersburg State University, Universitetskij, Pr. 28, Petrodvorets, St. Petersburg 198504, Russia
[3] Instituto de Astrofísica de Andalucía (IAA), CSIC, Glorieta de la Astronomía s/n, E-18008, Granada, Spain
[4] Instituto de Astrofísica de Andalucía (IAA), CSIC, Apartado 3004, E-18080, Granada, Spain
[5] Aalto University Metsähovi Radio Observatory, Metsähovintie 114, FI-02540 Kylmälä, Finland
[6] Aalto University Department of Electronics and Nanoengineering, P.O. Box 15500, FI-00076, Aalto, Finland
Received 2021 August 25; revised 2022 February 17; accepted 2022 February 23; published 2022 May 4

Abstract

We analyze the parsec-scale jet kinematics from 2007 June to 2018 December of a sample of γ-ray bright blazars monitored roughly monthly with the Very Long Baseline Array (VLBA) at 43 GHz under the VLBA-BU-BLAZAR program. We implement a novel piecewise linear fitting method to derive the kinematics of 521 distinct emission knots from a total of 3705 total intensity images in 22 quasars, 13 BL Lacertae objects, and 3 radio galaxies. Apparent speeds of these components range from $0.01c$ to $78c$, and 18.6% of knots (other than the "core") are quasi-stationary. One-fifth of moving knots exhibit nonballistic motion, with acceleration along the jet within 5 pc of the core (projected) and deceleration farther out. These accelerations occur mainly at locations coincident with quasi-stationary features. We calculate the physical parameters of 273 knots with statistically significant motion, including their Doppler factors, Lorentz factors, and viewing angles. We determine the typical values of these parameters for each jet and the average for each subclass of active galactic nuclei. We investigate the variability of the position angle of each jet over the 10 yr of monitoring. The fluctuations in position of the quasi-stationary components in radio galaxies tend to be parallel to the jet, while no directional preference is seen in the components of quasars and BL Lacertae objects. We find a connection between γ-ray states of blazars and their parsec-scale jet properties, with blazars with brighter 43 GHz cores typically reaching higher γ-ray maxima during flares.

Unified Astronomy Thesaurus concepts: Active galaxies (17); Relativistic jets (1390); Interferometry (808); Blazars (164); Flat-spectrum radio quasars (2163); BL Lacertae objects (158)

Supporting material: figure sets, machine-readable tables

1. Introduction

The ultrarelativistic flow speeds of the jets of some active galactic nuclei (AGNs) strongly affect their observed characteristics through beaming, aberration, and light-travel delays. These physical effects cause the illusion of apparent superluminal motion, greatly enhanced flux densities, and reduced timescales of variability of flux and polarization (e.g., Blandford et al. 1977). Blazars (Angel & Stockman 1980), with their jet directions oriented nearly along our line of sight (e.g., Lister et al. 2016), exhibit the most extreme characteristics of all AGNs. The extraordinary resolution afforded by very long baseline interferometry (VLBI) enables detailed studies of the inner jets of AGNs on distance scales from <1 to >100 pc from the central supermassive black hole. Monitoring programs over at least a decade are able to (1) systematically characterize the long-term variability of the parsec-scale jet, including knot motions, jet wobbling, and precession; (2) reveal the connection between multiwavelength outbursts and multimessenger events in the jet; and (3) provide an observational basis for theoretical models of jet formation, acceleration, and collimation.

Most blazar jets feature "knots" of emission that travel away from a (presumed stationary) "core" at apparent speeds that range from $\lesssim 1c$ to $\gtrsim 50c$ (e.g., Lister et al. 2016; Jorstad et al. 2017). In a number of blazars, the jets are observed (in projection) to undergo rapid swings of position angle in their innermost regions, but remain collimated on kiloparsec scales (for a review of several sources, see Agudo 2009). The projected jet position angles can vary considerably (by up to 150° over a 12–16 yr time span; Lister et al. 2013). Monotonic swings with no apparent periodicity ("wobbles") have been reported in some objects (e.g., Jorstad et al. 2004; Agudo et al. 2007, 2012), while precession (sinusoidal variations) has been claimed in others (e.g., Stirling et al. 2003; Bach et al. 2005; Lobanov & Roland 2005; Savolainen et al. 2006; Marti-Vidal et al. 2013; Britzen et al. 2018, 2019). The origin of the wobbles and precession is not well understood, but the presence of such changes in only the innermost (parsec-scale) regions of the jet implies that the causal mechanisms are related to the origin of the jet, e.g., accretion disk precession (e.g., McHardy et al. 1990; Conway & Wrobel 1995; Villata & Raiteri 1999; Britzen et al. 2005, 2017; Perucho et al. 2012; Fromm et al. 2013; Larionov et al. 2013; Raiteri et al. 2017, 2021), instabilities in the jet flow (e.g., Nakamura et al. 2001; Moll et al. 2008; Mignone et al. 2010; Liska et al. 2018), or interactions in a binary supermassive black hole system (e.g., Britzen et al. 2018; Qian et al. 2019).

In order to understand the physical processes in blazars, it is important to relate changes observed in the radio jet to multiwavelength variability and outbursts. Connections between the high-energy emission and radio jets of AGNs have been theorized for ~40 yr (e.g., Königl 1981; Marscher 1987), with observational evidence provided by joint radio and γ-ray studies, the latter based on data from the Compton Gamma Ray Observatory (Hartman et al. 1999). The results have highlighted the dichotomy between blazar subclasses. In the traditional AGN unification scheme (Urry & Padovani 1995), flat-spectrum radio quasars (FSRQs) and BL Lacertae objects (BL Lac objects) are differentiated by their optical properties and radio morphology (e.g., Wardle et al. 1984). During the Compton era, FSRQs were found to have higher γ-ray fluxes when they also exhibited high optical polarization and a high-radio-frequency outburst (Valtaoja & Terasranta 1995). There was no similarly clear correlation between the γ-ray emission in BL Lac objects and their radio variations (Lähteenmäki & Valtaoja 2003). For both subtypes, however, there existed a correlation between the brightness of the radio "core" and γ-ray flux (Jorstad et al. 2001b), as well as a connection between the ejections of superluminal radio knots and γ-ray outbursts (Jorstad et al. 2001a).

The Fermi Large Area Telescope (LAT) has ushered in a new era of γ-ray-radio studies. Individual sources show a wide variety of behavior during major γ-ray events. The typical duration of a high γ-ray state in blazars is several months (Williamson et al. 2014), although shorter-timescale fluctuations are often observed (e.g., Agudo et al. 2011a; Weaver et al. 2019, 2020). The majority of these γ-ray and very-high-energy (⩾100 GeV) outbursts can be connected with the propagation of a knot through the core or other quasi-stationary components in the parsec-scale radio jet (e.g., Marscher et al. 2010; Agudo et al. 2011a; Casadio et al. 2015; Liodakis et al. 2020; H. E. S. S. Collaboration et al. 2021; MAGIC Collaboration et al. 2021). Two major issues exist with this model for blazar flares: the presence of "orphan" γ-ray flares (e.g., Krawczynski et al. 2004; MacDonald et al. 2015) with no counterparts at longer wavelengths, and the need for an intense external photon field at these locations in the jet (e.g., Aleksić et al. 2011; Joshi et al. 2014), the source of which is unknown. Emission-line flares with short time delays relative to the γ-ray outburst have also been observed in several blazars (León-Tavares et al. 2013; Larionov et al. 2020; Hallum et al. 2022), which could provide additional seed photons (Isler et al. 2015; León-Tavares et al. 2015; Larionov et al. 2020). Detection of a 290 TeV neutrino with a direction of origin coincident with the flaring blazar TXS 0506+056 (IceCube Collaboration et al. 2018a, 2018b), suggests an association between flaring blazars and high-energy neutrinos (e.g., Murase et al. 2018; Rodrigues et al. 2018). Thus, blazar jets may produce high-energy hadronic cosmic-rays (e.g., Keivani et al. 2018; Cerruti et al. 2019) alongside electromagnetic outbursts and changes in the parsec-scale structure (for discussion of the parsec-scale jet of TXS 0506+056, see Li et al. 2020).

VLBI observations can also provide constraints on theoretical models of AGN jet launching, acceleration, and collimation, which are challenging to model. The launching mechanism in AGNs can be ascribed to one (or both) of two processes. The Blandford–Znajek mechanism (Blandford & Znajek 1977) utilizes the rotational energy of the black hole, with the spin of the black hole winding up the magnetic field

lines anchored to the event horizon, resulting in a relativistic Poynting flux dominated jet (e.g., Beskin & Kuznetsova 2000; Komissarov 2001, 2005; Tchekhovskoy et al. 2010). Alternatively, magnetic field lines anchored to the accretion disk can launch mildly relativistic mass-dominated winds (Blandford & Payne 1982). One of the primary goals of VLBI monitoring programs of blazar jets is to provide an observational framework for comparing numerical simulations of jets (e.g., Vlahakis & Königl 2003; Komissarov 2005; Lyubarsky 2009; Meier 2012; Pu et al. 2015; Chatterjee et al. 2019) with the actual parsec-scale behavior.

A number of observing programs follow time changes in the jets of a large number of blazars. The largest has monitored several hundred of the brightest AGNs in the northern sky, first under the 2 cm VLBA survey (Kellermann et al. 1998), and later as part of the MOJAVE[7] program. Lister et al. (2019) found that 60% of the 409 monitored sources exhibit acceleration of emission features in the jet. Other than a few outliers, the 15 GHz emission features have a distribution of apparent velocities that fall within ±40% of the median speed of a given source. No jet features are reported to have a bulk Lorentz factor $\Gamma > 50$. Through Monte Carlo modeling of the parent population, the authors show that the data are consistent with a jet population that has a simple unbeamed power-law luminosity function incorporating pure luminosity evolution, and a power-law Lorentz factor distribution ranging from 1.25 to 50, with a slope -1.4 ± 0.2.

The Boston University group and its collaborators have been monitoring blazar jets with the VLBA at 43 GHz since 1993. The research focuses on the connection between jet properties and multiwavelength behavior. This includes analysis of events in the jets of γ-ray blazars during the Compton era (Jorstad et al. 2001b), accretion disk-jet associations (Marscher et al. 2002; Chatterjee et al. 2011), and relations between optical and millimeter-wave linear polarization (Jorstad et al. 2005). Over the past 10 yr, we have been monitoring the jet kinematics of a sample of 38 blazars at a roughly monthly cadence at 43 GHz under the VLBA-BU-BLAZAR program.[8] For comparison with the longer-wavelength data, we obtain well-sampled γ-ray light curves from the Fermi LAT. The higher observing frequency relative to other VLBA monitoring programs allows emission features to be tracked closer to the "core" of the sources. Also, the more frequent monitoring allows faster, shorter-lived features to be observed. Based on the first 5 yr of data, we found that nearly one-third of moving knots show evidence of acceleration in the jet (Jorstad et al. 2017). Furthermore, knots in FSRQs tend to have higher Doppler and Lorentz factors, with smaller viewing and opening angles, than the knots in BL Lac objects and radio galaxies (RGs). A number of radio jet–γ-ray event associations have been detected using these data (Marscher et al. 2010; Agudo et al. 2011a, 2011b; Wehrle et al. 2012; Jorstad et al. 2013; Jorstad & Marscher 2016; Casadio et al. 2015; Larionov et al. 2020; H. E. S. S. Collaboration et al. 2021; MAGIC Collaboration et al. 2021).

In this paper, we provide the data and detailed analyses of the parsec-scale jet behavior of a sample of γ-ray bright AGNs over our decade-long monitoring program, VLBA-BU-BLA-ZAR. We implement a new piecewise linear fitting method to

---

determine the jet kinematics. For consistency, we reanalyze previously published data to produce a uniform data set that covers the first 10.5 yr of VLBA monitoring associated with Fermi LAT observations, 2007 June to 2018 December. The paper is structured as follows. In Section 2, we detail the observations, their calibration, and analysis from 2013 January through 2018 December, and describe the piecewise fitting of the core-knot separations versus time that we apply to all of the data. The data for individual knots and sources are available in Tables 2 and 3. The parsec-scale jet structure and the behavior of the jet position angle with time (Table 7) of each source are discussed in Section 3. Section 4 describes the moving/ stationary features (Tables 8 and 9) and accelerations (Table 10) of all knots in our sample. We determine the statistically robust physical parameters of knots in our sample in Section 5 (Table 12), and provide estimates for the "typical" physical parameters of each jet (Table 13). We briefly discuss connections between millimeter-wave and γ-ray states of the AGNs in Section 6. A summary of our findings is given in Section 7. Throughout this work, we assume a standard Λ cold dark matter cosmology with rounded values of cosmological parameters based on those obtained by the Planck collaboration (Planck Collaboration et al. 2020), the results from type Ia supernova studies (Riess et al. 2016), and VLT-KMOS data (González-Morán et al. 2021): $H_\circ = 70\ \mathrm{km\ s^{-1}\ Mpc^{-1}}$, $\Omega_m = 0.3$, and $\Omega_\Lambda = 0.7$.

2. Observations and Data Analysis

As part of the VLBA-BU-BLAZAR monitoring program, we have obtained roughly monthly observations with the VLBA at 43 GHz (7 mm wavelength) of a sample of AGNs detected as γ-ray sources. The results of the observations from 2007 June to 2013 January have been presented in Jorstad et al. (2017). In this work, we extend the analyzed period with observations obtained from 2013 January through 2018 December, bringing the total monitoring period to 10.5 yr. In order to interpret the results of our study more consistently, we apply a new formalism (described below) to the entire data set to calculate the knot motions and kinematic parameters.

The sample studied here consists of a total of 38 sources, of which 22 are FSRQs, 13 are BL Lac objects, and three are RGs. Each source has been detected at γ-ray energies by the Fermi LAT (Abdo et al. 2010; Acero et al. 2015), with an average flux density at 43 GHz exceeding 0.5 Jy, a decl. north of $-30°$, and an optical magnitude in the R band brighter than $18\overset{\mathrm{m}}{.}5$. The original sample is described in Jorstad et al. (2017). Several additional sources that have been revealed to have occasionally strong γ-ray flux (as observed with the Fermi-LAT) and sufficiently high optical flux to meet the selection criteria have been included in the current sample.

The observations of the sample were performed roughly monthly via dynamical scheduling, over a 24 hr period at each epoch, using all available VLBA antennas. (At some epochs, 1–2 antennas could not collect data owing to technical problems or weather conditions.) A total of 32 or 33 objects were observed during each epoch, with 40–45 minutes integration time per source (8–9 scans of $\sim$5 minutes duration), spread over the 6–10 hr time span with the optimal visibility of the object. Eight sources were observed during alternating sessions; these objects are in crowded R.A. ranges and exhibit relatively long timescales of variability of the jet structure at 43 GHz. Although the observations and data processing were

carried out in a similar manner as in Jorstad et al. (2017), with the latter using the Astronomical Image Processing System (AIPS; van Moorsel et al. 1996), some details were different. A new data recording system (Mark5C) was installed, allowing a data recording rate of 2048 Mb per second, as opposed to the previous rate of 512 Mb per second. The resulting increase in data quality allows a sufficient signal-to-noise ratio to be achieved without averaging intermediate frequency bands (IFs). Thus, since 2014 February, the final calibrated data available on the project website include visibilities at four IFs (centered at 43.0075, 43.0875, 43.1515, and 43.2155 GHz). We have calibrated the instrumental polarization separately for each IF.

We have continued to monitor the optical $BVRI$ photometric brightness and R-band linear polarization of the sample at the 1.83 m Perkins Telescope (Boston University,[9] Flagstaff, Arizona) over $\sim$1 week time intervals during dark/gray lunar phases. One such session occurred during most months.

Table 1 gives a list of the monitored sources, along with their characteristics: 1—name based on B1950 coordinates; 2—common name; 3—subclass of blazar; 4—redshift, z, according to the NASA Extragalactic Database;[10] 5—average total intensity at 37 GHz, $\langle S_{37} \rangle$, and its standard deviation as observed with the Metsähovi Radio Observatory of Aalto University, Finland, between 2007 January and 2018 December; 6—average γ-ray photon flux at 0.1–200 GeV, $\langle S_\gamma \rangle$, and its standard deviation based on the γ-ray light curve of each source, calculated from the photon and spacecraft data provided by the Fermi Space Science Center (for details, see Williamson et al. 2014) between 2007 January and 2018 December; and 7—average R-band magnitude, $\langle S_R \rangle$ and its standard deviation according to our observations at the Perkins Telescope between 2007 January and 2018 December.

2.1. Total Intensity Image Modeling

The parsec-scale jet morphology of blazars features a "core" (e.g., Jorstad et al. 2001b, 2005, 2017; Kellermann et al. 2004; Lister et al. 2013, 2018), an assumed stationary feature located at the upstream end of the jet seen in the VLBI images. For most sources, the core is usually the brightest feature in the jet (Jorstad et al. 2017), but sometimes in some blazars an emission component downstream of the core can be more prominent (e.g., 2251+158; Jorstad et al. 2001b). The exact location of this core relative to the central black hole is frequency dependent as the core represents the region where the jet becomes optically thick at a given frequency, with VLBI at higher frequencies being able to image closer to the black hole (see, e.g., O'Sullivan & Gabuzda 2009; Event Horizon Telescope Collaboration et al. 2019). One or more "knots" of emission are often observed downstream of the core (e.g., Jorstad et al. 2001b). Some of these are quasi-stationary, without systematic motions relative to the core, while others move down the jet, in most cases at apparent superluminal speeds (e.g., Cohen et al. 1971, 1977; Jorstad et al. 2001b, 2017; Lister et al. 2018).

In order to represent the total intensity structure of each source at each epoch, we model the frequency-averaged visibility data with a series of circular Gaussian components that best fit the data. The model fitting involves iterations of the

---

[9] Operated by Lowell Observatory prior to 2019.
[10] https://ned.ipac.caltech.edu/

Table 1
The VLBA-BU-BLAZAR Sample

Source	Name	Type	z	$\langle S_{37} \rangle$ (Jy)	$\langle S_\gamma \rangle$ (10^{-8} ph cm^{-2} s^{-1})	$\langle S_R \rangle$ (mag)
(1)	(2)	(3)	(4)	(5)	(6)	(7)
0219+428[a]	3C 66A	BL	0.444[b]	0.71 ± 0.24	10.81 ± 12.86	14.40 ± 0.42
0235+164	A0 0235+16	BL	0.940[b]	1.99 ± 1.16	11.77 ± 14.91	17.45 ± 0.98
0316+413[c]	3C 84	RG	0.0176	26.11 ± 4.57	35.54 ± 20.40	12.82 ± 0.14
0336−019	CTA 26	FSRQ	0.852	2.24 ± 0.56	12.34 ± 10.13	16.86 ± 0.52
0415+379	3C 111	RG	0.0485	4.06 ± 2.13	7.43 ± 4.68	17.38 ± 0.22
0420−014	OA 129	FSRQ	0.916	4.11 ± 2.14	7.68 ± 5.18	17.50 ± 0.78
0430+052[d]	3C 120	RG	0.033	3.40 ± 1.64	5.43 ± 4.84	13.90 ± 0.13
0528+134	PKS 0528+13	FSRQ	2.060	1.84 ± 1.20	8.85 ± 9.93	19.38 ± 0.27
0716+714	S5 0716+71	BL	0.3[b]	2.44 ± 1.19	20.78 ± 14.67	13.19 ± 0.63
0735+178	PKS 0735+17	BL	0.424	0.77 ± 0.23	6.21 ± 11.77	15.98 ± 0.47
0827+243	OJ 248	FSRQ	0.939	1.23 ± 0.61	6.87 ± 11.26	16.91 ± 0.39
0829+046	OJ 049	BL	0.182	0.83 ± 0.37	6.53 ± 3.93	15.52 ± 0.38
0836+710	4C+71.07	FSRQ	2.172	2.12 ± 0.69	13.91 ± 19.40	16.60 ± 0.09
0851+202	OJ 287	BL	0.306	5.94 ± 2.20	9.08 ± 7.46	14.37 ± 0.49
0954+658	S4 0954+65	BL	0.368[b]	1.19 ± 0.40	10.87 ± 20.24	15.58 ± 0.96
1055+018[a]	4C+01.28	FSRQ[e]	0.890	5.22 ± 1.36	9.91 ± 5.72	15.92 ± 0.83
1101+384[c]	Mkn 421	BL	0.030	0.49 ± 0.16	17.83 ± 9.50	12.41 ± 0.39
1127−145	PKS 1127−14	FSRQ	1.184	…	6.80 ± 5.05	16.74 ± 0.18
1156+295	4C+29.45	FSRQ	0.729	2.08 ± 0.83	16.51 ± 21.60	15.71 ± 1.00
1219+285	WCom	BL	0.102	0.41 ± 0.16	6.29 ± 2.65	15.26 ± 0.37
1222+216	4C+21.35	FSRQ	0.435	1.98 ± 0.61	33.62 ± 55.61	15.10 ± 0.43
1226+023	3C 273	FSRQ	0.158	17.76 ± 4.58	29.03 ± 40.00	12.63 ± 0.13
1253−055	3C 279	FSRQ	0.538	19.00 ± 5.31	66.30 ± 117.31	15.02 ± 0.66
1308+326	B2 1308+32	FSRQ	0.998	1.74 ± 0.72	5.25 ± 4.24	18.03 ± 0.83
1406−076	PKS 1406−07	FRSQ	1.494	0.94 ± 0.26	6.54 ± 10.19	18.28 ± 0.42
1510−089	PKS 1510−08	FSRQ	0.361	3.31 ± 1.25	96.60 ± 120.47	15.88 ± 0.53
1611+343	DA 406	FSRQ	1.40	3.11 ± 0.71	5.25 ± 2.44	17.31 ± 0.21
1622−297[f]	PKS 1622−29	FSRQ	0.815	…	12.09 ± 7.57	18.18 ± 0.25
1633+382	4C+38.41	FSRQ	1.814	3.78 ± 1.39	30.31 ± 30.63	16.68 ± 0.63
1641+399	3C 345	FSRQ	0.595	5.83 ± 1.16	9.22 ± 5.83	17.15 ± 0.46
1652+398[g]	Mkn 501	BL	0.034	0.93 ± 0.17	5.27 ± 2.38	13.26 ± 0.09
1730−130	NRAO 530	FSRQ	0.902	3.47 ± 0.94	11.96 ± 9.99	17.63 ± 0.38
1749+096[a]	OT 081	BL	0.322	3.82 ± 1.21	8.89 ± 12.39	16.49 ± 0.52
1959+650[h]	1ES 1959+65	BL	0.047	0.32 ± 0.14	5.13 ± 3.29	14.24 ± 0.25
2200+420	BL Lac	BL	0.069	4.46 ± 2.47	40.48 ± 25.08	13.64 ± 0.56
2223−052	3C 446	FSRQ	1.404	3.80 ± 2.00	5.02 ± 2.89	18.09 ± 0.35
2230+114	CTA 102	FSRQ	1.037	3.50 ± 0.89	118.81 ± 185.75	15.65 ± 1.04
2251+158	3C 454.3	FSRQ	0.859	17.01 ± 7.72	206.62 ± 337.67	15.02 ± 0.79

Notes.
[a] Source added to the sample in 2009.
[b] Redshift has not been confirmed.
[c] Source added to the sample in 2010.
[d] Source added to the sample in 2012.
[e] Classified as a BL object in Jorstad et al. (2017).
[f] Removed from the sample after 2017 July.
[g] Source added to the sample in 2014.
[h] Source added to the sample in 2017.

MODELFIT task within the Difmap (Shepherd 1997) software package. We use the term "knot" to refer to these Gaussian components, which correspond to a (usually) compact feature of enhanced brightness in the jet. Initially, a single circular Gaussian component approximating the brightness distribution of the core is used, then knots are added at the approximate locations of bright features identified in the image. Each addition of a knot is followed by hundreds of iterations with MODELFIT to determine the parameters of the knot that yield the best agreement between the model and uv data, according to a χ^2 test. The knot parameters that we fit are: S—flux density;

$R_{\rm obs}$—distance with respect to the core; $\Theta_{\rm obs}$—relative position angle (P.A.) with respect to the core, measured north through east; and a—the angular size of the knot, corresponding to the FWHM of the circular Gaussian component. The iterative process of adding knots is ended when the addition of a new knot does not significantly improve the χ^2 value of the model. Often, the model of a previous epoch is used as the starting model for the next epoch for a given source, as we assume that the jet does not drastically change structure between our roughly monthly observations. We utilize the previously published Difmap models of each source at each epoch from

Table 2
Modeling of Jets by Gaussian Components 2013–2018

Source	χ^2	rms	Epoch (yr)	MJD	$S \pm \sigma_S$ (Jy)	$R \pm \sigma_R$ (mas)	$\Theta \pm \sigma_\Theta$ (deg)	$a \pm \sigma_a$ (mas)	$T_{b,\mathrm{obs}}$ ($\times 10^8$ K)
(1)	(2)	(3)	(4)	(5)	(6)	(7)	(8)	(9)	(10)
0219+428	1.131	0.050	2013.038	56307	0.129 ± 0.009	0.000	0.0	0.020 ± 0.009	2418.8L
			2013.038	56307	0.071 ± 0.010	0.084 ± 0.030	-165.0 ± 5.8	0.081 ± 0.022	81.2
			2013.038	56307	0.044 ± 0.012	0.391 ± 0.099	-157.1 ± 4.6	0.183 ± 0.037	9.9
			2013.038	56307	0.025 ± 0.014	0.737 ± 0.296	-176.0 ± 5.8	0.329 ± 0.057	1.7
			2013.038	56307	0.031 ± 0.015	2.396 ± 0.443	-177.8 ± 2.7	0.512 ± 0.067	0.9
0219+428	0.792	0.035	2013.288	56398	0.203 ± 0.013	0.000	0.0	0.053 ± 0.013	542.0
			2013.288	56398	0.047 ± 0.011	0.149 ± 0.060	-161.5 ± 6.8	0.122 ± 0.029	23.7
			2013.288	56398	0.030 ± 0.011	0.448 ± 0.098	-160.4 ± 3.8	0.148 ± 0.036	10.3
			2013.288	56398	0.021 ± 0.015	0.843 ± 0.613	-169.4 ± 11.1	0.558 ± 0.077	0.5
			2013.288	56398	0.025 ± 0.014	2.474 ± 0.372	-177.3 ± 2.2	0.398 ± 0.062	1.2

Note. Values of $T_{b,\mathrm{obs}}$ denoted by the letter "L" represent the lower limits to the brightness temperature; see Section 2.1 for details.

(This table is available in its entirety in machine-readable form.)

2007 June to 2012 December (Jorstad et al. 2017). In this work we provide models for each source from 2013 January to 2018 December.

The uncertainties of the model parameters were calculated using the formalism described in Jorstad et al. (2017), which is based on an empirical relation between the uncertainties and the brightness temperatures of knots, $T_{b,\mathrm{obs}} = 7.5 \times 10^8 S/a^2$ K (e.g., Jorstad et al. 2005; Casadio et al. 2015). Estimates of the errors in each model parameter are as follows: $\sigma_X \approx 1.3 \times 10^4\, T_{b,\mathrm{obs}}^{-0.6}$, $\sigma_Y \approx 2\sigma_X$, $\sigma_S \approx 0.09\, T_{b,\mathrm{obs}}^{-0.1}$, and $\sigma_a \approx 6.5\, T_{b,\mathrm{obs}}^{-0.25}$. Here, σ_X and σ_Y are the 1σ uncertainties in R.A. and decl. in milliarcseconds, σ_S is the uncertainty in the flux density in janskys, and σ_a the uncertainty in component size in milliarcseconds. Note that the typical north–south synthesized beam is $\sim 2\times$ the typical east–west beam size, which increases the uncertainty in decl. As in Jorstad et al. (2017), we have also added a minimum positional error of 0.005 mas (related to the resolution of the observations) and a typical amplitude calibration error of 5% to these uncertainties.

Table 2 gives the total intensity jet models and brightness temperature values for all components in the jet of each source from 2013 January to 2018 December as follows: 1—source name according to its B1950 coordinates; 2—χ^2 value of the model fit; 3—rms difference between the observed and model visibilities; 4—epoch of the start of the observation; 5—MJD of the start of the observation; 6—the flux density, S, and its uncertainty σ_S, in janskys; 7—distance with respect to the core, R_{obs}, and its uncertainty σ_R, in milliarcseconds; 8—position angle of the knot with respect to the core, Θ_{obs}, and its uncertainty σ_Θ, measured north through east in degrees; 9—angular size of the knot, a, and its uncertainty σ_a, in milliarcseconds; and 10—observed brightness temperature $T_{b,\mathrm{obs}}$, in units of 10^8 K. The core at each epoch is located at position $(X, Y) = (0, 0)$, where X is the relative R.A. and Y is the relative decl., and X and Y are related to R_{obs} and Θ_{obs} through $R_{\mathrm{obs}} = \sqrt{X^2 + Y^2}$ and $\tan \Theta_{\mathrm{obs}} = X/Y$. For 9.8% of knots, the model fit yielded a size less than 0.02 mas. This angular size is too small to be resolved on the longest VLBA baselines. Thus, lower limits to $T_{b,\mathrm{obs}}$ for these knots are calculated using $a = 0.02$ ($\sim 20\%$ of the resolution of the longest baselines) and denoted by "L" in Column 10 of Table 2. The total intensity jet models and brightness temperature values for all components in

the jet of each source from 2007 June to 2012 December can be found in Table 2 of Jorstad et al. (2017).

2.2. Identification of Components and Calculation of Apparent Speed

As discussed above, the VLBI "core" is defined as the bright, compact (either unresolved or partially resolved) emission feature at the upstream end of the jet, relative to which the positions of all other components are measured. To identify components, we make use of the fact that all four model parameters (S, R_{obs}, Θ_{obs}, and a) should not change abruptly with time given the regularity of our observations. If a knot is identified at $N \geqslant 4$ epochs, it is assigned a kinematic classification and identification number (ID).

Previous studies (e.g., Homan et al. 2015; Jorstad et al. 2017) have found that a given knot can exhibit both acceleration and deceleration as it propagates down the jet. In order to describe the locations along the jet of such regions of changing velocity, we have created a new formalism for the calculation of kinematic parameters of a knot, utilizing piecewise linear fits to separation (from the core) versus time data instead of polynomial fits as used in Jorstad et al. (2017). This simplifies the calculation of kinematic parameters by describing the motion in terms of the mean velocity of each segment of time within which the velocity is roughly constant and significantly different from that of other segments. This allows us to estimate the distance down the jet at which acceleration occurs. The new procedure consists of the following steps:

1. *Piecewise Linear Fits to X and Y:* We start with the assumption that knots detected at $N \geqslant 4$ epochs can have their X and Y positions fit by a linear trend of the form

$$X(t_i) = a_0 + a_1(t_i - t_{\mathrm{mid}}) \qquad (1)$$

and

$$Y(t_i) = b_0 + b_1(t_i - t_{\mathrm{mid}}), \qquad (2)$$

where t_i is the epoch of observation, $i = 1, \ldots, N$, and $t_{\mathrm{mid}} \equiv (t_N + t_1)/2$. We use the statsmodels package[11] (Seabold & Perktold 2010) weighted least-squares program to calculate the best-fit parameters and

---

[11] https://www.statsmodels.org/stable/index.html

reduced χ^2 value of the fit. These fit χ^2 values are then compared to the critical χ^2_{crit}, corresponding to a significance level of $\zeta = 0.05$ for $f = N - 2$ degrees of freedom (Bowker & Lieberman 1972). If $\chi^2 < \chi^2_{\text{crit}}$, our assumption was valid. However, if the opposite is true, the knot may be experiencing acceleration in the jet and a more complicated fit is necessary. In such cases, we use the `pwlf` package[12] to perform a weighted least-squares piecewise linear fit to the data (Jekel & Venter 2019). The advantage of such a fit over higher-order polynomial fits is that it relies on simple linear fits for segments of the data, so that there are no concerns about over-fitting the data or estimating kinematic parameters from higher-order fits.

We define the piecewise fits in this work in terms of the number of line segments present for each coordinate of motion X and Y. A single-segment fit describes the simple linear case as defined above. A two-segment fit indicates that the motion can be described by two different speeds with a single acceleration region at particular break point, t_b, and a three-segment fit indicates three speeds and two acceleration regions and break points. In a two-segment fit, there are five free parameters, while in a three-segment fit, there are eight free parameters. A piecewise fit with the fewest number of segments for which $\chi^2 \leqslant \chi^2_{\text{crit}}$ is used to fit the data, where χ^2_{crit} is the χ^2 value corresponding to a significance level of $\zeta = 0.05$ for $f = N - \ell$, where ℓ is the number of fit parameters. However, a two-segment fit is only used if $N > 8$, and a three-segment fit is only used if $N > 15$, given the number of degrees of freedom. In cases for which the χ^2 criterion is not reached for even a three-segment piecewise fit, we use the simplest fit that adequately describes the data (χ^2 closest to χ^2_{crit}). There are only several such cases. In some cases, the X and Y motion break points can overlap in time, generally defined as $|t_{b,X} - t_{b,Y}| \leqslant 0.25$ yr. In these situations we average $t_{b,X}$ and $t_{b,Y}$ and use this average time as a single break point. The model fit is then re-run with the break times frozen to the averaged values. The overlap value of 0.25 yr was chosen because in any time interval $\Delta t = 0.25$ yr, our roughly monthly observations will lead to only two or three observations within the time interval so that a calculation of the speed of such a segment is unreliable. The uncertainties of all best-fit parameters are calculated from the diagonals of the covariance matrices of the fits.

2. *Calculation of the Epoch of Ejection*, $t_\circ$: The epoch of ejection is defined as the time when the centroid of a knot coincides with the centroid of the core, with the knot motion extrapolated back to $(X, Y) = (0, 0)$. In general, all observations of the motion of a knot are important for calculating its kinematic parameters. However, for determining $t_\circ$, the most important observations are when the knot is closest to the core, before any potential acceleration. We thus extrapolate the linear fits to X and Y back to $(0, 0)$ from the first identified break point (or use the first ten observations of a knot in the case of no acceleration). This extrapolation provides the time of ejection along each coordinate, $t_{x\circ}$ and $t_{y\circ}$. We then

calculate the true time of ejection as:

$$t_\circ = \frac{t_{x\circ} / \sigma^2_{t_{x\circ}} + t_{y\circ} / \sigma^2_{t_{y\circ}}}{1 / \sigma^2_{t_{x\circ}} + 1 / \sigma^2_{t_{y\circ}}}. \tag{3}$$

Here, the 1σ propagated uncertainties in $t_{x\circ}$ and $t_{y\circ}$ are defined as $\sigma_{t_{x\circ}}$ and $\sigma_{t_{y\circ}}$, respectively. The uncertainty in $t_\circ$ is then calculated as

$$\sigma_{t_\circ} = \sqrt{\frac{(t_\circ - t_{x\circ})^2 / \sigma^2_{t_{x\circ}} + (t_\circ - t_{y\circ})^2 / \sigma^2_{t_{y\circ}}}{1 / \sigma^2_{t_{x\circ}} + 1 / \sigma^2_{t_{y\circ}}}}. \tag{4}$$

For a few cases, weighting $t_{x\circ}$ and $t_{y\circ}$ by uncertainties does not provide a robust solution since they are significantly different from each other, a situation that we define as $|t_{x\circ} - t_{y\circ}| \geqslant 0.5$ yr. This often occurs in the case of knot motion directly along the X- or Y-axis or for knots whose ejections occurred before our monitoring. In such cases, we construct a best-fit linear trend to the R coordinate (either the first ten epochs of observation in the case of purely linear motion or the first segment of motion for knots showing acceleration) and find $t_\circ$ as its root, with its corresponding uncertainty. To each uncertainty in $t_\circ$, regardless of calculation method, we add a minimum uncertainty of $0.005 / \mu$ yr, where 0.005 mas is the size of half a pixel in the VLBA images, and μ is the proper motion of the component (defined below), in milliarcseconds per year. This minimum error is typically $\sim$3–4 days and is generally much less than the error computed as indicated above.

3. *Calculation of Apparent Speeds:* Based on the piecewise linear fits that best fit the X and Y data, we calculate the proper motion μ, direction of motion Φ, and apparent speed β_{app} for each time segment. We continue to define the speed and direction of the motion as in Jorstad et al. (2005), with $\langle \mu_j \rangle = \sqrt{\langle \mu_{x,j} \rangle^2 + \langle \mu_{y,j} \rangle^2}$ and $\langle \Phi_j \rangle = \tan^{-1}(\langle \mu_{x,j} \rangle / \langle \mu_{y,j} \rangle)$, where the subscript j indicates the number of the line segment. As the motion in each coordinate X and Y can be described independently by up to three linear segments, the maximum range of $j = 1, 2, ..., 5$. We arrange the break points chronologically.

4. *Calculation of Apparent Accelerations:* If $j \neq 1$, there is a change in the speed and direction of motion of the knot over time as it moves down the jet. In the case of two or more line segments, we define a region in time between the mid-points of the line segments as the "acceleration region," Δt. While the acceleration may occur over a shorter or longer time period than this midpoint definition, using the mid-points of a segment to determine Δt characterizes the acceleration without a priori knowledge of the cause of acceleration. The acceleration along each coordinate X and Y is defined as $\dot{\mu}_x = \Delta \mu_x / \Delta t$ and $\dot{\mu}_y = \Delta \mu_y / \Delta t$. Then the total acceleration parallel, $\dot{\mu}_{\parallel}$, and perpendicular, $\dot{\mu}_{\perp}$, to the jet axis can be calculated through $\dot{\mu}_{\parallel} = \dot{\mu}_x \sin\langle \Theta_{\text{jet}} \rangle + \dot{\mu}_y \cos\langle \Theta_{\text{jet}} \rangle$ and $\dot{\mu}_{\perp} = \dot{\mu}_x \cos\langle \Theta_{\text{jet}} \rangle - \dot{\mu}_y \sin\langle \Theta_{\text{jet}} \rangle$, where $\langle \Theta_{\text{jet}} \rangle$ is the average jet direction. How we calculate the average jet direction for each source is discussed in Section 3.2.

To interpret the results of the jet kinematics in a uniform manner across 10 yr of observation, we have applied the above method to all of the knots presented in Jorstad et al. (2017), in

---

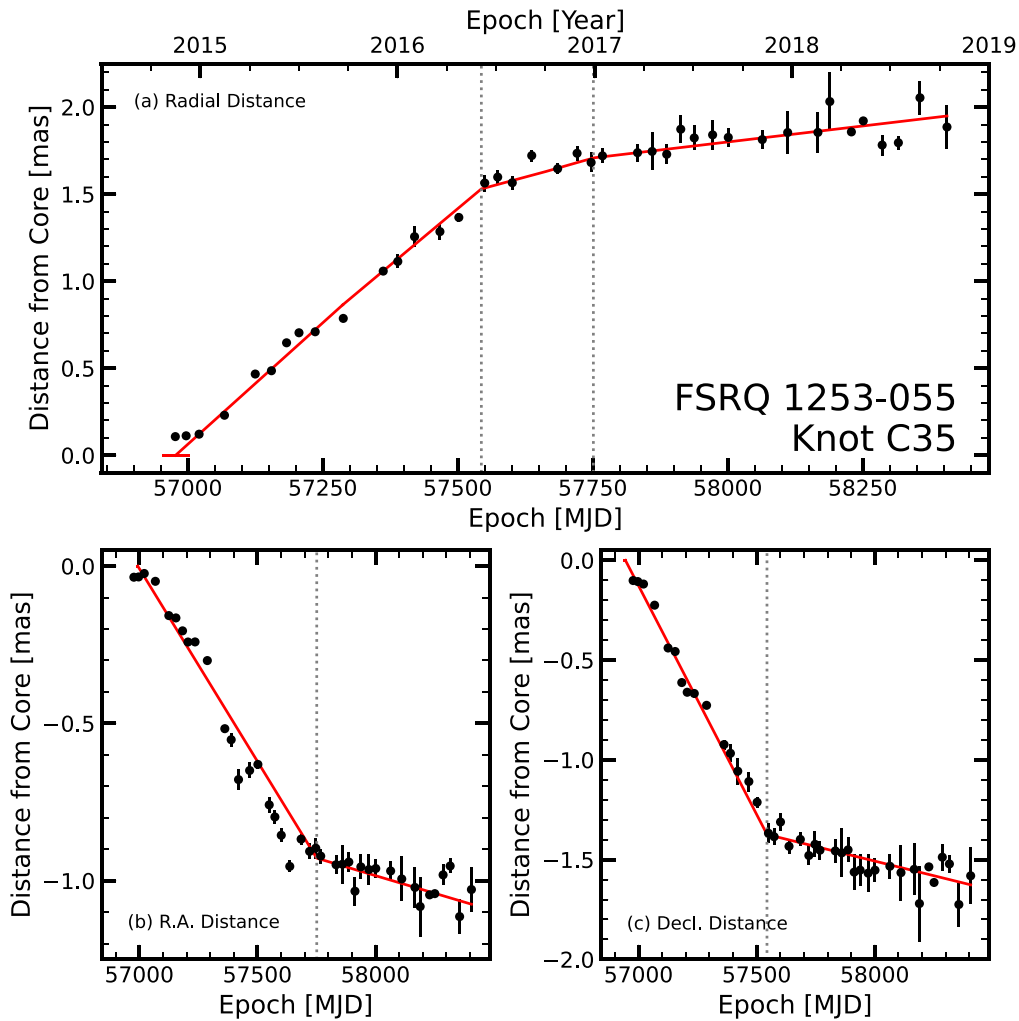[12] https://jekel.me/piecewise_linear_fit_py/index.html

Figure 1. An example of the piecewise linear fitting procedure described in Section 2.2 for the knot *C35* of the FSRQ 1253–055. The three panels represent the total distances from the core along the (a) radial *R*-axis, (b) *X*-axis (relative R.A.), and (c) *Y*-axis (relative decl.). The red lines represent the piecewise linear fits to the data, while the gray dotted lines indicate break-point dates. The fit line in (a) is constructed from the combination of the fits in (b) and (c). The estimated epoch of ejection, $t_\circ$, is shown in (a) as a horizontal red line. See the text for details.

addition to the new knots observed since 2012 December. As an example of this fitting procedure, Figure 1 shows the result for knot *C35* of the FSRQ 1253−055. Panels (b) and (c) presents the linear fits to the separation of the knot versus time along the *X* and *Y* dimensions, respectively. In this example, two segments are needed to represent both the *X* and *Y* motions accurately. Panel (a) shows the motion of the knot relative to the core along the radial *R* dimension, combining the *X* and *Y* models. For this example, there are three measurements of the speed of the knot and two estimates for the acceleration.

3. Parsec-scale Jet Structure

Given the above determination of the kinematic parameters of the jet components, we have separated the knots into different types according to their properties. Images of all sources at all epochs possess a core (described above), which we label as *A0*. All remaining components are classified based on their proper motion. Those with significant proper motion ($\mu \geqslant 2\sigma_\mu$) are designated as moving features of type *M*. Components without this proper motion are termed "quasi-stationary" (often shortened to "stationary" below) features of type *St*. We continue the naming scheme introduced in

Jorstad et al. (2017) for all previously analyzed sources. For the two sources added to the sample later (the BL Lac objects 1652 +398 and 1959+650), designations start at 1 for both moving and quasi-stationary features.

We have calculated the average parameters of all features in all of the blazars, and list the results in Table 3 in the following format: 1—B1950 name of the source; 2—ID of the knot; 3—the number of epochs, *N*, at which the knot is detected; 4—mean flux density, $\langle S \rangle$, of the knot and its standard deviation, in Jy; 5—average distance of the knot, $\langle R \rangle$, and its standard deviation, in milliarcseconds;[13] 6—average position angle of the knot with respect to the core, $\langle \Theta \rangle$, and its standard deviation, in degrees. For the core, $\langle \Theta \rangle$ is calculated using the weighted average of the Θ of all of the knots in the jet over all epochs at which $R \leqslant 0.7$ mas, and thus represents the average projected direction of the inner jet at a given epoch. Counter-jet features are not included in this calculation; 7—mean size of the knot, $\langle a \rangle$, and its standard deviation, in milliarcseconds; and 8—kinematic type of the knot (see above).

---

[13] This average represents the typical distance at which the knot was observed and is not necessarily the midpoint of its trajectory.

Table 3
Jet Structure

Source	Knot	N	$\langle S \rangle$ (Jy)	$\langle R \rangle$ (mas)	$\langle \Theta \rangle$ (deg)	$\langle a \rangle$ (mas)	Type
(1)	(2)	(3)	(4)	(5)	(6)	(7)	(8)
0219+428	A0	62	0.24 ± 0.09	0.00 ± 0.02	-166.0 ± 10.0	0.04 ± 0.02	Core
	A1	52	0.08 ± 0.04	0.17 ± 0.04	-167.9 ± 10.9	0.09 ± 0.03	St
	A2	36	0.04 ± 0.02	0.37 ± 0.06	-168.5 ± 9.5	0.14 ± 0.04	St
	A3	50	0.03 ± 0.01	0.65 ± 0.09	-173.2 ± 5.8	0.21 ± 0.09	St
	A4	56	0.03 ± 0.01	2.31 ± 0.09	-177.1 ± 1.4	0.46 ± 0.14	St
	B1	6	0.02 ± 0.01	1.03 ± 0.19	-175.7 ± 1.3	0.27 ± 0.06	M
	B2	10	0.02 ± 0.01	1.04 ± 0.22	-172.7 ± 6.0	0.40 ± 0.10	M
	B3	6	0.04 ± 0.03	0.48 ± 0.26	-160.7 ± 18.3	0.15 ± 0.11	M
	B4	7	0.01 ± 0.01	1.35 ± 0.45	-168.6 ± 1.3	0.41 ± 0.10	M
	B5	11	0.02 ± 0.02	0.94 ± 0.56	-169.5 ± 3.2	0.28 ± 0.14	M
	B6	4	0.01 ± 0.01	1.40 ± 0.24	-177.5 ± 3.2	0.43 ± 0.06	M
0235+164[a]	A0	126	1.30 ± 0.83	0.00 ± 0.02	-000.0	0.06 ± 0.03	Core
	B1	6	0.16 ± 0.23	0.40 ± 0.17	-17.7 ± 5.8	0.26 ± 0.13	M
	B2	15	1.03 ± 0.88	0.22 ± 0.08	163.1 ± 12.2	0.15 ± 0.06	M
	B3	40	0.25 ± 0.14	0.21 ± 0.07	164.9 ± 6.4	0.13 ± 0.05	M
	B4	16	0.15 ± 0.11	0.19 ± 0.06	-63.4 ± 21.0	0.13 ± 0.10	M
	B5	17	0.41 ± 0.29	0.28 ± 0.10	-059.1 ± 4.0	0.20 ± 0.07	M
	B6	19	0.19 ± 0.16	0.27 ± 0.11	-051.2 ± 6.2	0.23 ± 0.14	M
	B7	6	0.04 ± 0.01	0.26 ± 0.03	-009.6 ± 5.5	0.11 ± 0.05	M

Note.
[a] The direction of the inner jet for 0235+164 is uncertain, since features detected in the jet have a range of P.A. exceeding 180°.

(This table is available in its entirety in machine-readable form.)

Figure 2 presents an image of each source at a single epoch between 2013 January and 2018 December, when the most prominent features in the jet were visible. The black circles indicate the sizes and positions of the features according to the model parameters for that epoch. These images do not contain labels for all observed features in the jet over the 10 yr of observations. We list the important parameters for each image in Table 4 as follows: 1—B1950 name of the source; 2—epoch of observation; 3—total intensity peak of the map, I_{peak}, in mJy beam^{-1}; 4—lowest shown contour, I_{low}^{cnt}, in mJy beam^{-1}; 5—size of the restoring beam, used to produce images of similar fidelity across all epochs, in units of milliarcseconds × milliarcseconds, with all restoring beam orientation angles set to $-10°$; 6—antennas with no data for the source at that particular observation epoch; and 7—size and orientation angle of the synthesized beam corresponding to the *uv*-coverage for the epoch of observation, in units of milliarcseconds × milliarcseconds and degrees.

3.1. Observed Brightness Temperatures

The observed brightness temperatures of all jet features from 2007 June to 2012 December are listed in Table 2 of Jorstad et al. (2017), while those from 2013 January to 2018 December are listed in Table 2 of this paper. Combined, there are a total of 19,644 estimates for the brightness temperatures of components. Of these, 10.1% of the $T_{b,obs}$ values are lower limits (see Section 2.1).

For a direct comparison with the brightness temperatures analyzed in Jorstad et al. (2017), Figure 3 (left) displays the brightness temperatures of all cores in the host-galaxy frame ($T_{b,obs}^s = T_{b,obs}(1 + z)$) from 2013 January to 2018 December for each subclass of blazar. The RG distribution peaks at $(1–5) \times 10^{11}$ K. Only a few cores have epochs when $T_{b,obs}^s \geqslant 5 \times 10^{11}$ K. The FSRQ distribution is bimodal, with peaks at both $(1–5) \times 10^{11}$ K and $(1–5) \times 10^{12}$ K. The highest

peak of the BL Lac object distribution is also at $(1–5) \times 10^{12}$ K, but includes a large number of lower limits. The BL Lac object distribution also has the most significant number of cores with low brightness temperatures ($T_{b,obs}^s < 10^{11}$ K). The distributions of the brightness temperatures for knots, other than the cores, between 2013 January and 2018 December are shown in Figure 3 (right). In general, these knots have lower brightness temperatures than the cores, but with much wider dispersion about the mean. Both distributions are similar in shape to those presented in Jorstad et al. (2017), indicating no apparent time variability in the populations of brightness temperatures of components as a whole for the sources in our sample.

A direct comparison of the distributions for each subclass presented in Figure 3 (as with a Kolmogorov–Smirnov, K-S, test) would ignore two crucial aspects of the data: (1) that the brightness temperature values for the cores and the knots of a particular object in our sample are correlated by virtue of coming from the same source, rather than being an independent measurement from a random blazar, and (2) the relatively large number (in some cases, ~50%, e.g., the core of the BL Lac object 1959+650) of lower limits present in the sample. In order to compare the brightness temperatures of the cores and knots in our sample between each subclass, we derive "typical" values for the brightness temperatures of components for each source by estimating the survival function of the brightness temperature of the cores and knots to get the median value (see the Appendix).

Figure 4 (left) shows the median brightness temperatures of core components of blazars in our sample between 2013 January and 2018 December, while Figure 4 (right) shows the same for the entire observing period of the program (2007 June–2018 December). The three RGs in the sample have very similar median core brightness temperatures, ~5×10^{11} K. The distribution of the median $T_{b,obs}^s$ for BL Lac objects is very wide spread, ranging from 10^{10} K to ~10^{13} K. The cores of FSRQs
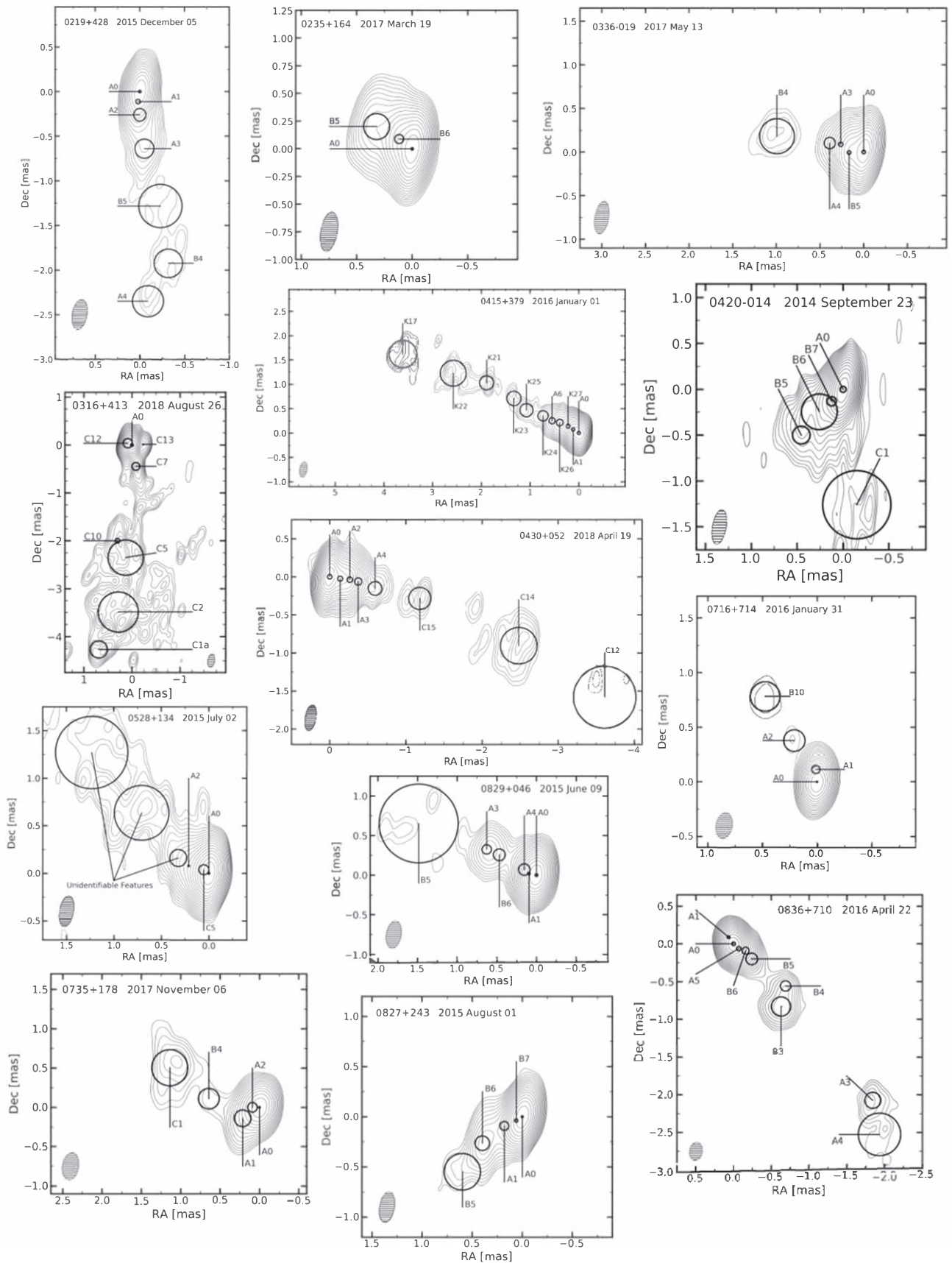
Figure 2. Total intensity images of the VLBA-BU-BLAZAR sample at 43 GHz with uniform weighting. Parameters of all images are listed in Table 4. Contours decrease by a factor of $\sqrt{2}$ from the peak flux density. Black circles on the images indicate the jet features according to the model fits. The shaded ellipse in the bottom-left corner represents the restoring beam.
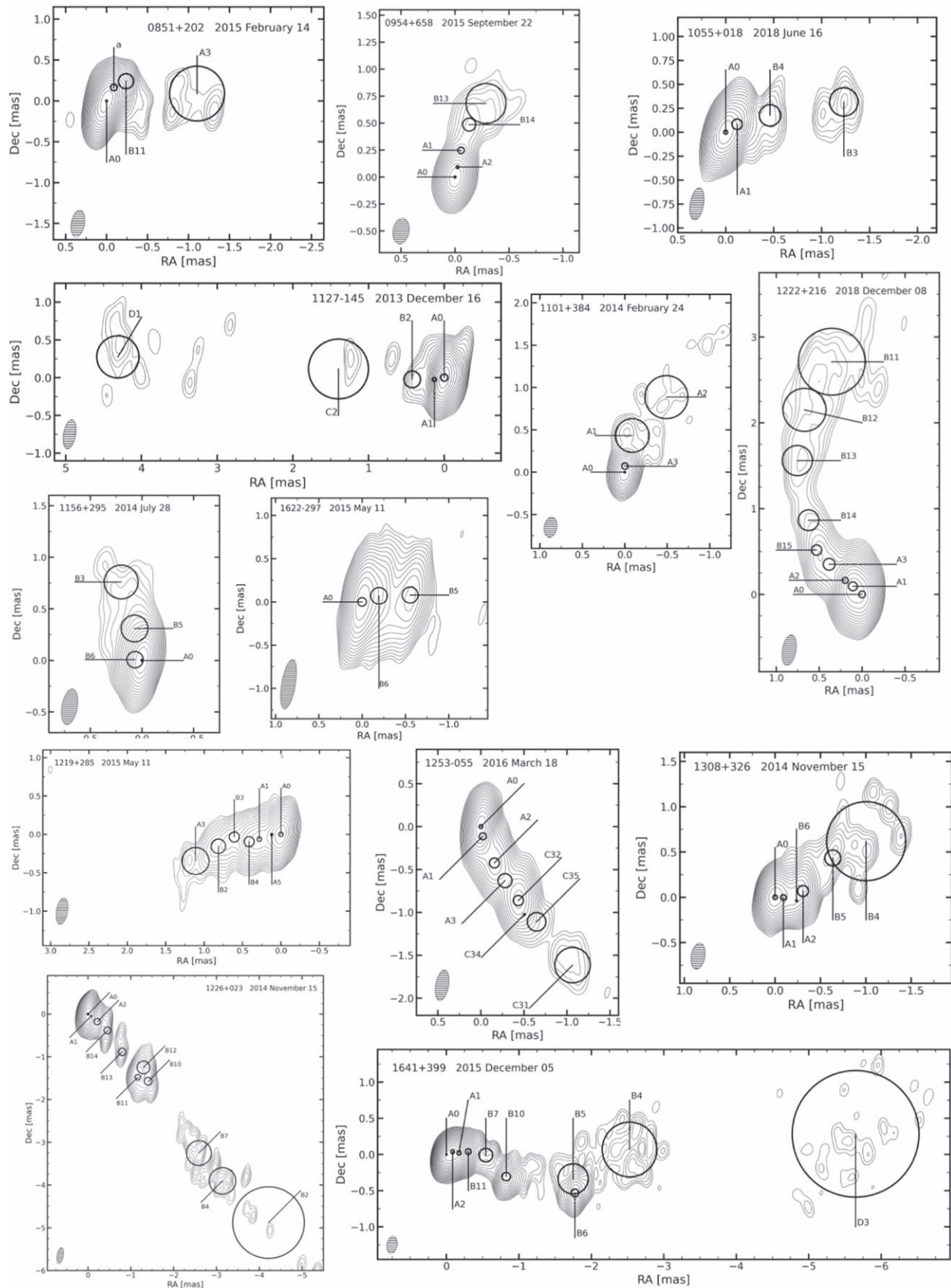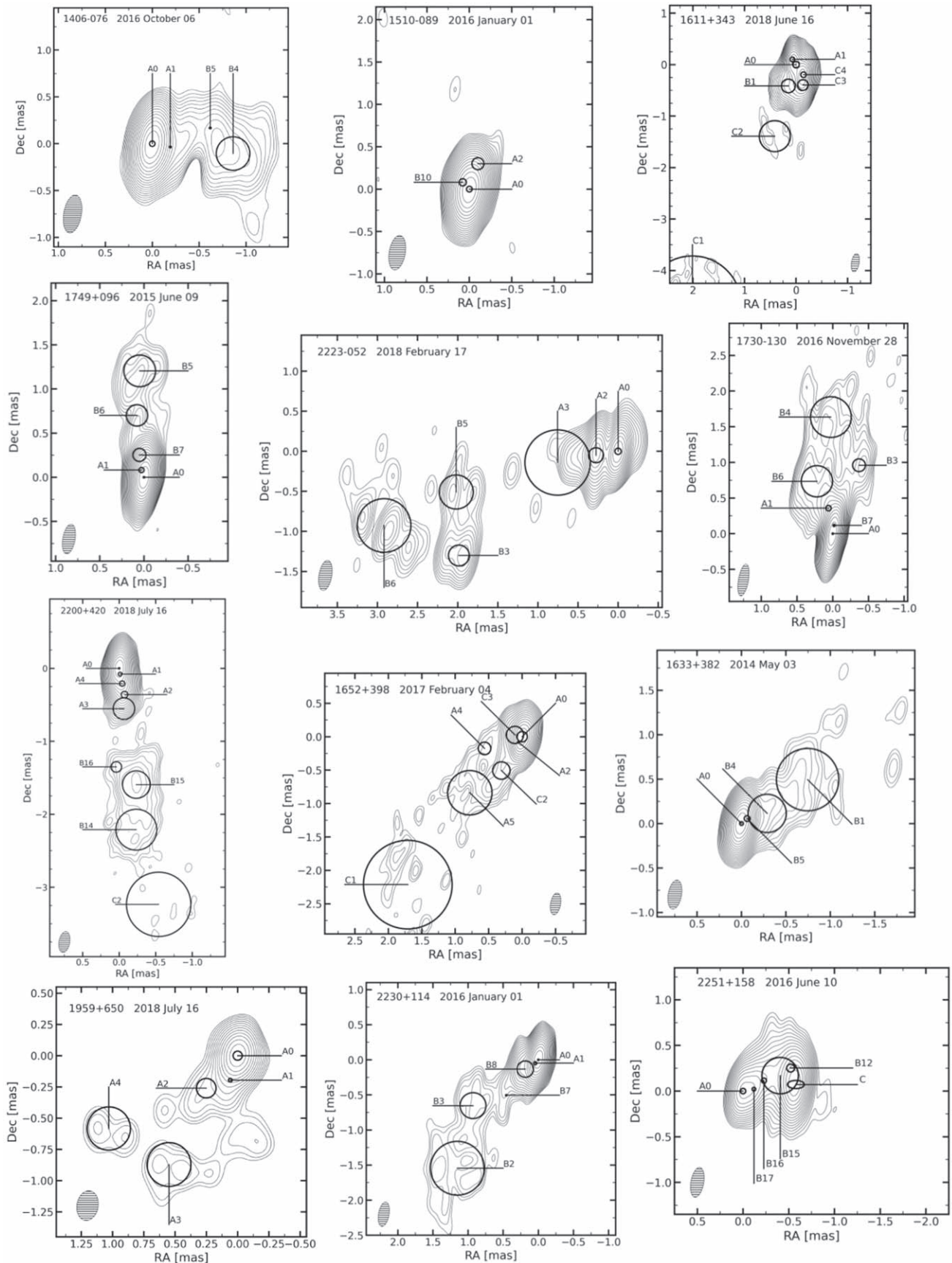
Figure 2. (Continued.)

Figure 2. (Continued.)

Table 4
Parameters of VLBA 43 GHz Images in Figure 2

Source	Epoch	$I_{\rm peak}$	$I_{\rm low}^{\rm cnt}$	Beam Size	Unavailable Antennas[a]	Synthesized Beam Size
		(mJy beam^{-1})	(mJy beam^{-1})	(mas × mas)		(mas × mas, deg)
(1)	(2)	(3)	(4)	(5)	(6)	(7)
0219+428	2015 Dec 5	233	1.82	0.17 × 0.34	...	0.16 × 0.28, − 4.1
0235+164	2017 Mar 19	866	3.38	0.15 × 0.36	...	0.16 × 0.33, − 3.4
0316+413	2018 Aug 26	1572	12.28	0.15 × 0.28	...	0.16 × 0.30, 10.0
0336−019	2017 May 13	1214	6.71	0.16 × 0.38	...	0.16 × 0.37, − 2.8
0415+379	2016 Jan 1	578	2.26	0.16 × 0.32	...	0.16 × 0.33, − 2.5
0420−014	2014 Sep 23	1207	4.71	0.15 × 0.38	HN	0.16 × 0.39, − 2.9
0430+052	2018 Apr 19	1117	2.18	0.14 × 0.34	...	0.15 × 0.36, − 4.4
0528+134	2015 Jul 2	366	0.72	0.15 × 0.33	...	0.16 × 0.37, − 0.9
0716+714	2016 Jan 31	1498	8.28	0.15 × 0.24	...	0.16 × 0.28, − 7.1
0735+178	2017 Nov 6	204	2.25	0.21 × 0.35	BR, SC	0.16 × 0.73, − 20.0
0827+243	2015 Aug 1	322	1.26	0.15 × 0.31	...	0.16 × 0.31, − 3.1
0829+046	2015 Jun 9	723	2.83	0.19 × 0.35	...	0.17 × 0.39, − 7.8
0836+710	2016 Apr 22	854	3.33	0.17 × 0.24	...	0.16 × 0.24, − 16.0
0851+202	2015 Feb 14	4807	9.39	0.16 × 0.33	FD	0.20 × 0.57, 26.0
0954+658	2015 Sep 22	723	3.99	0.15 × 0.24	...	0.17 × 0.24, 8.5
1055+018	2018 Jun 16	2195	8.57	0.14 × 0.34	SC	0.15 × 0.68, − 18.0
1101+384	2014 Feb 24	281	3.10	0.15 × 0.24	FD	0.16 × 0.28, − 21.0
1127−145	2013 Dec 16	1112	4.34	0.16 × 0.39	KP	0.17 × 0.46, − 8.2
1156+295	2014 Jul 28	1087	4.25	0.15 × 0.35	...	0.16 × 0.31, 0.5
1219+285	2015 May 11	205	0.80	0.15 × 0.35	...	0.17 × 0.30, − 8.3
1222+216	2018 Dec 8	473	1.85	0.16 × 0.36	...	0.16 × 0.33, − 10.0
1226+023	2014 Nov 15	3612	7.05	0.15 × 0.38	...	0.18 × 0.44, − 5.6
1253−055	2016 Mar 18	6266	24.47	0.15 × 0.36	...	0.17 × 0.40, − 4.6
1308+326	2014 Nov 15	571	2.23	0.15 × 0.29	...	0.17 × 0.35, − 15.0
1406−076	2016 Oct 6	654	1.28	0.19 × 0.41	HN, MK	0.20 × 0.82, 23.0
1510−089	2016 Jan 1	4277	5.91	0.19 × 0.41	...	0.14 × 0.45, − 10.0
1611+343	2018 Jun 16	616	1.70	0.15 × 0.36	SC	0.16 × 0.37, − 27.0
1622−297	2015 May 11	589	3.25	0.16 × 0.58	HN	0.13 × 0.40, − 4.8
1633+382	2014 May 3	2230	4.36	0.15 × 0.33	NL	0.15 × 0.30, − 9.2
1641+399	2015 Dec 5	1800	1.76	0.14 × 0.24	...	0.15 × 0.28, − 17.0
1652+398	2017 Feb 4	175	0.97	0.15 × 0.33	BR	0.15 × 0.31, − 20.0
1730−130	2016 Nov 28	1812	3.54	0.14 × 0.45	...	0.14 × 0.38, − 4.5
1749+096	2015 Jun 9	3310	3.23	0.14 × 0.34	...	0.15 × 0.36, − 7.0
1959+650	2018 Jul 16	126	1.39	0.17 × 0.24	HN, PT, SC	0.20 × 0.34, − 7.0
2200+420	2018 Jul 16	1745	1.70	0.15 × 0.29	...	0.16 × 0.25, − 8.1
2223−052	2018 Feb 17	486	1.90	0.16 × 0.38	MK, SC	0.27 × 0.81, − 5.0
2230+114	2016 Jan 1	1840	3.59	0.15 × 0.35	...	0.14 × 0.40, − 7.9
2251+158	2016 Jun 10	5115	28.26	0.14 × 0.33	...	0.13 × 0.33, − 6.1

Note.
[a] Antenna abbreviations can be found at the NRAO VLBA website (https://science.nrao.edu/facilities/vlba/docs/manuals/oss/sites). Individual antennas are sometimes unavailable due to weather, maintenance, or undetected fringes (in the case of the weakest sources, e.g., 1959+650).

are more narrowly distributed around a central brightness temperature, $\sim 10^{12}$ K. As the process of calculating the median brightness temperature has already taken into account the presence of lower limits, we can now meaningfully compare the distributions for each subclass through a K-S test. Values of the test statistic, $\mathcal{D}$, and significance, p, values for the test between each subclass distribution are given in Table 5. The differences between the FSRQ and RG core distributions are statistically significant at a $\sim 3\sigma$ level, with $p = 0.009$, once all cores from 2007 June to 2018 December have been taken into account. The FSRQ and BL Lac object cores also appear to be different, but at a less significant level ($p = 0.086$). There is no statistical difference between the BL Lac object and RG distributions, but it is important to note that the number of sources is small (13 for BL Lac objects and three for RGs).

Similarly to the core distributions, in Figure 5 we show the median knot brightness temperature distributions for each subclass, including knots observed from 2013 January to 2018 December (left) and 2007 June to 2018 December (right). In general, the median knot brightness temperature distribution for each subclass is centered on lower values than that of the core components. The knots of FSRQs are more concentrated around the mean value than the knots of BL Lac objects. The knots of the RG 0316+428 have a higher median $T_{\rm b,obs}^{\rm s}$ than the other two RG in the sample. The $\mathcal{D}$- and p-values for a K-S test between the knot distributions are given in Table 6. The only distributions that show a statistically significant difference are the knots of FSRQs compared with BL Lac objects, at a significance $p = 0.002$ for the entire observed time period.

Despite the low significance levels according to a K-S test (likely due to the number of sources in our sample), we see a
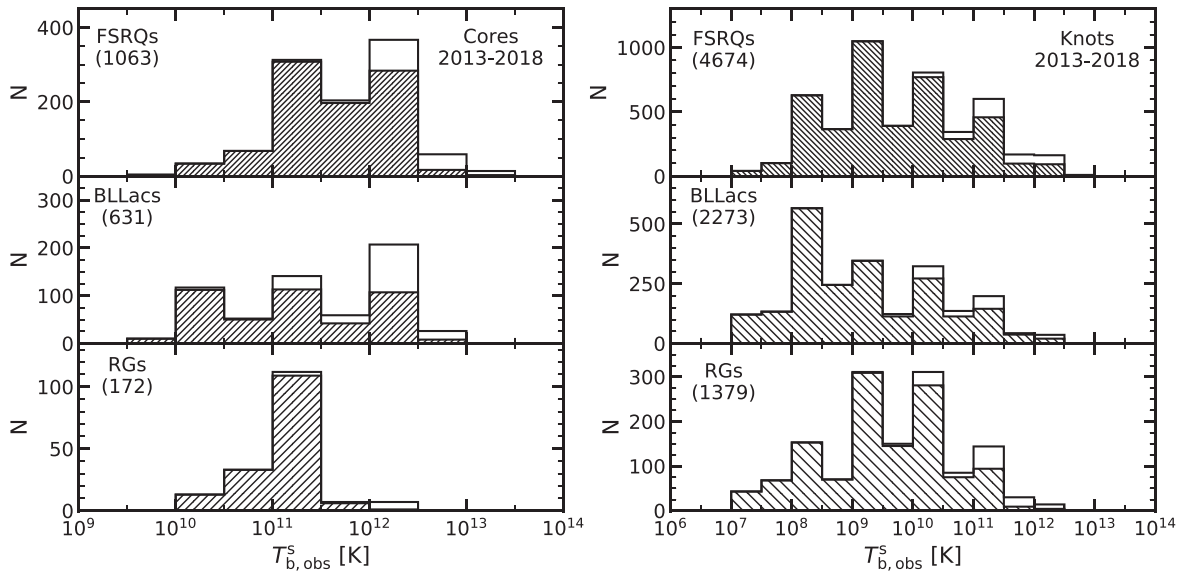
Figure 3. Host-galaxy frame brightness temperature distributions of the core (left) and noncore (knots, right) features between 2013 January and 2018 December. Unshaded regions of the distributions represent components with lower limits to $T^s_{b,obs}$. The bin sizes are neither linear nor logarithmic. Values in parentheses are the number of $T_{b,obs}$ measurements of components for each subclass, including lower limits.

general trend across the median core and knot brightness temperature distributions: *FSRQs and BL Lac objects have more intense cores than those of RGs, but the knots in the extended jets of BL Lac objects are significantly less intense than the knots of RGs and FSRQs.* A small fraction of analyzed knots are weak diffuse features with $T^s_{b,obs} < 10^8$ K. The highest brightness temperatures, near 10^{13} K, are discussed in Section 6.1.

3.2. Jet Position Angles

With over 10 yr of observations, we can constrain the bulk characteristics of the jet, such as the average position angle, $\langle \Theta_{jet} \rangle$, and its temporal evolution. Such constraints are important for determining whether there are sudden changes in the direction of the jet, or if precession is common in blazars. In addition, since the calculation of acceleration along or perpendicular to the jet axis depends on the position angle, such information can allow us to account for the effect of changes in Θ_{jet} on the accelerations.

In order to determine how the jet position angles vary, we have constructed plots of the observed position angle, Θ, versus time for all knots in each source. Figure 6 shows an example of such plots for the source 0219+428. The figure set for Figure 6 provides a similar plot for each source in the sample.

We have visually inspected the plots in Figure 6 to see if there are any overall trends or abrupt changes in the position angles of knots. This leads us to classify the average jet position angle behavior into three categories: (1) $\langle \Theta_{jet}(t) \rangle = $ constant (i.e., variations are insignificant), labeled as C; (2) a linear dependence, $\langle \Theta_{jet}(t) \rangle = a_1 * (t - t_{ave}) + a_0$, where t_{ave} is the midpoint of the observed period, labeled with L; and (3) a cubic spline fit, $\langle \Theta_{jet}(t) \rangle = $ spline$(t - t_{ave})$, labeled as S.

In order to perform a more quantitative placement of the sources into these categories, we have calculated the average inner jet direction, $\langle \Theta_{jet} \rangle$, and standard deviation, $\sigma_{\langle \Theta_{jet} \rangle}$, by averaging Θ of all moving knots within a distance from the core of $\sim 3\times$ the observing beam FWHM (i.e., the inner jet). For several jets, there are one or two knots with Θ significantly different from the others, which we exclude from this

calculation. We have compared $\sigma_{\langle \Theta_{jet} \rangle}$ with the average uncertainty of the knot position angle measurement within the inner jet, $\langle \sigma_\Theta \rangle$. If $\sigma_{\langle \Theta_{jet} \rangle} \leqslant 3 \times \langle \sigma_\Theta \rangle$, the position angle is classified as constant, C. For sources where this criterion is not met, we have employed either linear or spline fits as determined from visual inspection of the behavior of Θ for all knots. To confirm that these fits provide a better estimate of the jet position angle, we have compared the standard deviation of the fit to the standard deviation of a constant $\langle \Theta_{jet} \rangle$. In the majority of cases, the fit reduced the standard deviation of the knot position angles to within the $3 \times \langle \sigma_\Theta \rangle$ criterion. This criterion remained unmet after the fit in only four sources (0716+714, 1226+023, 1253–055, and 1749+096), but even in these cases, the fits improved the standard deviation, and so were adopted. Finally, a handful of sources have a very wide dispersion, but no clear trend in the position angles of knots. For these sources, we have created a fourth category (W for "wide"), where we have adopted a constant value of $\langle \Theta_{jet} \rangle$, but with a standard deviation $> 3 \times \langle \sigma_\Theta \rangle$.

Table 7 describes the fits for each source as follows: 1—source name; 2—constant average position angle of the knots in a jet, $\langle \Theta_{jet} \rangle$ (in degrees), regardless of the best fit; 3—average error of knot position angles, $\langle \sigma_\Theta \rangle$ (in degrees); 4—categorization of the jet position angle behavior, with categories as described above;[14] 5—midpoint in time of all of the knot observations, t_{ave}, for the fits; 6—standard deviation of the best fit to knot position angles, $\sigma_{\langle \Theta_{jet} \rangle}$, in degrees; and 7—knots that were used to determine the average position angles and fits.

The majority of sources in our sample (23/38, 60.5%) have knots in the jet with position angles that are relatively constant over time, i.e., have a narrow spread. For these, we take the value in Column 2 of Table 7 to be $\langle \Theta_{jet} \rangle$ in the analyses that follow. Six other sources (15.8% of the sample) are well described by a constant jet direction, but have very wide jets in terms of the spread of the position angles of knots. Despite the latter property, we adopt the value listed in Column 2 for the

---

[14] Due to their complexity, spline fits are available upon request. Linear fits are provided below.
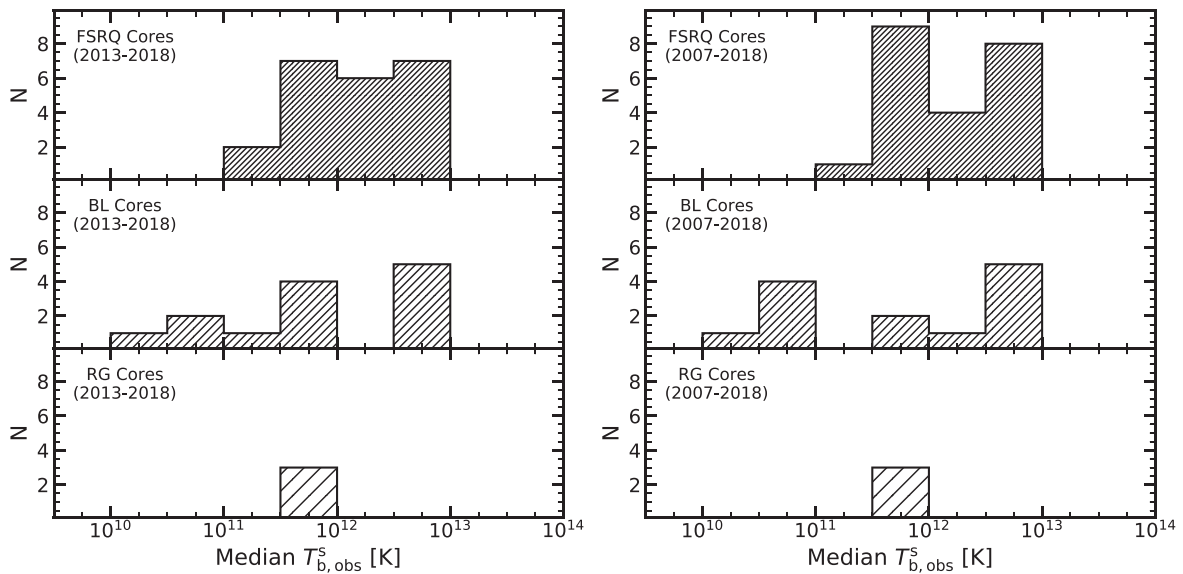
Figure 4. Median core component host-galaxy frame brightness temperature distributions of blazars in the VLBA-BU-BLAZAR sample, as determined through survival analysis. The bin sizes are neither linear nor logarithmic.

Table 5
K-S Test Statistic, $\mathcal{D}$-, and p-values for the Median Brightness Temperatures of Jet Cores

Subclass 1	Subclass 2	$\mathcal{D}$	p
FSRQ	BL	0.388	0.129
FSRQ	RG	0.818	0.030
BL	RG	0.615	0.229
FSRQ	BL	0.416	0.086
FSRQ	RG	0.909	0.009
BL	RG	0.538	0.375

Note. The data for Section 1 of this table consist of observations taken from 2013 January through 2018 December. The data for Section 2 were taken from 2007 June through 2018 December.

subsequent analyses. Only two sources (the FSRQs 0420−014 and 1226+023) have clear linear trends of knot position angle variations over time. The linear fit for 0420−014 is $\langle\Theta_{\mathrm{jet}}(t)\rangle = (5.9 \pm 0.2) * (t - 2013.24) + (127.0 \pm 0.7)$ degrees, while the fit for 1226+023 is $\langle\Theta_{\mathrm{jet}}(t)\rangle = (1.2 \pm 0.1) * (t - 2013.79) - (140.9 \pm 0.2)$ degrees. The remaining seven sources (18.4%) display very complex behavior. Some (e.g., the FSRQ 1222+216) visually resemble jet rotation (possibly precession), while others exhibit abrupt changes in the jet position angle (e.g., the FSRQ 1253−055). For the sources best fit with a linear trend or spline, we use the fits to calculate the jet position angle at the time of acceleration for the analysis in Section 4.3. We use the average of the fit over the observed time period for each knot for the analysis of stationary features in Section 4.2. For all sources, we use $\sigma_{\langle\Theta_{\mathrm{jet}}\rangle}$ as the uncertainty on $\langle\Theta_{\mathrm{jet}}\rangle$ in the subsequent analyses.

4. Motions of Knots in the Jets

Between 2007 and 2018 we have identified 559 distinct emission features in the parsec-scale jets of the 38 blazars in the VLBA-BU-BLAZAR sample. Of this total number, 38 are the 43 GHz cores. Among the remaining knots, 96 have been classified as quasi-stationary (18.4% of noncore components),

leaving 425 classified as moving knots. Accelerations along the jet cause 75 of the moving knots (17.6%) to have multiple estimates for their apparent speed as they traverse different regions along their trajectory. The only sources that do not exhibit apparent superluminal motion in the parsec-scale jet are the BL Lac objects 1652+398 and 1959+650. Interestingly, we find superluminal motion in the generally subluminal jet of the RG 0316+413 (3C 84) in one knot, $C10$, with an apparent speed of $\beta_{\mathrm{app}} = 1.38c \pm 0.03c$. We consider this estimate of the knot speed to be reliable, with multiple observations of its motion close to the core and a well-defined epoch of ejection. Also, we detect knot motions up to $\sim 2c$ in the BL Lac object 1101+384 (Mkn 421).

For each source, we have constructed a plot displaying the separation of all knots from the core (Figure 7). Each knot is color-coded in the corresponding figure in Figure 6 according to its motion type. In each figure, the black vectors show the P.A. of knots with respect to the core at the corresponding epoch. The solid lines represent the piecewise linear fits to the knot motions, the red dotted line shows the position of the core, and dashed colored lines mark the average positions of the stationary components. Error bars on each measurement are the approximate 1σ positional uncertainties based on $T_{\mathrm{b,obs}}$. Lines extrapolating the knot motion back to the epoch of ejection $t_\circ$ may appear slightly bent in some cases owing to (1) R being a quadratic combination of X and Y, or (2) instances where $|t_{x\circ} - t_{y\circ}| \geqslant 0.5$ yr so that the epoch of ejection is calculated using a linear fit to the first segment of R data. These apparent bends have no effect on the apparent speeds. Figure 7 presents an example of these plots for the BL Lac object 0219+428 (3C 66A).

4.1. Moving Feature Properties

Here we describe the properties of the moving features in the jets of sources in each of the three subclasses of blazars. Because knot C of the FSRQ 2251+158 (3C 454.3) shows motion despite being a quasi-stationary feature (see Section 4.2), we include it in the analysis of 426 moving knots. Since any individual knot can have multiple motions
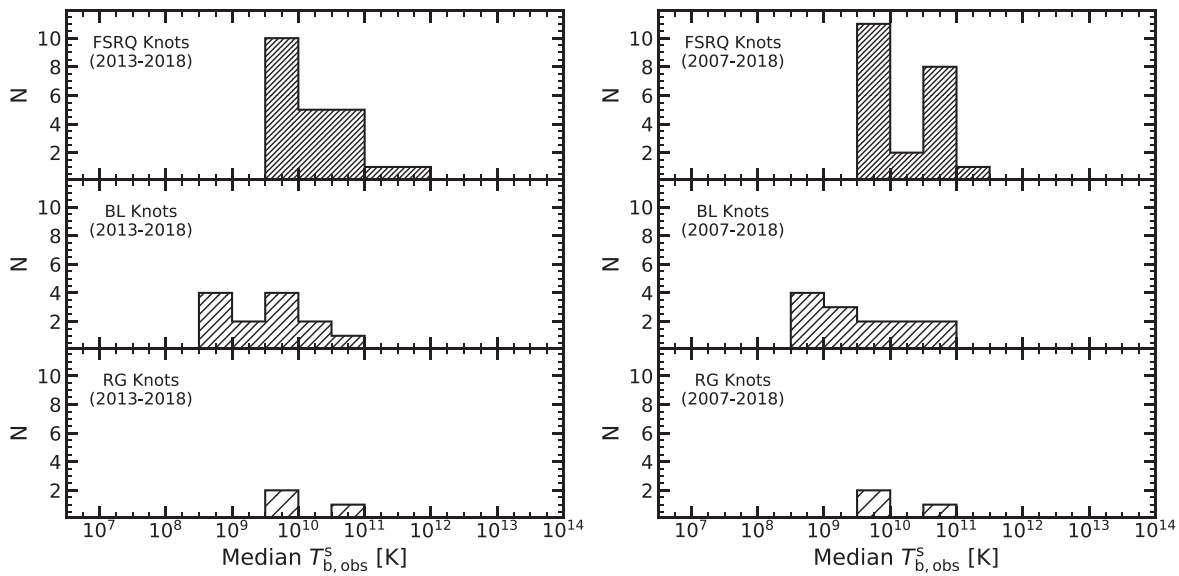
Figure 5. Median knot component host-galaxy frame brightness temperature distributions of blazars in the VLBA-BU-BLAZAR sample, as determined through survival analysis. The bin sizes are neither linear nor logarithmic.

Table 6
K-S Test Statistic, $\mathcal{D}$-, and p-values for the Median Brightness Temperatures of Jet Knots

Subclass 1	Subclass 2	$\mathcal{D}$	p
FSRQ	BL	0.538	0.010
FSRQ	RG	0.363	0.750
BL	RG	0.615	0.229
FSRQ	BL	0.615	0.002
FSRQ	RG	0.439	0.574
BL	RG	0.615	0.229

Note. The data for Section 1 of this table consist of observations taken from 2013 January through 2018 December. The data for Section 2 were taken from 2007 June through 2018 December.

over different time periods, we analyze a total of 529 knot speeds.

Table 8 presents the speeds of the moving knots as follows: 1—name of the source; 2—designation of the component; 3—segment number of the fit to the knot motion, N_{seg} (1 for purely linear motion in both the X and Y direction, up to 5[15]); 4—start date of the segment, t_{s}, in years; 5—end date of the segment, t_{e}, in years; 6—proper motion, μ, and its associated 1σ uncertainty, in milliarcseconds per year; 7—direction of motion, Φ, and its associated 1σ uncertainty, in degrees; 8—apparent speed, β_{app}, and its associated 1σ uncertainty, in units of c; 9—epoch of ejection, $t_{\circ}$, and its associated 1σ uncertainty (only available for the first segment of a knot) in years; and 10—flag indicating whether $t_{\circ}$ was calculated to the combined X and Y dimension fit (XY), or if a fit to the R coordinate of the first segment was necessary (R, see Section 2.2). If the segment was not the first segment for a particular knot, the flag is NA.

Figure 8 (left) shows the distributions of the apparent speeds of the features for FSRQs, BL Lac objects, and RGs separately for the entire observing period from 2007 June to 2018

December for ease of comparison with previous literature. An increase in the number of moving knots by a factor of ~3 has dramatically filled in the FSRQ and BL Lac object distributions over those presented in Jorstad et al. (2017). The main distribution of apparent speeds of features in the jets of FSRQs covers a wide range of β_{app}, from $0.5c$ to $\sim50c$. Two knots (*B1* of 0528+134 and *D2* of 2230+114) have segments where the speed of the knot exceeds $50c$. In order to limit the size of the figure, these have been included in the last bin. They represent a small percentage (0.6%) of the total number of knots and thus do not affect the conclusions. The FSRQ distribution peaks in the $8c$–$10c$ bin but has a very long tail, extending continuously with at least one knot in each bin up to the $38c$–$40c$ range. The apparent speeds in the jets of BL Lac objects exhibit a very different distribution, with a peak in the $0c$–$2c$ bin and a similarly sized peak in the $8c$–$10c$ bin. The distribution does not extend to β_{app} as high as for FSRQs, with the maximum BL Lac object speed of $\sim27c$ occurring for a segment of the knot *B3* of 1749+096. The distribution of apparent speeds of RG knots is limited to much lower values than those of the other two subclasses. The peak between $4c$ and $6c$ corresponds to 0415+379 and 0430+052, with the peak from $0c$ to $2c$ coming primarily from 0316+413 (3C 84).

In order to more appropriately determine the differences in the distributions of apparent speed for FSRQs, BL Lac objects, and RGs, we calculate a single average apparent speed, $\langle\beta_{\mathrm{app}}\rangle$, for each source as the weighted average of the apparent speeds of all knots in that source. The distributions of these average apparent speeds are shown in Figure 8 (right). We see that the FSRQs have a well-determined peak in the distribution with $\langle\beta_{\mathrm{app}}\rangle \sim 12$–$14c$. The BL Lac objects have a very wide dispersion of average apparent speeds. With just three sources, it is easy to see (with Table 8) that the knots of 0316+413 are, on average, subluminal, while those of 0415+379 and 0430+052 are superluminal. Despite the small numbers of sources (especially for RGs), we have performed a K-S test between the distributions. The BL Lac object and RG distributions are the most similar, with $\mathcal{D} = 0.500$ and $p = 0.525$, likely due to the small number of sources. However, moderately significant differences are seen between the FSRQ:BL ($\mathcal{D} = 0.492$, $p = 0.029$) and FSRQ:RG

---

[15] If the best fit in a given dimension is with a three-segment broken linear fit, then there are two break points in that direction of motion. If both the X and Y motions are fit with a three-segment broken linear fit, there are four total break points and five line segments.
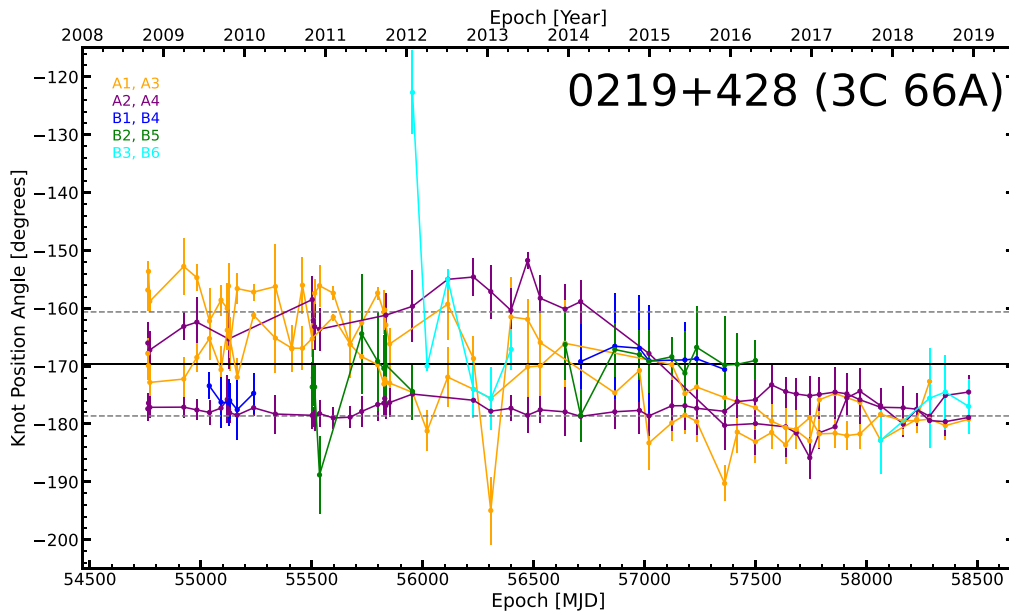
Figure 6. Jet position angles of each knot, relative to the core, of the BL Lac object 0219+428 (3C 66A). The colors of each knot are the same as in Figure 7, and are designated in the upper-left corner. We classify this source as having a constant jet position angle according to our criterion (see the text and Table 7). The black line indicates $\langle\Theta_{\rm jet}\rangle$, and the two gray dashed lines show the standard deviation of the P.A. with respect to $\Theta_{\rm jet}$, $\sigma_{\langle\Theta_{\rm jet}\rangle}$, which is listed in Column 7 of Table 7. Similar plots for all sources in the sample are available in the figure set.

(The complete figure set (38 images) is available.)

($\mathcal{D} = 0.955$, $p = 0.003$) distributions. Taking all of the results of Figure 8 into consideration, we see that the knots of FSRQs have, on average, higher apparent speeds than those of BL Lac objects, with RGs having the lowest apparent speeds.

We analyze the direction of the velocity vector of each knot by following the same approach as in Jorstad et al. (2017), calculating the difference between the direction Φ of the apparent velocity (given in Table 8) and the average position angle of the jet, $\langle\Theta_{\rm jet}\rangle$ (listed in Table 3). Instead of determining an average value of this parameter for each source, we consider the difference between Φ and $\langle\Theta_{\rm jet}\rangle$ for a given knot to be an independent measure of the possible dispersion of the position angles for each subclass of blazar, as all knots are required to determine the width/dispersion of a jet. Figure 9 plots the distributions of $|\Phi - \langle\Theta_{\rm jet}\rangle|$ for FSRQs, BL Lac objects, and RGs. The peak of each distribution lies within the first bin ($<10°$) and represents 34.1%, 40.3%, and 74.7% of the total number of knots in FSRQs, BL Lac objects, and RGs, respectively.

In order to measure the deviation from unidirectional motion, we first calculate the average uncertainty in the motion direction as $\langle\sigma(\Phi)\rangle = \sum_{i=1}^{N_k} \sigma(\Phi_i)/N_k$, where N_k is the total number of knot speeds measured in each subclass. BL Lac objects have the largest dispersion of knot motions, with $\langle\sigma(\Phi)\rangle = 7°.2$, while FSRQs and RGs have a dispersion $\langle\sigma(\Phi)\rangle = 4°.2$ and $4°.8$, respectively. The much larger dispersion in this work compared to those presented in Jorstad et al. (2017) is likely caused by a significantly larger number of measured speeds based on the revised method for calculating motion. In order to determine whether this dispersion is from varying directions of the velocity vectors of knots or from knots smaller than the jet cross section being displaced from the jet axis by various distances, we calculate the average position angle dispersion of knots in a subclass as $\langle\sigma(\langle\Theta\rangle)\rangle = \sum_{i=1}^{N_k} \sigma(\langle\Theta\rangle_i)/N_k$. Based on this,

FSRQs have the widest range of average knot position angles, with $\langle\sigma(\langle\Theta\rangle)\rangle = 9°.9$, while BL Lac objects and RGs have smaller dispersions of $8°.8$ and $5°.7$, respectively. We conclude that, while the knots of FSRQs are more inclined to move along the same direction in the jet than are the knots in the jets of BL Lac objects, FSRQs have wider projected opening angles. The latter can be connected with a smaller viewing angle and/or a wider intrinsic opening angle for FSRQs. FSRQs and BL Lac objects possess a similar percentage of knots in which the velocity vector deviates from the jet axis by a value between 30° and 60°, 12.5% and 14.4%, respectively. In contrast, only 2.5% of the knots of RGs have motions that fall within this deviation range.

Among superluminal knots there are 5, 13, and 19 segments in FSRQs, BL Lac objects, and RGs, respectively, with very slow ($<1c$) or even upstream motion corresponding to $|\Phi - \langle\Theta_{\rm jet}\rangle| > 90°$. These are shown in the last bin of the distribution, since they represent a small fraction of the total number of knot segments. A K-S test indicates that the FSRQ and BL Lac object distributions are *not* significantly different ($\mathcal{D} = 0.138$, $p = 0.046$). However, the FSRQ and BL Lac object distributions *are* statistically different from the RG distribution ($\mathcal{D} = 0.439$, $p = 1.8 \times 10^{-11}$ for FSRQs versus RGs, and $\mathcal{D} = 0.369$, $p = 1.2 \times 10^{-6}$ for BL Lac objects versus RGs).

4.2. Quasi-stationary Features

We have identified 96 features with no statistically significant motion (as defined in Jorstad et al. 2017). Of these, 45 are in FSRQs, 38 in BL Lac objects, and 13 in RGs. All sources in our sample except 0235+164 (BL), 0316+413 (RG), 1156+295, and 1622−297 (FSRQs) continue to contain at least one—but usually multiple—stationary feature in addition to the core. On average, FSRQs possess ~2 and BL

Table 7
Jet Position Angles

Source	$\langle\Theta_{\mathrm{jet}}\rangle$ (deg)	$\langle\sigma_\Theta\rangle$ (deg)	Type[a]	t_{ave} (yr)	$\sigma_{\langle\Theta_{\mathrm{jet}}\rangle}$ (deg)	Knots Included
(1)	(2)	(3)	(4)	(5)	(6)	(7)
0219+428	−169.6	5.5	C	…	9.0	B1—B6
0235+164	54.7	6.8	C	…	6.6	B5, B6
0316+413	173.3	0.4	W	…	9.6	All except C4, C8, C12, C13
0336−019	78.7	4.6	C	…	6.4	B1—B5
0415+379	66.1	2.2	C	…	4.9	K1—K31
0420−014	121.0	3.7	L	2013.24	8.3	B1—B9
0430+052	−113.5	2.9	C	…	3.2	C1—C15
0528+134	64.8	6.0	C	…	13.3	B1—B3; C1—C5
0716+714	24.3	3.9	S	2012.98	18.4	A1, A2; B1—B14; T10
0735+178	78.5	10.7	C	…	13.8	B1—B4; C1
0827+243	127.1	5.8	C	…	8.1	B1—B9
0829+046	63.1	5.7	C	…	10.6	A1—A4; B1—B6
0836+710	−140.0	3.3	C	…	9.0	B1—B6
0851+202	−24.1	1.2	S	2012.44	2.7	a
0954+658	−13.7	2.1	S	2013.97	5.5	A1, A2
1055+018	−63.8	6.5	C	…	18.4	B1; B4; T1
1101+384	−14.4	14.2	C	…	13.9	A1; B1, B3, B4
1127−145	80.7	4.3	C	…	10.4	B1, B2; C1, C2; D1
1156+295	10.0	3.8	C	…	11.1	B1—B7
1219+285	106.2	10.6	C	…	8.0	B1—B4
1222+216	23.5	1.9	S	2014.11	4.7	A1, A2, A3
1226+023	−141.3	0.7	L	2013.79	4.3	B1—B22
1253−055	−152.7	1.0	S	2013.37	20.0	A1; C24—C38
1308+326	−64.9	4.7	C	…	12.9	B2—B6
1406−076	−81.9	7.2	C	…	14.5	B1—B5; C1
1510−089	−33.1	2.8	C	…	8.0	All except B10
1611+343	163.3	3.3	W	…	13.0	A2, A3; C1—C3
1622−297	−78.1	3.3	W	…	11.7	B4—B6
1633+382	−51.6	6.1	C	…	9.1	B1, B2, B4, B5, B7
1641+399	−100.5	2.6	W	…	8.6	B1—B15; C1—C3; D1—D3
1652+398	119.7	11.8	C	…	26.9	A2—A5; C2, C3
1730−130	−2.8	1.4	W	…	13.6	A1; B1—B7; C1; D; T2
1749+096	−1.2	2.3	S	2014.03	15.0	A1; B1—B10; C1; T5
1959+650	127.9	12.9	C	…	19.1	A1—A4
2200+420	−170.0	1.8	C	…	4.5	B1—B16; C1—C5; D1, D2; T3
2223−052	114.3	3.2	W	…	14.7	A1—A3; B1—B6; C1, C2; T5
2230+114	130.9	3.6	C	…	10.1	B1—B10; D1, D2
2251+158	−81.8	1.6	S	2012.67	2.5	C

Notes. P.A.s are measured north through east.
[a] Final fit to the jet position angle behavior, labeled as follows: C—$\langle\Theta_{\mathrm{jet}}(t)\rangle$ = constant, for which the value in Column 2 is used in subsequent analyses in this work; W—sources for which $\langle\Theta_{\mathrm{jet}}(t)\rangle$ = constant, but $\sigma_{\langle\Theta_{\mathrm{jet}}\rangle} > 3 \times \langle\sigma_\Theta\rangle$; L—linear dependence, $\langle\Theta_{\mathrm{jet}}(t)\rangle = a_1 * (t - t_{\mathrm{ave}}) + a_0$, where t_{ave} is the midpoint of the observed period; and S—a spline fit of the third order, $\langle\Theta_{\mathrm{jet}}(t)\rangle = \mathrm{spline}(t - t_{\mathrm{ave}})$.

Lac objects ∼3 such features. Our sample size of RGs is small; however, we see seven and five stationary features in 0415 +379 and 0430+052, respectively. Given the subrelativistic speeds of knots in 0316+413, it is hard to determine which features are truly stationary. Almost half of the stationary features in our sample have appeared or disappeared over time, indicating that while these features may be stationary in position, they are often transient features over timescales of ∼10 yr. Given that there is no way to average the properties of stationary features for a particular source into one overarching "typical" stationary feature, we treat each stationary feature as an independent feature when making comparisons between the subclasses of blazars.

Figure 10, left, shows the distribution of the average projected linear distances from the core of all stationary features in our sample. Five stationary components that appear beyond 15 pc from the core are included in the last bin. The

distribution has a prominent peak at distances <1 pc from the core, as in the distribution presented in Jorstad et al. (2017). In addition, there continues to be no statistical difference in the distributions of FSRQs, BL Lac objects, and RGs, with a K-S test yielding $\mathcal{D} = 0.159$ and $p = 0.601$ for the distributions of FSRQs versus BL Lac objects, $\mathcal{D} = 0.260$ and $p = 0.423$ for FSRQs versus RGs, and finally $\mathcal{D} = 0.221$ and $p = 0.642$ for BL Lac objects versus RGs.

Despite the "stationary feature" classification, the brightness centroids of many of these components do exhibit distinguishable motion. The locations of the majority of features tend to fluctuate about their mean reported positions. Figure 10, right, shows three examples of the trajectories of stationary features, one in each subclass. The range of motion in both R.A. and decl. is larger than the positional errors can account for, and the loci of (X, Y) positions of a given stationary feature form a pattern that indicates a preferred direction of motion for the
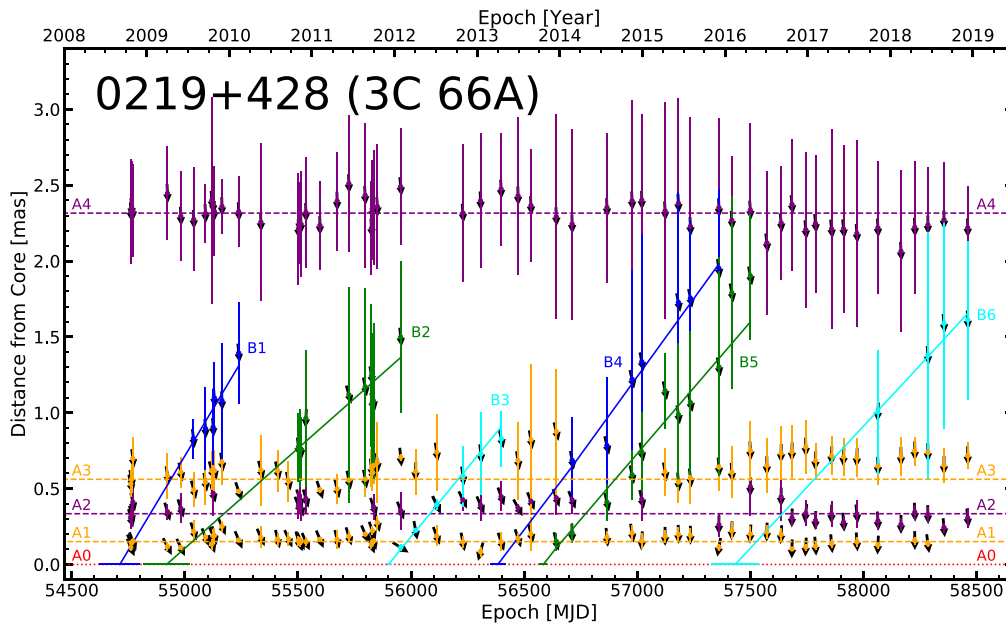
Figure 7. Separation vs. time of the knots in the jet of the BL Lac object 0219+428 (3C 66A). The colors of the knots—the same as in Figure 6—are coded based on their motion designation: blue, green, and cyan represent bright moving knots, orange and purple correspond to stationary components, and brown is used for trailing knots (appearing to split off from other knots), relatively faint moving features, or to differentiate between closely spaced knots. Red dotted lines are used to show the core component *A0*. Horizontal lines along *A0* indicate the uncertainty in time of the epoch of ejection. See the text for more details. Plots for all sources in the sample are available in the figure set.

(The complete figure set (38 images) is available.)

fluctuations. In order to characterize the shifts in position, we fit confidence ellipses to the motions of each stationary feature. Table 9 gives the parameters of the elliptical fits as follows: 1—source name; 2—knot designation; 3—number of observations, N, of a knot; 4—projected linear distance from the core to $\langle R \rangle$ of the knot, in parsecs; 5—mean position of the knot along the X-axis (relative R.A.), X_{cen}, in milliarcseconds; 6—mean position of the knot along the Y-axis (relative DEC), Y_{cen}, in milliarcseconds; 7—semimajor axis length, A, in milliarcseconds; 8—semiminor axis length, B, in milliarcseconds; and 9—orientation angle of semimajor axis relative to north, ϖ, in degrees. Figure 10, right panel, shows sample 2σ confidence ellipses for the given knots, where 2σ indicates that 95% of the observed data would lie within the ellipse if the data were normally distributed.

In this characterization of the knot motion dispersion, ϖ represents the angle of the motion along the major axis. We compare this direction of motion with the direction of the jet through $|\varpi - \langle \Theta_{jet} \rangle|$, as defined in Table 7. For sources with $\langle \Theta_{jet} \rangle$ fit by a linear trend or a spline, we average the trend over the dates of observation of the particular stationary feature. Figure 11, left, shows the distributions of this difference angle separately for FSRQs, BL Lac objects, and RGs. A K-S test between the distributions indicates that there is no statistical difference between the subclasses, with the FSRQ and BL Lac object distributions being the most similar ($\mathcal{D} = 0.162$, $p = 0.578$), while $\mathcal{D} = 0.318$, $p = 0.200$ for FSRQs versus RGs and $\mathcal{D} = 0.277$, $p = 0.357$ for BL Lac objects versus RGs.

We are able to separate the entire range of $|\varpi - \langle \Theta_{jet} \rangle|$ into three categories: (1) fluctuations along the jet, with $|\varpi - \langle \Theta_{jet} \rangle| \leqslant 30°$ or $|\varpi - \langle \Theta_{jet} \rangle| > 150°$, (2) fluctuations transverse to the jet direction, $60° < |\varpi - \langle \Theta_{jet} \rangle| \leqslant 120°$, and (3) oblique fluctuations with intermediate angle differences, $30° < |\varpi - \langle \Theta_{jet} \rangle| \leqslant 60°$ or $120° < |\varpi - \langle \Theta_{jet} \rangle| \leqslant 150°$.

Figure 11 shows the divisions between parallel and oblique cases with red dotted lines, while the division between oblique and transverse fluctuations is shown with blue dotted lines. In FSRQs, 40% (18/45) of knots fluctuate along the jet direction, 26.7% (12/45) oblique to the jet, and 33.3% (15/45) transverse to the jet. The situation is similar for BL Lac objects: 44.7% (17/38), 26.3% (10/38), and 28.9% (11/38), respectively. This is supported by the K-S test, which indicates that the FSRQ and BL Lac object distributions are not significantly different. The RG distribution, however, shows a clear preference for motions along the jet direction, with 11 of the 13 knots (92%) moving predominately along the jet direction. While the number of RG stationary features has increased over those detected in Jorstad et al. (2017), there are still only a relatively small number of such knots, so that the K-S test is inconclusive.

Almost all of the apparent motions of the quasi-stationary features appear to be minor fluctuations about the average positions. A clear trend in the motion is apparent only for knot C of the FSRQ 2251+158. Over ~10 yr of observations, this feature started ~0.7 mas from the 43 GHz core in 2007, after which the separation decreased to a minimum of ~0.45 mas in 2013. Since then, the separation has been increasing more gradually. It is unclear whether this motion is related to changes in the intensity distribution of this extended feature, or to bright knots that were ejected from the core and later merged with C. An alternative possibility is that the change in separation between the core and C in 2251+158 is due to the motion of the core itself, contrary to the assumption made in this work that every core is at an essentially stationary position in the jet.

Figure 12 shows distributions of the average flux density of the stationary features, $\langle S_{knot} \rangle$, normalized by the average flux density of the core, $\langle S_{core} \rangle$ for all three subclasses. A K-S test

Table 8
Velocity in the Jets

Source	Knot	N_{seg}	t_s[a] (yr)	t_e[a] (yr)	μ (mas yr^{-1})	Φ (deg)	β_{app} (c)	$t_\circ$ (yr)	Flag for $t_\circ$
(1)	(2)	(3)	(4)	(5)	(6)	(7)	(8)	(9)	(10)
0219+428	B1	1	2009.56	2010.11	0.915 ± 0.178	179.2 ± 4.0	24.62 ± 4.80	2008.67 ± 0.24	R
	B2	1	2010.84	2012.07	0.483 ± 0.058	-167.0 ± 4.9	13.01 ± 1.56	2009.24 ± 0.27	R
	B3	1	2012.07	2013.29	0.665 ± 0.070	-168.5 ± 11.7	17.89 ± 1.87	2011.93 ± 0.01	XY
	B4	1	2014.15	2015.93	0.751 ± 0.056	-170.2 ± 1.4	20.22 ± 1.50	2013.25 ± 0.08	XY
	B5	1	2013.96	2016.31	0.634 ± 0.050	-168.4 ± 2.1	17.07 ± 1.35	2013.80 ± 0.03	XY
	B6	1	2017.85	2018.94	0.605 ± 0.067	-165.6 ± 5.7	16.28 ± 1.79	2016.12 ± 0.28	R
0235+164	B1	1	2007.66	2008.62	0.533 ± 0.025	-18.3 ± 3.5	26.58 ± 1.27	2007.45 ± 0.01	XY
	B2	1	2008.62	2009.62	0.258 ± 0.024	140.3 ± 4.9	12.88 ± 1.18	2008.15 ± 0.11	R
	B3	1	2010.58	2013.96	0.051 ± 0.004	147.1 ± 4.8	2.55 ± 0.21	2008.10 ± 0.32	R
	B4	1	2013.49	2016.31	0.107 ± 0.014	-124.2 ± 8.9	5.32 ± 0.68	2012.62 ± 0.26	R
	B5	1	2016.08	2017.67	0.183 ± 0.017	66.7 ± 4.8	9.13 ± 0.87	2015.54 ± 0.15	XY
	B6	1	2016.91	2018.65	0.120 ± 0.013	13.4 ± 8.0	6.00 ± 0.63	2015.42 ± 0.51	R
	B7	1	2018.30	2018.79	0.191 ± 0.046	52.3 ± 16.3	9.55 ± 2.28	2016.55 ± 0.95	R
0336−019	B1	1	2007.75	2009.15	0.617 ± 0.032	81.4 ± 1.4	28.57 ± 1.50	2007.30 ± 0.02	XY
	B2	1	2008.81	2009.50	0.227 ± 0.003	81.2 ± 4.3	10.50 ± 0.13	2008.37 ± 0.16	R
	B2	2	2009.50	2010.45	0.650 ± 0.001	86.9 ± 1.5	30.11 ± 0.05	$\ldots$	$\ldots$

Note.
[a] Knots with a single motion segment have no error in their start and end times, as these are the first and last observations of the knot, respectively. The typical error on the segment start and end times for knots fit with multiple segments is $\sigma_T \lesssim 0.01$ yr and is determined from the covariance matrices of fit parameters in the least-squares piecewise linear fitting.

(This table is available in its entirety in machine-readable form.)

confirms the distributions for each subclass are similar, with $\mathcal{D} = 0.201$, $p = 0.319$ for FSRQs versus BL Lac objects, $\mathcal{D} = 0.244$, $p = 0.501$ for FSRQs versus RGs, and $\mathcal{D} = 0.223$, $p = 0.628$ for BL Lac objects versus RGs.

Finally, we investigate whether the stationary and moving features in the jets have distributions of knot-to-core flux density ratios that are statistically different within a subclass. We calculate the average $\langle S_{knot} \rangle$, median, and maximum flux density of each knot and normalize them by the average flux density of the core, $\langle S_{core} \rangle$. Figure 13 displays the distributions of flux ratios for stationary features (left) and moving features (right) separately for each subclass. There is no statistical difference between the flux ratios of the stationary and moving features in RGs according to a K-S test ($\mathcal{D} = 0.333$, $p = 0.133$). The hypothesis of different distributions in FSRQs is similarly rejected ($\mathcal{D} = 0.191$, $p = 0.110$). In BL Lac objects, however, there is a moderately significant result that the stationary features of BL Lac objects have higher flux ratios than do the moving features ($\mathcal{D} = 0.275$, $p = 0.019$). The flux distributions and K-S statistics for the average and maximum flux ratios of stationary and moving components show a similar trend, but are not included here for brevity.

4.3. Knot Acceleration and Deceleration

Between 2007 and 2018, 75 of the 425 (17.6%) moving knots detected in our sample exhibit nonballistic apparent velocities, which we define as motions that are best fit by multiple line segments in a piecewise fashion. We also include the quasi-stationary feature C of the FSRQ 2251+158 in the following analysis, as it has been reliably observed to have motion around the average stationary value. Across the three subclasses, we have detected acceleration in 55 features in 16 FSRQs, nine features in six BL Lac objects, and 11 features in the three RGs. Due to the nature of our piecewise linear fits, the trajectories of many of these knots contain multiple acceleration regions. This

totals 104 individual acceleration regions in the jets of 25 blazars in our sample. Given that the multiple acceleration regions may have different properties, we consider each region to be an independent measurement of possible acceleration within a particular subclass of blazar, and do not calculate a "typical" acceleration for each source. Table 10 gives the accelerations of each region in each knot as follows: 1—name of the source; 2—designation of the component; 3—acceleration region number, N_{acc}; starting with 1 for the first region present (between moving segments 1 and 2) in a knot trajectory and reaching a maximum of 4 for a knot that is best fit by three linear segments in both the X and Y directions; 4—beginning date of the acceleration, t_{start}; 5—end date of the acceleration, t_{end}; 6—the acceleration parallel the jet, $\dot{\mu}_\parallel$, and its 1σ uncertainty in mas yr^{-2}; 7—the acceleration perpendicular to the jet, $\dot{\mu}_\perp$, and its 1σ uncertainty in mas yr^{-2}; 8—$R_{\dot{\mu}}$, the distance from the core to the position of the knot based on the estimated time break point (from the piecewise fit), in milliarcseconds; 9—the normalized acceleration parallel to the jet, $\eta_\parallel$, and its 1σ uncertainty in yr^{-1}; and 10—the normalized acceleration perpendicular to the jet, $\eta_\perp$, and its 1σ uncertainty in yr^{-1} (see below for definitions of $\eta_\parallel$ and $\eta_\perp$). As discussed in Section 3.2, the accelerations parallel and perpendicular to the jet were determined using the averaged position angle for sources with constant or wide jets and using the linear or spline trend to calculate the jet position angle at the time of acceleration for those with time-variable jet positions. In this way, we separate the time variability of the jet as a whole from the change in directions of knots relative to the bulk flow.

The accelerations found in the jets of RGs are primarily in 0415+379 (8/11, 72.7%). Several knots in this source show very complex motions, requiring more than two acceleration regions. Accelerations occur in only one knot in 0430+052. In contrast, only a few BL Lac objects exhibit any acceleration, and only one BL Lac object (2200+420) contains a knot ($C2$) that shows complex enough motion to have more than two
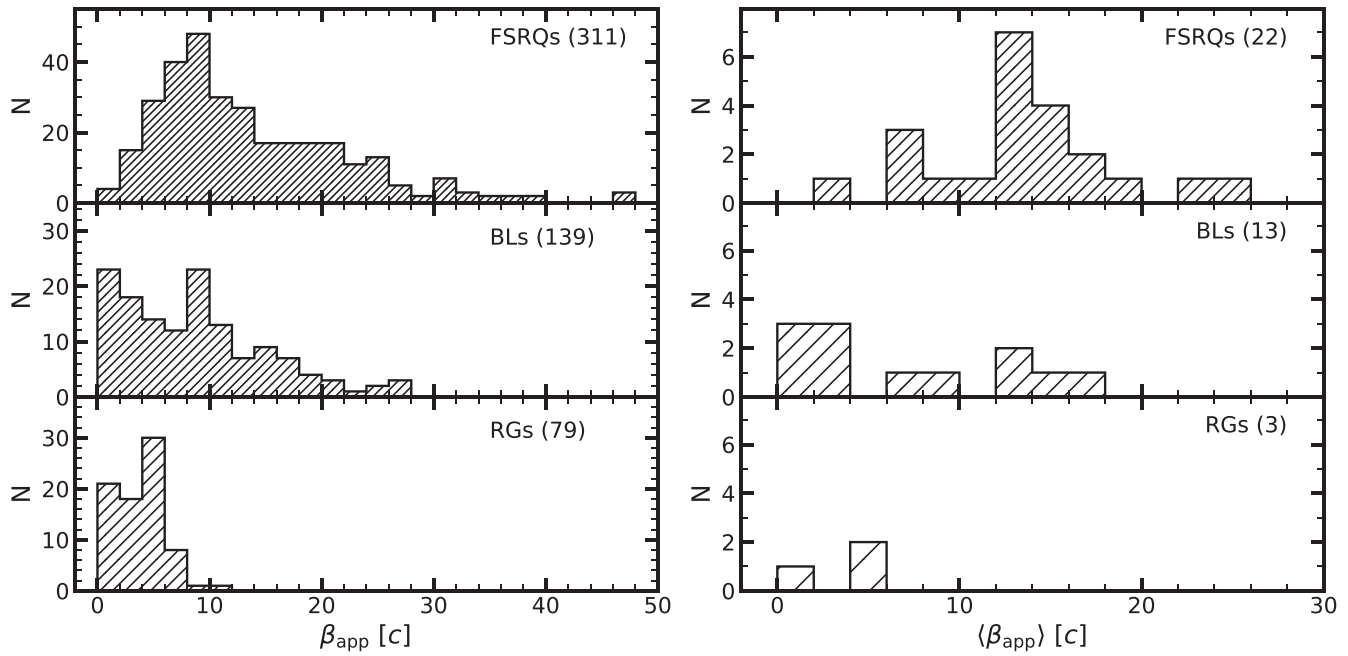
Figure 8. Distributions of the apparent speeds of all moving knots (left), and weighted average of the apparent speed for each source (right) detected in FSRQs (top), BL Lac objects (middle), and RGs (bottom).
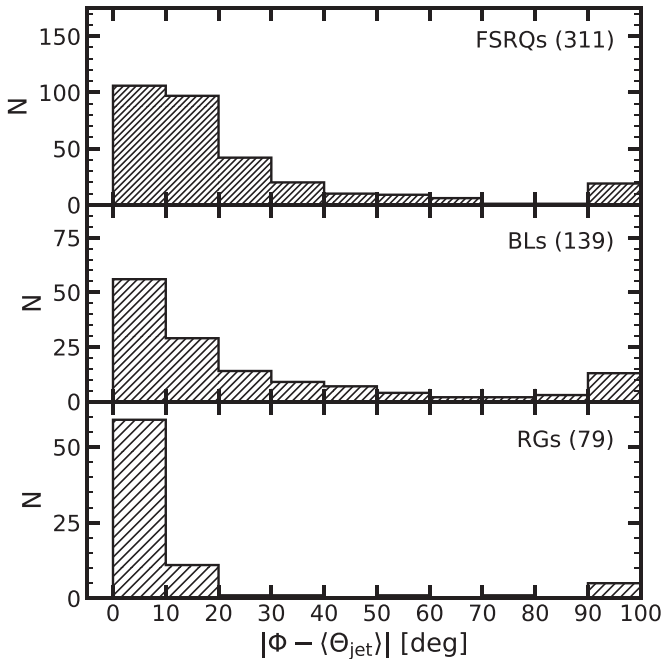

Figure 9. Distributions of the differences between the velocity vector, Φ, and the jet axis, $\langle\Theta_{jet}\rangle$, in FSRQs (top), BL Lac objects (middle), and RGs (bottom).$|\Phi - \langle\Theta_{jet}\rangle| > 90°$ indicates slow or upstream motion of the knot segment.

acceleration zones. A much wider variety of knots are found to have accelerated in FSRQs, but again a few sources dominate in terms of the number of regions (such as 1226+023, with 21 regions for 13 knots).

Due to the fact that the 3D motion is projected onto the 2D plane of the sky, we cannot distinguish whether the acceleration in a given knot is connected with an intrinsic change in speed (and thus in the Lorentz factor Γ) or with a change in the intrinsic viewing angle Θ_o. To resolve this ambiguity, we

follow the statistical approach suggested by Homan et al. (2009) and followed by Jorstad et al. (2017): If, in a flux-limited sample of beamed jets, the observed relative parallel acceleration exceeds ~60% of the observed relative perpendicular acceleration (averaged over the sample), then the observed accelerations are caused more by variations in the Lorentz factors of the knots than by changes in the jet direction.

We compute the relative accelerations in our jets following a formalism similar to that of Homan et al. (2009), adapted for our fitting procedure: the acceleration parallel to the jet is $\eta_{\parallel} = (1 + z)\dot{\mu}_{\parallel}/\mu_i$, while acceleration perpendicular to the jet direction is $\eta_{\perp} = (1 + z)\dot{\mu}_{\perp}/\mu_i$, where μ_i in both cases refers to the pre-acceleration proper motion of the knot. Averaging over the entire sample, we find $\langle\eta_{\parallel}\rangle = 0.678$ yr^{-1} and $\langle\eta_{\perp}\rangle = -0.056$ yr^{-1}, thus, $|\langle\eta_{\parallel}\rangle| > 0.6|\langle\eta_{\perp}\rangle|$ and the observed accelerations are likely caused by changes in the Lorentz factors rather than changes in the jet direction.

One advantage of the piecewise linear fits used in this work (instead of the polynomial fits presented in Jorstad et al. 2017) is that, since the accelerations can be seen to take place at specific locations in the jet, it is straightforward to determine the distance from the 43 GHz core to the acceleration zone. Figure 14, left, shows the computed relative accelerations with respect to the angular distance from the core to the acceleration region, while the right panel shows the same relative accelerations as functions of the average projected linear distance from the core to the acceleration region. While the accelerations in RGs tend to appear to occur closer to the core than the accelerations in FSRQs and BL Lac objects, this is due to the observational bias that the RG redshifts are smaller than those of the other subclasses. Given that there are no distinct differences in relative acceleration between the subclasses, we consider all accelerations together.

We bin both $\eta_{\parallel}$ and $\eta_{\perp}$ for all sources by distance from the 43 GHz core of the jet, and construct histograms of the accelerations in Figure 15. Distance bins are chosen so that a significant number of knot accelerations would be present in
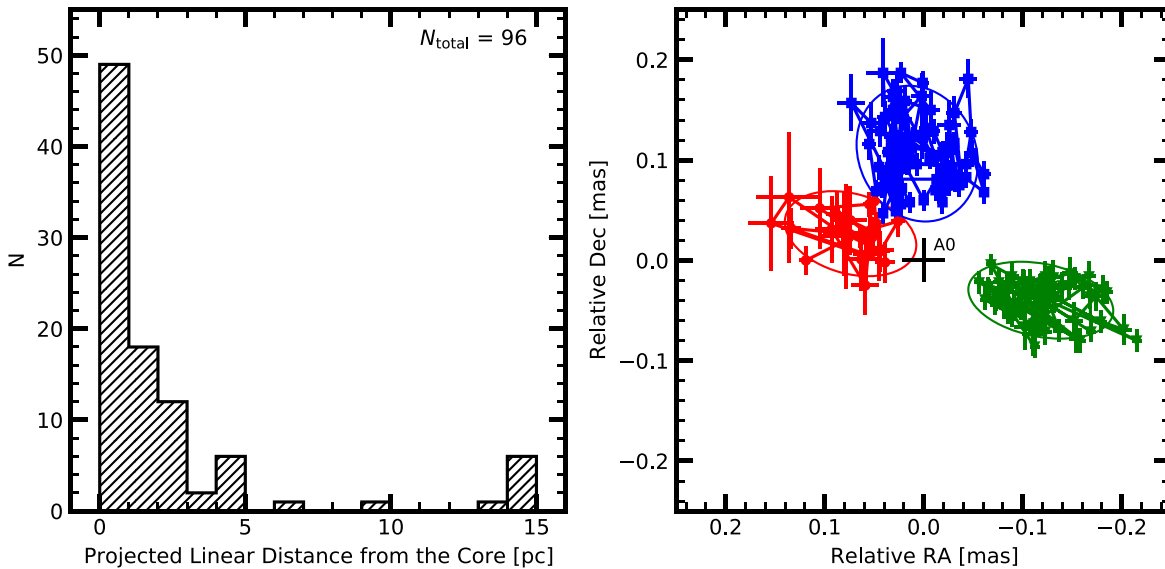
Figure 10. Left: distribution of the projected distances from the core to the stationary features in our sample. Right: trajectories of the stationary features *A1* in 0528+134 (FSRQ, red circles), *A2* in 1749+096 (BL, blue squares), and *A1* in 0430+052 (RG, green triangles) with respect to the core, *A0* (the black cross at position (0,0)). The solid lines show 2σ confidence ellipses used to characterize the dispersion and orientation of the knot motion.

each bin ($\gtrsim 10$) while also maintaining adequate distance spacing. The left panels display $\eta_{\parallel}$, while those on the right show $\eta_{\perp}$. In the distributions, the red vertical lines indicate the median values, which are listed in Table 11.

From inspection of the distributions of $\eta_{\parallel}$, it is apparent that accelerations close to the core are positive, increasing the speed at which knots flow down the jet axis. As the distance from the core increases, the magnitude of this acceleration generally decreases. Once knots reach distances of $\sim$5–10 pc from the core, most accelerations are negative. While this work at 43 GHz probes projected distances of $\sim$0–35 pc from the core, data at 15 GHz (Homan et al. 2015) probes farther out, up to $\sim$100 pc projected distance from the core. The data at longer wavelengths supports our results here, with a general turnover from positive to negative/no acceleration beyond $\sim$10–20 pc projected distance. This result indicates that, although the overall diversity in apparent speeds likely requires a variety of different shock strengths if the knots are shock waves (e.g., Marscher & Gear 1985), it is common for accelerations to occur close to the core and for constant speeds or decelerations to dominate farther downstream ($\sim 10^2$ pc deprojected distance).

The distributions of $\eta_{\perp}$ indicate a different behavior of the knot motions perpendicular to the jet axis. Beyond $\sim$2 pc from the core, the acceleration distributions are consistent with low, if any, acceleration transverse to the jet axis. However, initially there appears to be positive acceleration, resulting in knot motion away from the jet axis. This could be due to bends in the jet close to the core or a widening of the jet flow. The motion is reversed for distances $\sim$1–2 pc, where there is negative acceleration. This could be an indication of recollimation of the jet flow, such that the jet width narrows or remains constant downstream of this point. Stacking of the 43 GHz images of jets can be used to investigate the jet width (e.g., Pushkarev et al. 2017; Kovalev et al. 2020; Casadio et al. 2021) and test whether the acceleration trends are actually related to the jet width.

An important question is whether accelerations are related to the stationary features in the jets, as one might expect if the

features represent standing shocks. To test this, Figure 16 displays the relationship between the locations of each acceleration region and the closest stationary feature. The gray dotted line depicts a 1:1 relationship between the two, i.e., where the positions of acceleration and a stationary feature are the same. We have used the standard deviation of the stationary feature position as the uncertainty in the distance from the core to the closest stationary feature. We have assigned a positional error of 0.02 mas ($\sim$0.2 times our best resolution) to the distance from the core to the acceleration region.

Very few pairs of acceleration region and stationary feature fall below the 1:1 relationship line. This indicates that most accelerations occur at or beyond stationary features. An example of this trend is readily seen in the FSRQ 0336−019, where knots *B2, B3,* and *B4* appear to accelerate after passing through stationary features *A1* and *A4*. Such behavior is expected if the stationary features are structural components in the jet that can interact with moving features, such as recollimation shocks. The interpretation of recollimation shocks is further supported by the acceleration distributions for projected distances $\sim$1–4 pc, which are predominately negative for $\eta_{\perp}$.

5. Physical Parameters of Jets

The trajectories, apparent velocities, and light curves derived for moving features can be used to compute important physical parameters in the parsec-scale jets of the blazars in our sample. These parameters are: variability Doppler factor $\delta_{\rm var}$, Lorentz factor Γ of the motion, viewing angle $\Theta_\circ$, and opening semi-angle $\theta_\circ$ of the jet. We restrict the following analysis to the most "reliable" features, which we define as those with a number of images in which the feature is visible $N \geqslant 6$, and ejection times within our observed period of VLBA monitoring. The resulting sample includes 191, 101, and 46 knots in FSRQs, BL Lac objects, and RGs, respectively. Each knot can have multiple values of speed, depending on the number of line segments used in the piecewise linear fit. This leads to a total of 262, 109, and 58 potential measurements of the physical

Table 9
Quasi-stationary Jet Features

Source	Knot	N	$\langle R \rangle$ (pc)	X_{cen} (mas)	Y_{cen} (mas)	A (mas)	B (mas)	ϖ (deg)
(1)	(2)	(3)	(4)	(5)	(6)	(7)	(8)	(9)
0219+428	A1	52	0.97 ± 0.23	-0.04	-0.16	0.08	0.06	21.9
	A2	36	2.11 ± 0.34	-0.08	-0.35	0.15	0.10	-127.7
	A3	50	3.71 ± 0.51	-0.07	-0.64	0.19	0.11	-21.7
	A4	56	13.20 ± 0.51	-0.12	-2.31	0.18	0.11	-3.3
0336–019	A1	36	1.23 ± 0.31	0.14	0.02	0.10	0.08	13.9
	A2	7	14.64 ± 0.84	1.77	0.69	0.28	0.21	16.0
	A3	8	2.15 ± 0.23	0.27	0.07	0.11	0.04	-46.4
	A4	11	3.14 ± 0.46	0.39	0.11	0.17	0.09	-41.8

(This table is available in its entirety in machine-readable form.)
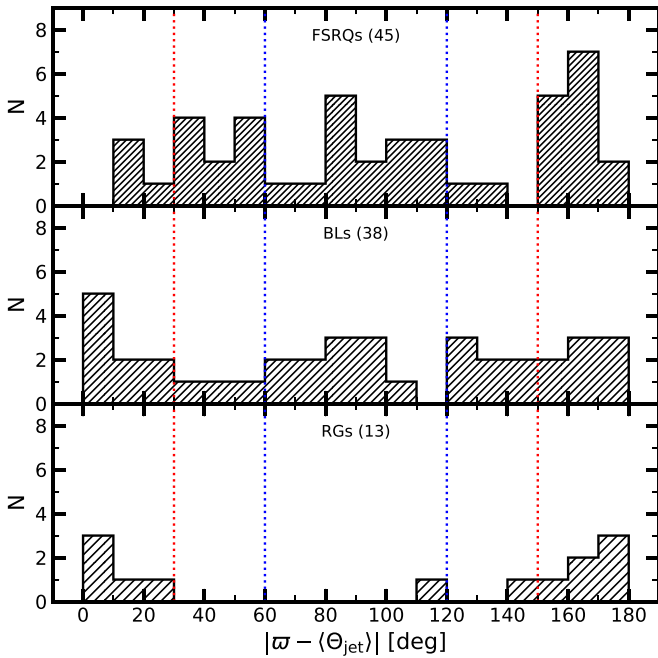
Figure 11. Distributions of the differences between the major axis orientation angles, ϖ, and $\langle \Theta_{jet} \rangle$, in FSRQs (top), BL Lac objects (middle), and RGs (bottom). See the text for details.

parameters in the jets of FSRQs, BL Lac objects, and RGs, respectively.

5.1. Variability Timescale and Doppler Factor

We follow the formalism developed by Jorstad et al. (2005) and modified in Jorstad et al. (2017) to calculate the timescale of variability, τ_{var}, and variability Doppler factor, δ_{var}, for the moving knots in our sample. In this method, we assume that for the majority of superluminal knots, the flux density at 43 GHz declines from radiative energy losses of the relativistic electrons rather than adiabatic cooling. If this decay (calculated in the rest frame of the jet plasma) is also shorter than the light-travel time, as we assume, the Doppler factor can be determined as

$$\delta_{var} \approx \frac{16 s D_{Gpc}}{\tau_{var}(1+z)}, \quad (5)$$
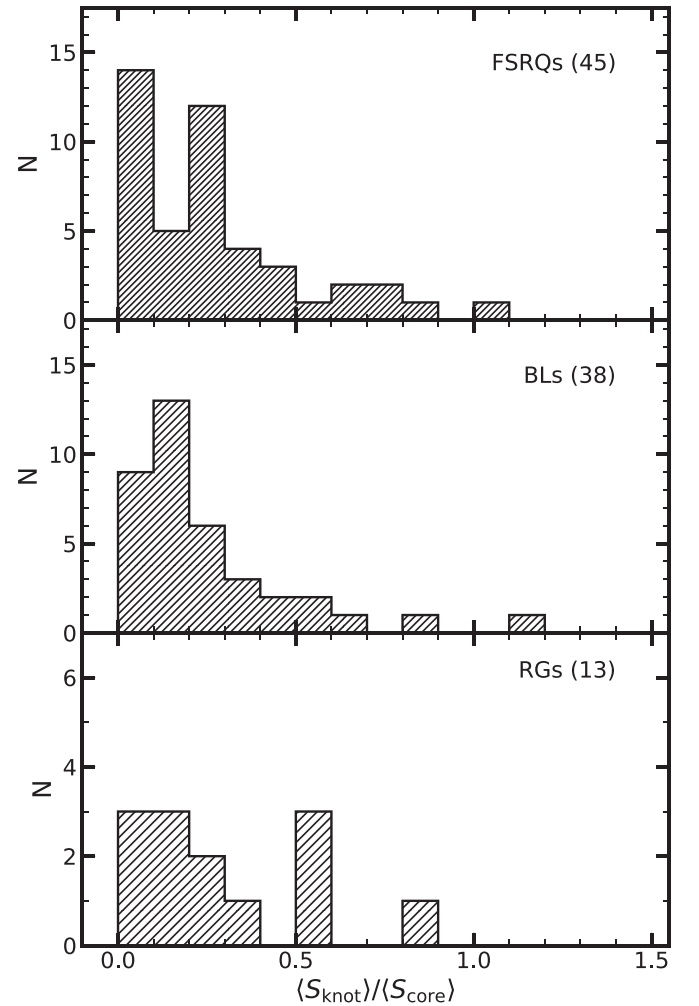
Figure 12. Distributions of the relative flux densities of quasi-stationary features for the different subclasses—FSRQs (top), BL Lac objects (middle), and RGs (bottom).

where D_{Gpc} is the luminosity distance to the source in gigaparsecs, τ_{var} is measured in years, z is the redshift of the host galaxy, and s is the angular size of the knot in milliarcseconds.

In order to estimate τ_{var}, we make use of the fact that the rise and decay portions of the millimeter-wave light curves of
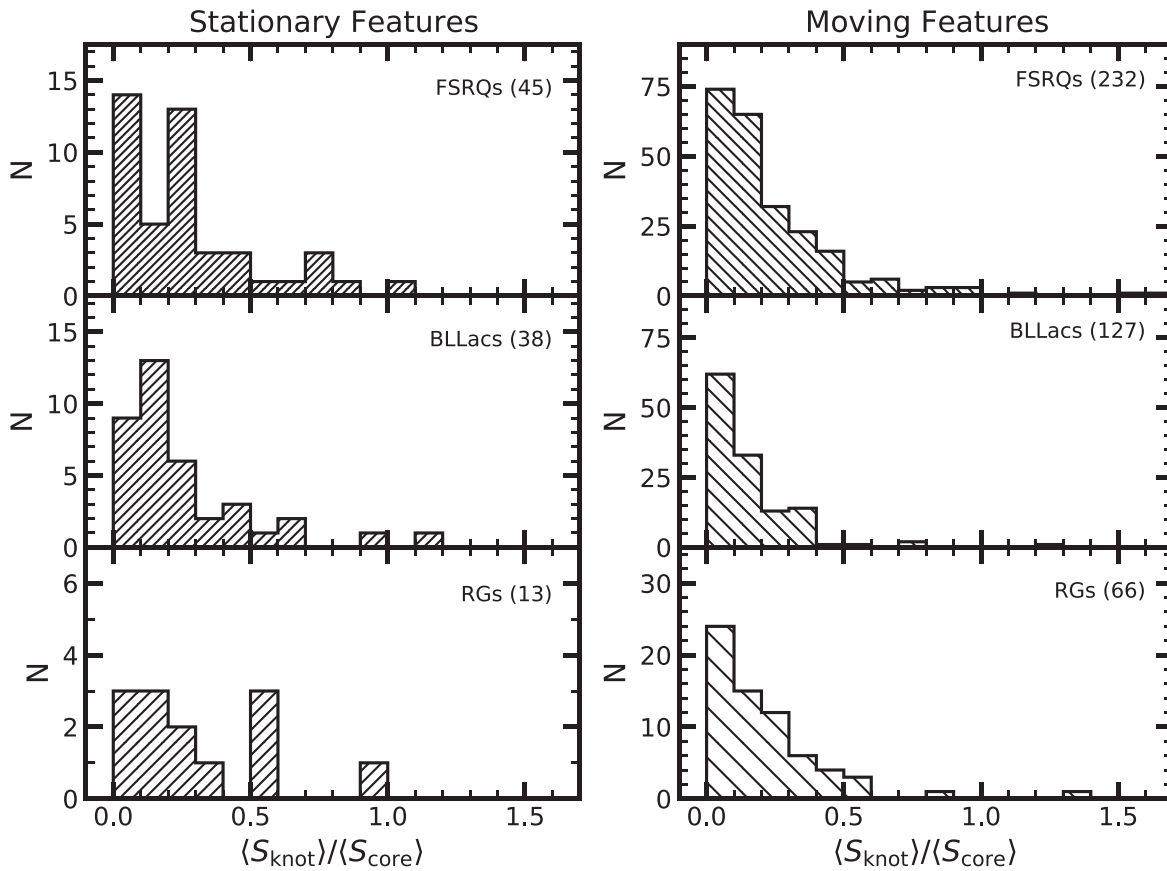
Figure 13. Distributions of the average flux of a knot relative to the average flux of the core, $\langle S_{core} \rangle$, for the stationary (left) and moving (right) features in FSRQs (top), BL Lac objects (middle), and RGs (bottom).

blazars can both be roughly modeled by exponential profiles, so that $\ln S(t) \propto t$ (Terasranta & Valtaoja 1994; Lister 2001). Such millimeter-wave flares in blazars occur roughly at the same time as the emergence of a new knot from the core, and the decay of the flux density of a knot resembles that of the total flux density (Savolainen et al. 2002). We thus approximate the flux decay of the reliable knots in our sample with an exponential of the form $\ln(S(t)/S_\circ) = k(t - t_{max})$, where $t_{max} \leqslant t$ is the epoch corresponding to the maximum flux density, S_{max}, $S_\circ$ is the flux density of a least-squares fit to the light curve decay at time t_{max}, and k is the slope of the fit. The timescale of variability is then $\tau_{var} = |1/k|$ yr. While τ_{var} for most knots can be determined to within $\sim 10\%$, some light curves have no well-defined maximum given the time coverage of the observations, which leads to significant uncertainty in the timescale of variability. Because of this, we remove knots from our reliable sample if $\sigma_{\tau_{var}} > \tau_{var}/2$. We also cut from our analysis motion segments beyond the first acceleration zone for knots with complex motion. This reduced sample consists of estimates for the physical parameters of 162 knots in 22 FSRQs, 80 knots in 11 BL Lac objects, and 31 knots in two RGs. The remaining three sources either have no reliable moving knots with defined epochs of ejections (the RG 0316 +413 and the BL Lac object 1652+398) or no moving features at all identified in this work (the BL Lac object 1959+650). While we use the superluminal knots of the BL Lac object 1101 +384 to determine its jet parameters, the low apparent speeds suggest that we are looking at a sheath of the jet rather than the region closer to the axis (see Section 5.3).

Figure 17 shows the decay light curves and the fits used to calculate τ_{var} for a knot in each subclass, shifted for clarity. The distributions of the timescales of variability, corrected for redshift to transform into the host-galaxy frame, are similar for all three subclasses, peaking at $\tau_{var}^s \lesssim 6$ months with the majority ($\gtrsim 80\%$) of all knots having a timescale $\tau_{var}^s < 1$ yr.

In order to test the assumption that the flux density decay of knots at 43 GHz is due primarily to radiative losses rather than adiabatic expansion, we also fit an exponential of the form $\ln(a(t)/a_\circ) = k_a(t - t_{max})$ to the knot sizes, $a(t)$, over the same epochs as used to calculate the flux timescale of variability. Here, $a_\circ$ is the size of the knot according to a least-squares fit to the data at time t_{max} (defined above) and $\tau_a = |1/k_a|$ yr. Figure 18 shows the timescale of variability of knot size compared to that of the flux density for individual knots. We have classified knots as having reliable values of the timescale for changes in size if $\tau_a \geqslant 2\sigma_{\tau_a}$, where $\sigma_{\tau a}$ is the estimated uncertainty. In the figure, the dotted gray line indicates the approximate relation between τ_a and τ_{var} for adiabatic losses for optically thin shocked gas with $\alpha = 0.7$ (Marscher & Gear 1985). A substantial majority (188/287, 65.5%) of knots have $\tau_{var} < \tau_a$ (above the dotted line), implying that the flux density decay is due predominantly to radiative losses rather than adiabatic losses, and thus that our initial assumption is valid.

The angular size a obtained in the model fits is the FWHM of a presumed Gaussian brightness distribution. We consider a face-on disk to be a more physically appropriate geometry, and therefore convert a to the diameter s of a face-on disk that has a

Table 10
Acceleration in the Jets

Source	Knot	N_{acc}	t_{start}[a] (yr)	t_{end}[a] (yr)	$\dot{\mu}_{\parallel}$ (mas yr^{-2})	$\dot{\mu}_{\perp}$ (mas yr^{-2})	$R_{\dot{\mu}}$ (mas)	$\eta_{\parallel}$ (yr^{-1})	$\eta_{\perp}$ (yr^{-1})
(1)	(2)	(3)	(4)	(5)	(6)	(7)	(8)	(9)	(10)
0316+413	C1a	1	2014.69	2017.58	0.127 ± 0.003	0.015 ± 0.023	2.86	0.538 ± 0.016	0.064 ± 0.098
	C10	1	2016.32	2016.89	-1.778 ± 0.073	-0.209 ± 0.307	1.19	-1.558 ± 0.069	-0.183 ± 0.269
	C10	2	2016.89	2018.04	0.404 ± 0.037	0.047 ± 0.077	1.24	1.827 ± 0.289	0.213 ± 0.349
0336−019	B2	1	2009.16	2009.98	0.508 ± 0.013	0.102 ± 0.064	0.25	4.145 ± 0.119	0.832 ± 0.522
	B3	1	2011.63	2013.88	0.075 ± 0.002	0.015 ± 0.009	0.28	1.094 ± 0.039	0.219 ± 0.131
	B4	1	2015.33	2016.94	0.222 ± 0.005	0.044 ± 0.026	0.46	2.056 ± 0.051	0.407 ± 0.241

Note.

[a] We take the typical uncertainties in the estimated start and end dates of the acceleration region to be similar to the uncertainty in the break points for the piecewise linear fitting, which are $\sigma_t \lesssim 0.01$ yr. The uncertainties in the acceleration are dominated by the uncertainty in the speeds rather than the time period of acceleration.

(This table is available in its entirety in machine-readable form.)

similar interferometric visibility function, $s = 1.6a$, for use in Equation (5). We estimate a as the average over the epochs used to calculate τ_{var}, so that $a = \sum_{i=1}^{n} a_i/n$, where a_i is the FWHM size of the knot at each epoch i and n is the number of epochs in the decay phase of the light curve. Table 12 presents the physical parameters of each knot segment as follows: 1—source name; 2—knot designation; 3—timescale of variability of the knot flux density, τ_{var}, and its estimated 1σ uncertainty from the least-squares fit to the decay of the light curve, in years; 4—average size of the knot, $\langle a \rangle$, and its propagated 1σ uncertainty, in milliarcseconds; 5—number of measurements used to calculate τ_{var} and $\langle a \rangle$; N_t; 6—Doppler factor of variability for each knot segment, δ_{var}, and its 1σ uncertainty; 7—bulk Lorentz factor of each knot segment, Γ, and its 1σ uncertainty (see Section 5.2); and 8—intrinsic viewing angle of each knot segment, $\Theta_\circ$, and its 1σ uncertainty, in degrees (see Section 5.2).

For comparison with past literature, Figure 19 (left) displays the distributions of the Doppler factors for all reliable knots derived using the above method. The Doppler factors of FSRQs and BL Lac objects are predominantly $\delta_{var} < 40$, with only eight and three segments having $\delta_{var} > 50$, respectively. These few knots are shown in the last bins of each distribution.

To more appropriately compare between the subclasses, we show in Figure 19 (right) the distributions of δ_{var} for "typical" knots of each source, where the "typical" knot has been determined through the method outlined in Section 5.3. We see that the δ_{var} values in RGs are substantially lower than those of FSRQs and BL Lac objects. This result is statistically significant $\sim 3\sigma$ when using a K-S test to compare the FSRQ and RG distributions ($\mathcal{D} = 0.955$, $p = 0.003$) but not when comparing the BL Lac object to RG distribution ($\mathcal{D} = 0.769$, $p = 0.071$) due to the relatively low number of RG sources in our sample. The FSRQ and BL Lac object distributions appear very similar (according to a K-S test; $\mathcal{D} = 0.311$, $p = 0.333$). However, this simple summary statistic hides an important distinction between the δ_{var} values of FSRQs and BL Lac objects. More than half (8/13, 61.5%) of the BL Lac objects have a typical $\delta_{var} \lesssim 15$, while in FSRQs, more than half (12/22, 54.5%) of the sources have $\delta_{var} \gtrsim 15$. This higher probability for FSRQs to have larger δ_{var} values is consistent with their observed higher brightness temperatures of jet features as compared to BL Lac objects, apparent in Figure 5.

5.2. Lorentz Factors and Viewing Angles

With the apparent speeds and Doppler factors derived for each knot, we can independently calculate the Lorentz factor Γ and viewing angle $\Theta_\circ$ with the relations

$$\Gamma = \frac{\beta_{app}^2 + \delta_{var}^2 + 1}{2\delta_{var}}; \quad \tan\Theta_\circ = \frac{2\beta_{app}}{\beta_{app}^2 + \delta_{var}^2 - 1}. \quad (6)$$

Figure 20, left panel, displays the distributions of Γ for all reliable knots of each subclass. The FSRQ and BL Lac object distributions both peak at $\Gamma \sim 10$, but BL Lac objects have a small local peak in the $\Gamma = 2$–6 bins, while the FSRQ distribution has a longer high-Γ tail. There is a single FSRQ knot for which $\Gamma \geqslant 60$, B1 in 0528+134, with $\Gamma = 81 \pm 10$; it is placed in the highest bin in the distribution. The RG distribution is comparatively narrow and low-valued, with all but one of the knots having $\Gamma < 10$. To directly compare the Lorentz factors of FSRQs, BL Lac objects, and RGs, we utilize a K-S test on the distributions of Γ for the "typical" knots of each source (see Section 5.3), shown in Figure 20 (right panel). Despite the low number of sources, we continue to infer that RGs have the slowest knots ($\Gamma \lesssim 10$), while FSRQs have, on average, faster knots, with a long tail (Γ extending up to ~ 60). Both FSRQ and BL Lac object distributions are statistically different from the RG distribution ($\sim 2\sigma$), with FSRQ versus RG $\mathcal{D} = 0.955$, $p = 0.003$, while the BL Lac objects versus RG $\mathcal{D} = 0.846$, $p = 0.036$. The K-S test cannot distinguish between the FSRQ and BL Lac object distributions, however, with $\mathcal{D} = 0.269$ and $p = 0.495$.

Figure 21 plots the distributions of the viewing angles for all reliable knots in the three subclasses. It is immediately apparent that RGs have a very different distribution than the FSRQs and BL Lac objects, peaking in the 16°–18° bin, with all knots having $\Theta_\circ > 10$. Minor differences can be seen between the FSRQ and BL Lac object distributions, such as the longer high-angle tail of the BL Lac objects. The peaks are also different, with the FSRQ distribution peaking between 0° and 2°, while the BL Lac object distribution peaks in the 2°–4° range. In both subclasses, however, the majority (>75%) of knots have $\Theta_\circ < 10$. Again to compare between the subclasses statistically, we use the viewing angle of a "typical" knot (see Section 5.3) for each source. The distributions for each subclass are shown in Figure 21. The FSRQs are more centrally located around the peak in viewing angle, $\Theta_\circ \sim 2$°–4°, than the BL Lac objects, but with a K-S test indicating
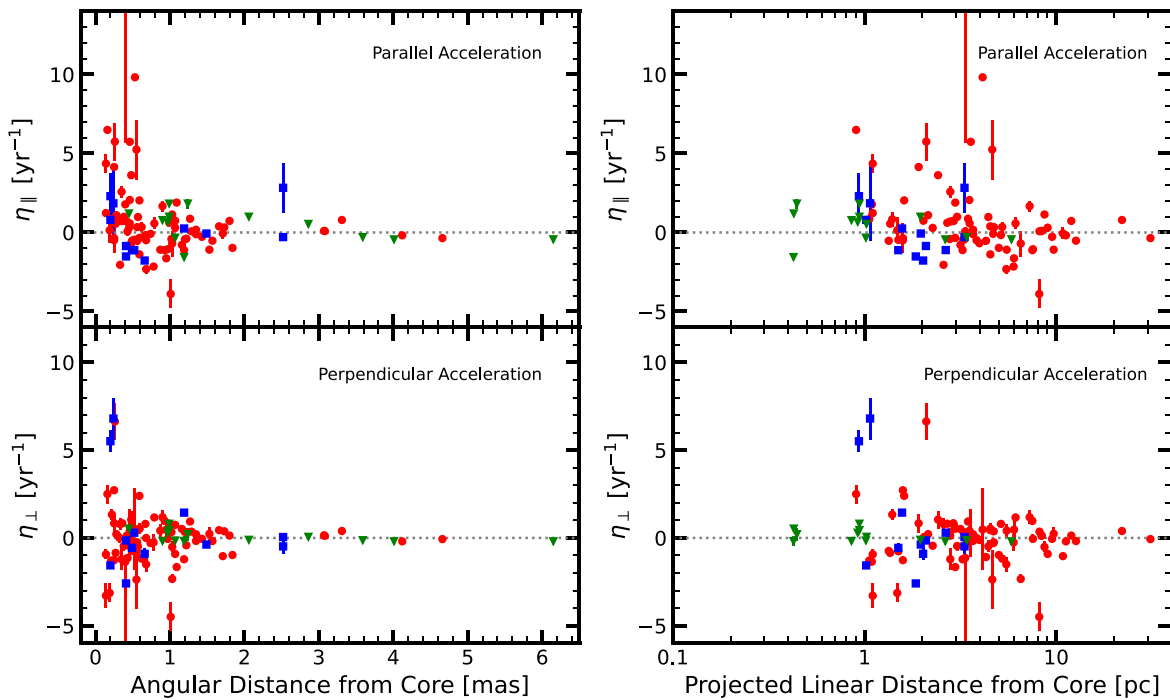
Figure 14. Left: relative accelerations parallel (top) and perpendicular (bottom) to the jet of moving knots in FSRQs (red circles), BL Lac objects (blue squares), and RGs (green triangles) vs. their angular distances from the core of the jet. Right: the same accelerations vs. the average projected linear distance downstream of the core.

$\mathcal{D} = 0.231$, $p = 0.678$. The RG distribution is statistically different from the other two subclasses, with $\mathcal{D} = 0.955$, $p = 0.003$ for the FSRQs versus RGs and $\mathcal{D} = 0.769$, $p = 0.071$ for the BL Lac objects versus RGs, despite the low number of sources.

5.3. Average Jet Physical Parameters and Opening Angles

According to Table 12, for any individual source, there is a diversity in knot properties, which complicates the determination of the characteristic physical conditions in the jet. The physical parameters of many jets are evidently time-variable, perhaps stochastically determined from a distribution of possible values. As an example, Figure 22 shows the distributions of the physical parameters δ_{var}, Γ, and $\Theta_\circ$ of the reliable knots of the RG 0415+379. The distributions can be approximated by Gaussian functions, with means $\mu = 2°\!.6$, $5°\!.8$, and $16°\!.3$ and standard deviations $\sigma = 0°\!.7$, $3°\!.1$, and $5°\!.0$, respectively, for δ_{var}, Γ, and $\Theta_\circ$. However, these well-determined distributions are the exception, since the number of knots observed in our study is more limited for most of the sample. The majority of sources have $N \leqslant 15$, too few to fit Gaussian distributions to the data accurately. Given the knot ejection rates of the sources observed in our sample, another $\sim$10 yr of monitoring would be required to observe enough knots to define the distributions of physical parameters for all objects.

Instead of analyzing tentative distributions of physical parameters of jets in our sample, we instead focus on "representative" values. For each reliable knot, we calculate a metric of overall uncertainty, $\xi \equiv \sqrt{\sigma_{\delta_{\text{var}}}^2 + \sigma_{\beta_{\text{app}}}^2}$, where $\sigma_{\delta_{\text{var}}}$ and $\sigma_{\beta_{\text{app}}}$ are the uncertainties in the variability Doppler factor and proper motion. We focus on these two parameters, since they factor directly into the determination of Γ and $\Theta_\circ$ (both given in Equation (6)), as well as the opening semi-angle (described below). We then choose as "representative" the knot

from the reliable sample of each jet that has the optimal combination of relatively high apparent speed and a relatively low value of ξ. We adopt the criterion $\xi/(\beta + \delta_{\text{var}}) < 0.15$ to select knots with low uncertainty. Choosing the highest apparent speed with a relatively low uncertainty ensures that the derived physical conditions are consistent with the most extreme, yet robust, behavior of the jet. The statistics of the chosen knots, one per source, would not have differed significantly across the sample had we instead chosen the knots with the highest established Doppler factor and lowest uncertainty. The typical knots are used to determine differences between the distributions of parameters for each subclass in Figures 8, 19, 20, and 21.

For each jet, we follow Jorstad et al. (2017) in calculating the opening semi-angle in two ways. Method A is based on the relation between the intrinsic and projected opening angles:

$$\theta_\circ^{\text{A}} = \theta_{\text{p}} \sin\langle\Theta_\circ\rangle \qquad (7)$$

(Jorstad et al. 2005). Here, θ_{p} is the projected opening semi-angle of the jet, and $\langle\Theta_\circ\rangle$ is the representative viewing angle of the jet. We define θ_{p} as twice the standard deviation of the knot position angles about a fixed value, regardless of whether the jet position angle is found to vary, as described in Section 3.2. We adopt the average uncertainties of $\langle\Theta_{\text{jet}}\rangle$, $\langle\sigma_\Theta\rangle$ as the uncertainty of θ_{p}.

Method B applies to jets with multiple reliable knots. We take the viewing angles of the fastest and slowest knot with low values of ξ (see above) to be the minimum and maximum viewing angles, $\Theta_\circ^{\text{min}}$ and $\Theta_\circ^{\text{max}}$. We then calculate the intrinsic opening semi-angle as

$$\theta_\circ^{\text{B}} = \frac{1}{2}(\Theta_\circ^{\text{max}} - \Theta_\circ^{\text{min}}). \qquad (8)$$

This definition would be appropriate if the difference in apparent speeds were due mainly to different viewing angles of
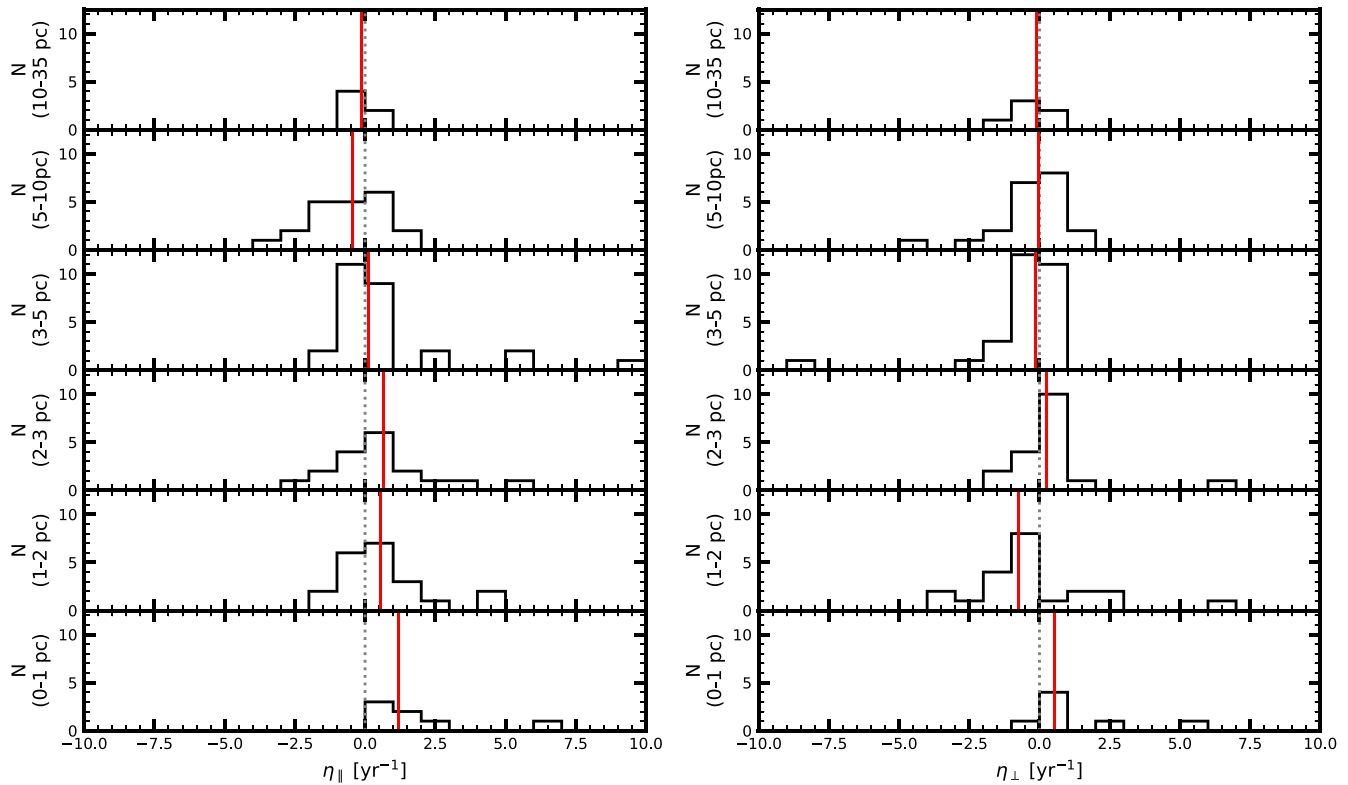
Figure 15. Histograms of relative knot accelerations (left) parallel and (right) perpendicular to the jet axis for all sources, separated by distance from the 43 GHz core. Red vertical lines in all panels indicate the median acceleration, while the gray dotted vertical lines indicate no acceleration.

Table 11
Median Values of Normalized Accelerations by Distance from the Core

Distance Bin (pc)	$\eta_{\parallel}$ (yr^{-1})	$\eta_{\perp}$ (yr^{-1})
0–1	1.20	0.53
1–2	0.55	−0.74
2–3	0.65	0.26
3–5	0.12	−0.15
5–10	−0.43	−0.05
10–35	−0.12	−0.12

the knots owing to the brightness centroids of the knots being located at different distances from the jet axis.

Table 13 gives the typical values of the physical parameters of knots in each source as follows: 1—name of the source; 2—luminosity distance, $D_{\rm Gpc}$, in gigaparsecs; 3—the knot selected as the representative high-speed knot; 4—Doppler factor of the representative knot, $\delta_{\rm var}$, and its uncertainty; 5—Lorentz factor of the representative knot, Γ, and its uncertainty; 6—viewing angle of the representative knot, $\Theta_{\rm o}$, and its uncertainty; 7—projected viewing opening semi-angle, $\theta_{\rm p}$, of the jet and its uncertainty; 8—opening semi-angle of the jet, $\theta_{\rm o}^{\rm A}$, derived using method A, and its uncertainty; 9—the knot selected as the representative low-speed knot; and 10—opening semi-angle of the jet, $\theta_{\rm o}^{\rm B}$, derived using method B, and its uncertainty.

Figure 23 presents a comparison between $\theta_{\rm o}^{\rm A}$ and $\theta_{\rm o}^{\rm B}$. For the majority of sources, there is good agreement (within the uncertainty) between the two opening semi-angles derived via the different methods. There are a small number of sources for which $\theta_{\rm o}^{\rm B} > \theta_{\rm o}^{\rm A}$, in contrast with the large number of sources

obeying this uncertainty found in Jorstad et al. (2017). This is likely due to the new definition of $\theta_{\rm o}^{\rm B}$, in which we take the opening semi-angle to be the difference between the fastest and slowest high-significance knot. One can explain this discrepancy for sources that have very small viewing angles, e.g., the BL Lac object 0235+164, where the knots have no preferential direction on the plane of the sky. Based on geometrical arguments, this cannot be the case for all sources in our sample.

Larger values of $\theta_{\rm o}^{\rm B}$ are to be expected if the jets of blazars are structured in a "spine-sheath" manner (e.g., Pelletier & Roland 1989; Sol et al. 1989; Celotti et al. 2001; Ghisellini et al. 2005; Tavecchio & Ghisellini 2008; D'Arcangelo et al. 2009; Xie et al. 2012; Mimica et al. 2015). Such a structure would consist of two flows: a faster, lower-density component streaming along the central axis (spine), and a slower, denser component along the edges of the jet. As the Doppler beaming would be stronger for the faster flow if viewed at a narrow angle, the spine would be expected to dominate the overall jet emission, while the sheath would be more intense at wider viewing angles (e.g., RGs; Bruni et al. 2021). Evidence for a spine-sheath structure in several blazar jets comes from linear polarization of VLBI images (e.g., Pushkarev et al. 2005; Asada et al. 2010; Gabuzda et al. 2014; Mertens et al. 2016), especially when including the space-based RadioAstron antenna in the array (Bruni et al. 2021).

It is possible that most knots seen in our images flow down the spine of a jet, (propelled by the rotational energy of the black hole; Blandford & Znajek 1977), while a relatively small number of knots form along the slower sheath (e.g., from a magnetically driven wind from the accretion disk; Blandford & Payne 1982). Several sources in our sample have been inferred to have a spine-sheath structure, such as 0316+413
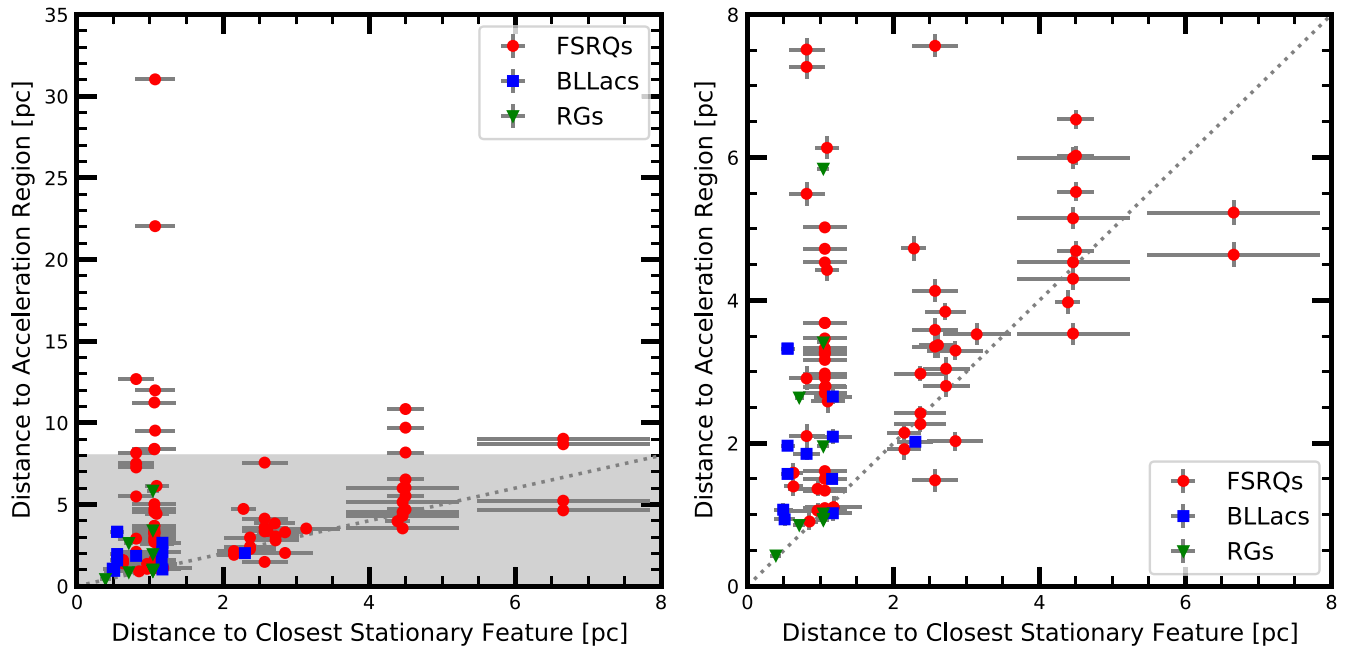
Figure 16. Left: distances from the 43 GHz core to the acceleration region and stationary feature closest to that acceleration region. The vertical segments of data correspond to sources that contain multiple knots with acceleration zones beyond the last stationary feature. The gray shaded region delineates the portion of the figure that is expanded for better viewing in the right panel. Error bars are shown in gray in both panels.
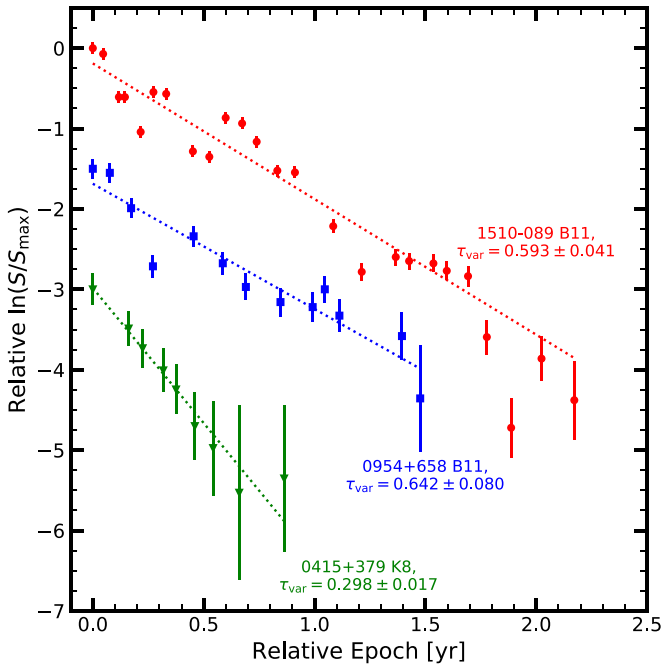

Figure 17. Light curves of moving knots B11 in the FSRQ 1510−089 (red circles), B11 in the BL Lac object 0954+658 (blue squares), and K8 in the RG 0415+379 (green triangles). The dotted lines represent the least-squares fits to the flux density decays of the knots. The data and fits for B11 and K8 have been shifted by −1.5 and −3.0 from their normalized values, respectively.

Figure 18. Timescale of variability of the size vs. that of the flux density for superluminal knots in our sample. "Reliable" estimates of τ_a (for which $\tau_a \geqslant 2\sigma_{\tau_a}$) are shown in black, while those that do not meet the reliability criterion are shown in red. The solid line marks the approximate relation for an optically thin shock with $\alpha \sim 0.7$ (Marscher & Gear 1985). Error bars are omitted for visual clarity.

(Giovannini et al. 2018), 1055+018 (Attridge et al. 1999; MacDonald et al. 2017), 1226+023 (MacDonald et al. 2017; Bruni et al. 2021), 1510−089 (MacDonald et al. 2015), 1652 +398 (Giroletti et al. 2004; Pushkarev et al. 2005), 0836+710, 1253−055, and 2230+114 (MacDonald et al. 2017). Neither 1652+398 nor 0316+413 have enough reliable superluminal knots for us to determine their jet structure (see Section 5.5 to obtain estimates of their physical parameters). The sources

1055+018 and 1226+023 both have $\theta_o^A > \theta_o^B$. The spine-sheath structure in 1055+018 was identified from the polarization of the emission rather than the total intensity that we have analyzed here. The inferred layered structure in 1226 +023 was based on images with extremely high spatial resolution at lower frequencies (1.6 and 4.8 GHz); it may be the case that we have not observed a slow knot in the sheath of this

Table 12
Physical Parameters of Jet Features

Source	Knot	τ_{var} (yr)	$\langle a \rangle$ (mas)	N_t	δ_{var}	Γ	$\Theta_{\circ}$ (deg)
(1)	(2)	(3)	(4)	(5)	(6)	(7)	(8)
0219+428	B1	0.535 ± 0.161	0.27 ± 0.02	6	21.6 ± 6.7	24.9 ± 5.6	2.6 ± 0.7
	B2	0.944 ± 0.300	0.40 ± 0.02	10	18.2 ± 5.9	13.8 ± 1.8	3.0 ± 1.3
	B3	0.639 ± 0.245	0.15 ± 0.02	6	10.2 ± 4.0	20.9 ± 5.4	4.8 ± 1.0
	B4	1.511 ± 0.330	0.43 ± 0.03	6	12.3 ± 2.8	22.8 ± 3.5	4.1 ± 0.5
	B5	1.240 ± 0.212	0.28 ± 0.02	11	9.9 ± 1.8	19.8 ± 3.0	5.0 ± 0.5
0235+164	B1	0.324 ± 0.068	0.26 ± 0.02	6	63.3 ± 13.9	37.2 ± 5.8	0.7 ± 0.2
	B2	0.207 ± 0.023	0.20 ± 0.01	9	76.7 ± 9.4	39.4 ± 4.5	0.2 ± 0.1
	B3	1.243 ± 0.119	0.15 ± 0.01	28	9.3 ± 0.9	5.1 ± 0.4	3.2 ± 0.7
	B4	0.717 ± 0.102	0.15 ± 0.01	13	16.4 ± 2.5	9.1 ± 1.1	2.1 ± 0.6
	B5	0.493 ± 0.068	0.23 ± 0.01	13	37.9 ± 5.4	20.0 ± 2.5	0.7 ± 0.2
	B6	0.361 ± 0.044	0.28 ± 0.01	13	62.5 ± 8.1	31.6 ± 4.0	0.2 ± 0.1

(This table is available in its entirety in machine-readable form.)

source. Conclusive evidence for spine-sheath structure in the jets of our sample can be found through an analysis of stacked images and maps of polarized intensity (as has been done for several sources in MacDonald et al. 2015, 2017), but is beyond the scope of this work.

5.4. Comparison with Other Physical Parameter Estimations

Several methods exist that use a variety of data at different frequencies to estimate the Doppler factor in blazar jets and subsequently infer the physical parameters of the jets themselves (e.g., Ghisellini et al. 1993; Lähteenmäki & Valtaoja 1999; Jorstad et al. 2005; Fan et al. 2013, 2014; Chen 2018; Lister et al. 2019; Zhang et al. 2020). Reviews of the methods and their results can be found in, e.g., Liodakis & Pavlidou (2015) and Liodakis et al. (2017a, 2017b). Here we compare a few of these results with those inferred from our piecewise kinematic fitting.

In order to quantify whether the distributions of the physical parameters from our work differ from those of others, we employ the Wilcoxon rank-sum test[16] (WRS, or, alternatively, the Mann–Whitney U-test; Mann & Whitney 1947). Since we wish to test whether estimation of the physical parameters depends on the method employed, we assume that the parameters are drawn from the same distribution, and thus the WRS test can indicate whether there is a systematic bias in the methodology. The WRS test operates under the null hypothesis that two distributions are drawn from the same sample, and for this test, smaller p-values indicate a larger likelihood that the distributions are different. We consider two data sets to be different if their WRS p-value < 0.005 ($\sim 3\sigma$ confidence level). Figure 24 shows a comparison between the results of this work and those of Jorstad et al. (2017) and Liodakis et al. (2018), to accompany the indicated p-values.

The most direct comparison can be made with Jorstad et al. (2017), as the current work shares data, methodology, and underlying physical assumptions. In this comparison, we ignore the three sources with no reliable knots for deriving values of physical parameters. The majority of our estimated

values of (δ_{var}, Γ, $\Theta_{\circ}$, θ_p, $\theta_{\circ}^A$, and $\theta_{\circ}^B$) agree within the sum of the two estimated 1σ uncertainties. Table 14 gives p-values between the "representative" physical parameters given in Table 13 and the average values from Jorstad et al. (2017). For most parameters, there is no statistically significant difference in the distributions. However, there is a slight tendency for the representative value of Γ defined in this work to be higher than that of Jorstad et al. (2017). This is likely due to how we define a "representative" knot as the fastest one with a relatively small ξ value, rather than averaging all knots together as was done in Jorstad et al. (2017). Similarly, the reported $\theta_{\circ}^A$ values in this work are slightly larger than those inferred previously, but this is probably due to $\langle \Theta_{\circ} \rangle$ and θ_p now being defined from >10 yr of observation, which samples a wider range of knot behaviors.

Another useful comparison can be made with the work of Liodakis et al. (2018). These authors modeled the 15 GHz light curves of 1029 blazars and blazar-like AGNs, as observed with the Owen's Valley Radio Observatory (OVRO; Richards et al. 2011), with a series of exponential rise and decay profiles (flares) superposed on a stochastic background. For each flare, a variability brightness temperature was calculated. Since each source can have numerous flares within the light curve, distributions of variability brightness temperatures can be made for each source. Comparison with an expected equilibrium brightness temperature then yields distributions of Doppler factors, δ_{var}. The authors then used the maximum apparent speeds of radio knots at 15 GHz from the MOJAVE program (Lister et al. 2016) to calculate Γ and $\Theta_{\circ}$. Agreement between the two methods would provide important constraints for the Doppler factors and equipartition states in the jets.

All of the sources in the VLBA-BU-BLAZAR program have been observed by OVRO and are included in Liodakis et al. (2018), except for the FSRQ 1622−297, which is below the decl. limit for the OVRO monitoring program. Two sources, the BL Lac objects 0735+178 and 0954+658, did not have reliable redshift estimates at the time of Liodakis et al. (2018). These have since been refined in NASA/IPAC Extragalactic Database to $z = 0.424$ and 0.368, respectively. Using the same formalism as Liodakis et al. (2018), we have updated the Lorentz factors and viewing angles (Equation (6)) to be $\Gamma = 8.4 \pm 1.6$, $\Theta_{\circ} = 3.3 \pm 1.6$ for 0735+178 and $\Gamma = 15.4 \pm 1.2$, $\Theta_{\circ} = 3.5 \pm 1.1$ for 0954+658.

Comparing the physical parameters δ_{var}, Γ, and $\Theta_{\circ}$ between our current work and Liodakis et al. (2018), we again see good

---

[16] The K-S test, used elsewhere in this work, is sensitive to differences in the general shape of two distributions (i.e., dispersion, skewness, etc.), whereas the WRS test is sensitive to differences in the location (e.g., the median) of the two samples.
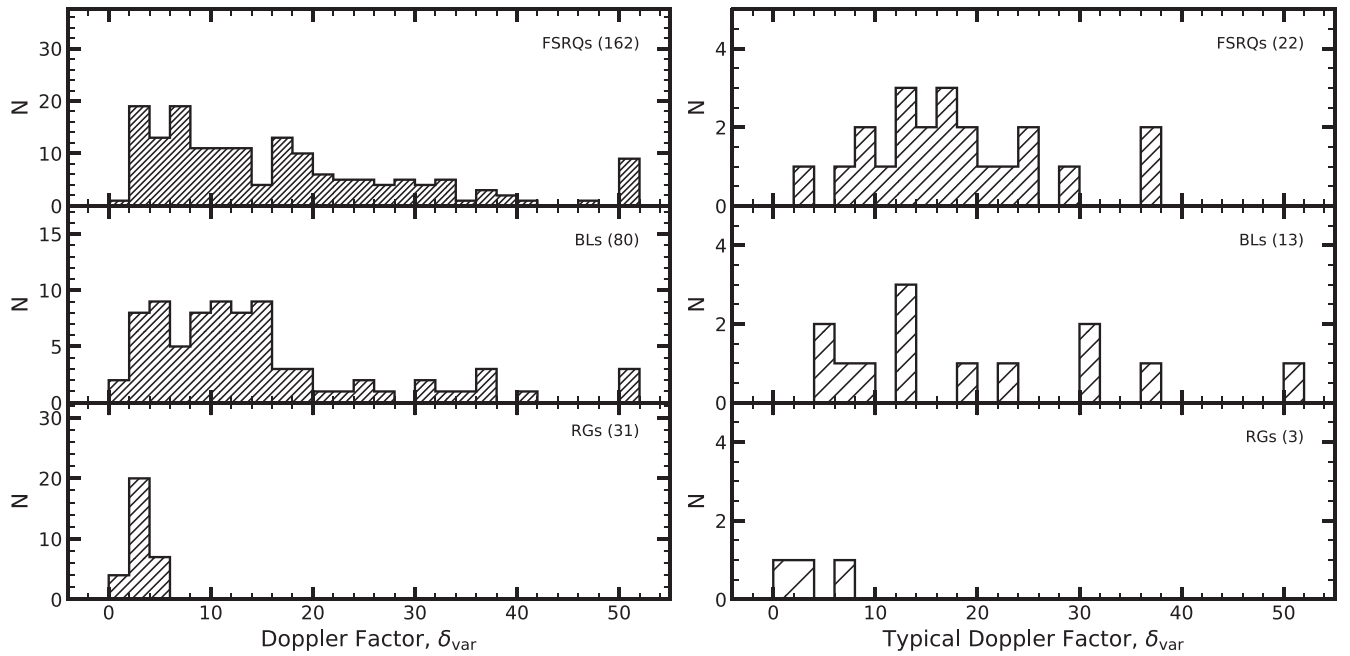
Figure 19. Distributions of all calculated (left) and typical (defined in Section 5.3, right) Doppler factors of variability, δ_{var}, derived for reliable moving knots in FSRQs (top), BL Lac objects (middle), and RGs (bottom). The typical δ_{var} for the BL Lac object 1101+384 is shown in the last bin to condense the axis.

agreement between the distributions. The majority of estimates of the physical parameters of each jet lie within the sum of the uncertainties between the two samples. WRS p-values between the two data sets are given in Table 14. No comparison meets our significance threshold, indicating that the distributions are not significantly different. Discrepancies in the values of parameters calculated by Liodakis et al. (2018) and this work are likely due to the difference in observing frequencies, resulting in different parts of the jet being probed.

Finally, we compare our results with modeling of the relation between Θ_{o} and Γ. Given that Doppler beaming increases with smaller viewing angles while geometrical likelihood increases with larger angle, the most probable viewing angle is somewhat smaller than that which maximizes the apparent velocity, $\Theta_{max} = \arcsin 1/\Gamma \approx 1/\Gamma$ for $\Gamma \gg 1$ (Marscher 1990). Vermeulen & Cohen (1994) found that the most likely angle is $\sim 0.5\Theta_{max}$. Meanwhile, Lister & Marscher (1997) used Monte Carlo simulations to determine statistical properties of beamed sources in a flux-limited sample, including the viewing angle at which a jet will appear in a flux-limited sample given its Lorentz factor and intrinsic luminosity. They found that the peak of the simulated distribution is $\Theta_{o} \sim 0.4\Theta_{max}$, with a considerable number of sources having $\Theta_{o} > \Theta_{max}$.

To see if these relations hold observationally, we plot the viewing angle of all reliable knots in our sample against Γ^{-1} in Figure 25. The data appear to fall into several distinct groups. To guide the reader's eye, we have added three lines indicating values for which $\Theta_{o} = 0.5$, 1, and 2 times Θ_{max}. The vast majority of knots fall between the $0.5\times$ and $2\times$ lines and with $\Theta_{max} \lesssim 0.15$ rad. Two extended populations appear, roughly following the $\Theta_{o} \sim \Theta_{max}$ and $2\Theta_{max}$ lines. Almost all of the RG knots appear along these extended populations.

To get a statistical sense of which relation most accurately describes the observations, we have followed Lister & Marscher (1997) by calculating the percent difference between Θ_{o} and Θ_{max}, which we plot as a histogram for each source type in Figure 26. There are nine FSRQ knots for which the

difference is $>300\%$, usually in cases of very high values of Γ. As these represent a small fraction ($\sim 5\%$) of the knots, we have omitted them to reduce the size of the figure. For FSRQs and BL Lac objects, we recover the simulated distribution of Lister & Marscher (1997). In these two distributions, the peak appears near -50% difference, but there is a long tail showing that many knots can have $\Theta_{o} > \Theta_{max}$. The two distributions are similar statistically, with a K-S test statistic of $\mathcal{D} = 0.72$ and $p = 0.073$. However, we do not see a similar distribution for the RGs ($\mathcal{D} = 0.460$, $p = 1.5 \times 10^{-5}$ for the FSRQ versus RG and $\mathcal{D} = 0.513$, $p = 6.3 \times 10^{-6}$ for the BL Lac object versus RG distributions). There is a wide spread of the percent difference for these sources, and no obvious distribution peak due to the small number of observed knots. The wide spread is an indication that the expected Θ_{max} relation with Γ is not a good indicator of the true viewing angle for RGs (Lister & Marscher 1997).

5.5. Averages of Physical Parameters of AGN Subclasses

We use the same formalism as Jorstad et al. (2017) to calculate the weighted averages of the physical parameters for each subclass in our sample. Two values of the average opening semi-angle values are obtained for the two different methods of estimating θ_{o}, $\overline{\theta_{o}}^{A}$ and $\overline{\theta_{o}}^{B}$. We calculate the uncertainty in the average quantities as the weighted standard deviation of the parameters of the sources in the subclass about these means, where the weights are the inverse of the variance of the parameter for each source. Table 15 gives the result of the averaging as follows: 1—Name of the AGN subclass; 2—number of sources in the subclass, N_s, used to calculate the averages; 3—Doppler factor, $\overline{\delta}$, and its weighted standard deviation from the included knots; 4—bulk Lorentz factor, $\overline{\Gamma}$, and its weighted standard deviation; 5—viewing angle, $\overline{\Theta_{o}}$, and its weighted standard deviation; 6—opening semi-angle of the jet according to method A, $\overline{\theta_{o}}^{A}$, and its weighted standard
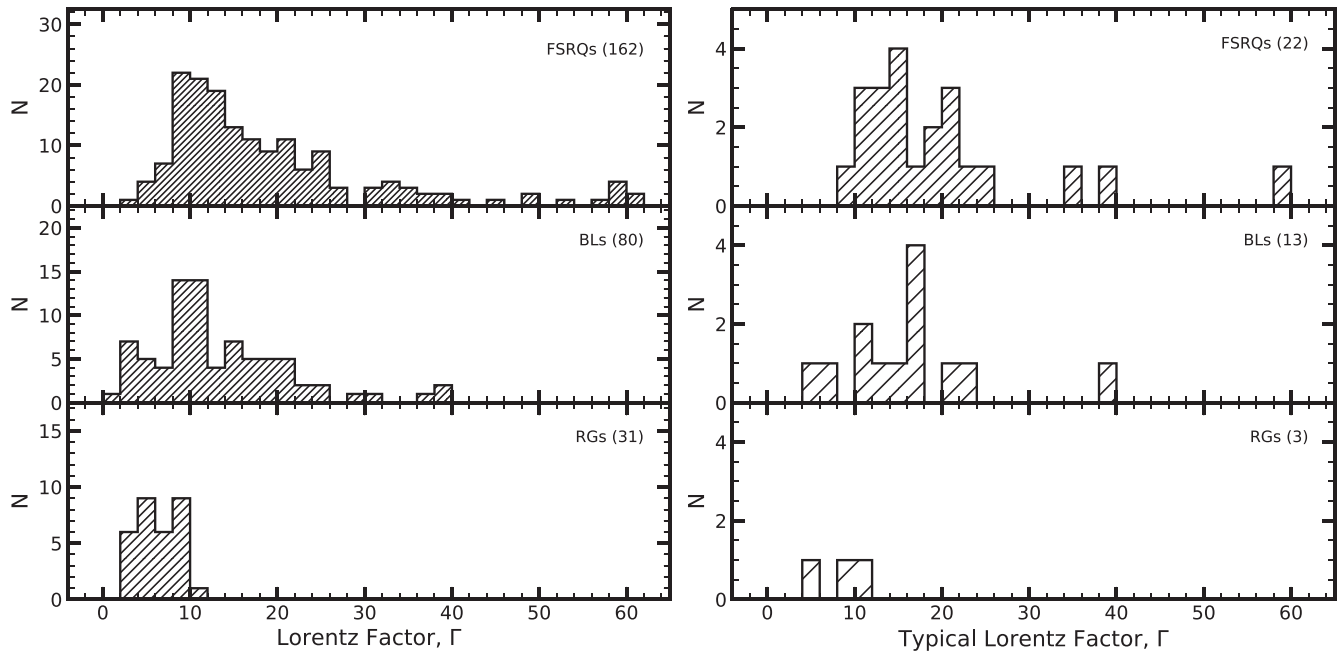
Figure 20. Distributions of all calculated (left) and typical (defined in Section 5.3, right) Lorentz factors, Γ, in FSRQs (top), BL Lac objects (middle), and RGs (bottom), derived from the apparent speeds and variability Doppler factors of reliable knots.

deviation; and 7—opening semi-angle of the jet according to method B, $\overline{\theta_\circ}^{\mathrm{B}}$, and its weighted standard deviation.

While the physical parameters of FSRQs and BL Lac objects overlap when the standard deviations are included, the expected trend of larger Doppler and Lorentz factors in FSRQs relative to BL Lac objects is observed in the current data (Jorstad et al. 2005). Higher values of δ in FSRQs are supported by the higher brightness temperatures of moving components. The relative similarity of the viewing and opening semi-angles between the two subclasses (compared to previous results; e.g., Pushkarev et al. 2009; Jorstad et al. 2017) can be explained by our choice of the fastest "typical" knot to represent particular sources. In a spine-sheath jet structure, the fastest knots all come from the spine, resulting in an opening semi-angle that would be smaller than if all knots were considered together (as would be expected in BL Lac objects). The physical parameters of RGs are also consistent with the predictions of the unified scheme of AGNs (Urry & Padovani 1995), with comparable Lorentz factors, smaller Doppler factors, and much larger viewing angles compared to FSRQs and BL Lac objects. However, as was pointed out in Jorstad et al. (2017), these RGs are the brightest γ-ray emitters of their subclass, and may not be representative of the subclass as a whole.

Three sources in our sample do not have superluminal knots meeting our reliability criteria described at the beginning of Section 5: the RG 0316+413 and the BL Lac objects 1652+398 and 1959+650. Thus, we cannot calculate their physical parameters using their knot motions. Instead, we make a rough estimate for the physical parameters of these sources based on two assumptions: (1) the intrinsic opening semi-angle of the jet is equal to $\overline{\theta_\circ}^{\mathrm{A}}$, the average of the subclass to which the source belongs, and (2) $\Gamma\theta_\circ \sim 0.2$ is universal for bright γ-ray AGNs (Clausen-Brown et al. 2013; Jorstad et al. 2017). The low apparent speeds of the knots in the BL Lac object 1101+384 indicate that we are looking at the sheath of the jet, so we also use the same formalism to estimate the parameters of this

source. The estimated parameters for these four sources are given in Table 13. The above assumptions result in viewing angles $\sim 2\times$ smaller than the subclass average for these sources. As we have only observed 1959+650 at six epochs, it is possible that the jet does indeed have physical parameters as estimated above, but more monitoring is necessary. However, the fact that only slow proper motions have been observed in 0316+413, 1101+384, and 1652+398 despite intensive monitoring campaigns (e.g., this work; Blasi et al. 2013; Lister et al. 2016) creates a "Doppler crisis" with their high-energy properties, which require high Doppler factors (and subsequently high proper motions). The decelerations observed in Figure 15 (5–10 pc from the core for parallel acceleration, and 1–2 pc from the core for perpendicular acceleration) might be able to explain the discrepancy, as high Doppler factors would only be seen closer to the central engine, beyond the opacity limit of 43 GHz observations. It is also possible that a mildly relativistic flow, corresponding to a "sheath" around the faster central spine, would obscure the faster spine, as seems to be the case in 0316+413 (Nagai et al. 2014).

6. Discussion

6.1. Brightness Temperatures and Doppler Factors

The brightness temperature distributions presented in Section 3.1 are similar to those expected for unbeamed, incoherent synchrotron radiation produced by relativistic electrons that are in equipartition with the magnetic field $T_{\mathrm{b,eq}} \sim 5 \times 10^{10}$ K (Readhead 1994). The higher values of $T_{\mathrm{b,obs}}^{\mathrm{s}}$ found in FSRQs and BL Lac objects can be partially explained by Doppler boosting: $T_{\mathrm{b,obs}} \propto \delta T_{\mathrm{b,int}}$; the Doppler factor has been inferred to be as high as $\delta \sim 60$ in blazars (e.g., Liodakis et al. 2018). During high activity states (such as outbursts) of blazars, it is possible that equipartition is violated such that the energy density of radiating particles is greater than that of the magnetic field in the VLBI core (e.g., Homan et al.
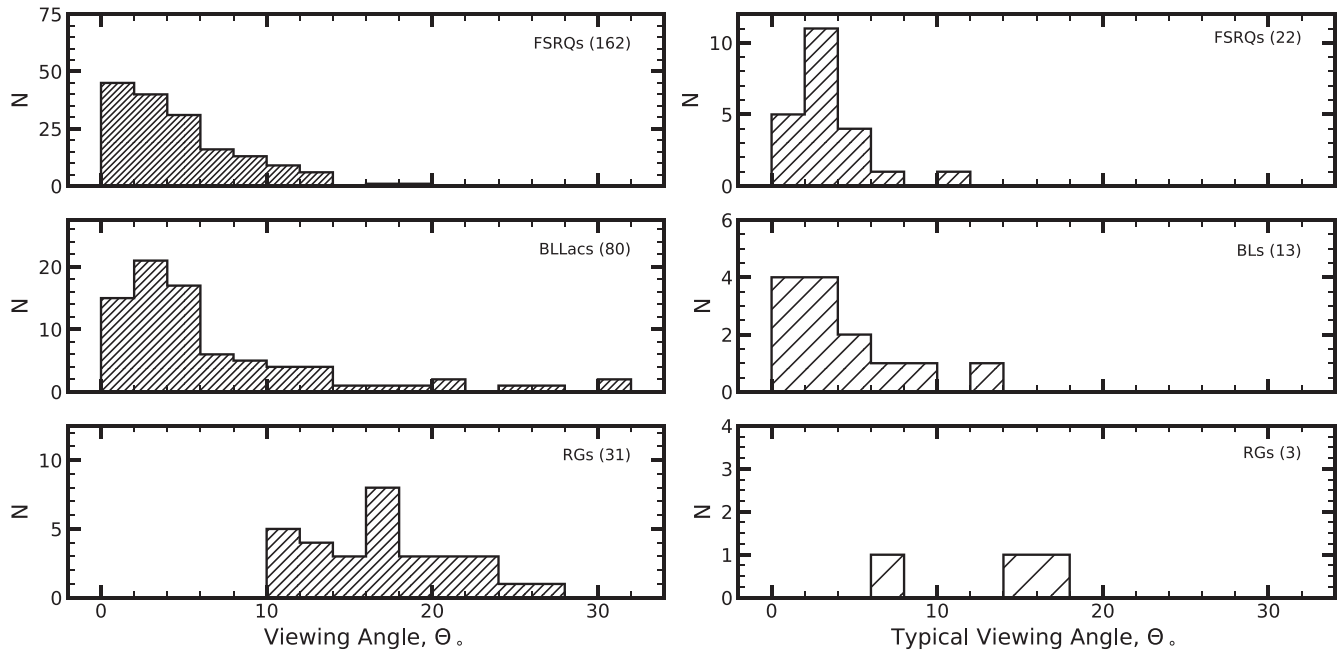
Figure 21. Distributions of all calculated (left) and typical (defined in Section 5.3, right) viewing angles in FSRQs (top), BL Lac objects (middle), and RGs (bottom), derived from the apparent speeds and variability Doppler factors of reliable knots. Note the different scales in each panel.
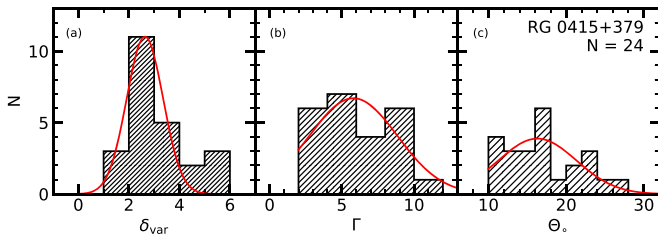

Figure 22. Distributions of physical parameters (a) $\delta_{\rm var}$, (b) Γ, and (c) $\Theta_{\circ}$ of reliable knots in the RG 0415+379. Red curves represent best-fit Gaussian distributions to the data. See the text for details.

2006; Kovalev et al. 2016). Such nonequipartition states could lead to the extremely high ($T_{\rm b,obs}^{s} \gtrsim 10^{13}$ K) brightness temperatures found in some sources.

Figure 27 compares the typical Doppler factor of variability, $\delta_{\rm var}$, for each source with the maximum brightness temperature of the core component $A0$ in the host-galaxy frame, $T_{\rm b,obs}^{s} = T_{\rm b,obs}(1 + z)$. In the figure, both the maximum resolved brightness temperature (closed symbols) and lower limit to the maximum brightness temperature (open symbols, based on the observed size of the component; see Section 2.1) are plotted. We have connected the resolved brightness temperatures and lower limits in each source with a dotted line to aid the reader. Sources with physical parameters estimated via the method presented in Section 5.5 are omitted. In general, we see that sources with higher maximum brightness temperatures tend to have higher Doppler factors. Also, the maximum brightness temperatures of FSRQs tend to be higher than those of BL Lac objects (as expected from the distributions in Figure 4). Taking the three subclasses together, the Doppler factors and maximum brightness temperatures of the cores have a Pearson's r correlation coefficient of 0.367 for the resolved components. There is more scatter in the data when considering only the lower limits, which have a correlation coefficient of 0.281 with the maximum brightness temperatures of the cores. The maximum core brightness

temperatures range up to $\sim 10^{13}$ K. These could be indicative of nonequipartition states in the 43 GHz cores of blazars. We see a connection between the γ-ray state of blazars and their 43 GHz properties (see Section 6.3 below), so these nonequipartition values are expected. However, the moving components all have $T_{\rm b,obs}^{s} < 5 \times 10^{12}$ K, which can be explained by Doppler boosting with our observed Doppler factor values, $\delta_{\rm var} \lesssim 60$.

6.2. Flux Variability

As discussed in Section 5.1, the rise and decay of flux in millimeter-wave light curves of blazars can be roughly modeled by exponential profiles (e.g., Terasranta & Valtaoja 1994; Lister 2001; Savolainen et al. 2002). We are thus able to estimate a timescale of variability, $\tau_{\rm var}$, from the flux decay rate, k, as $\tau_{\rm var} = |1/k|$ yr. We show in Figure 18 that these decay rates are often primarily due to radiative losses, modulated by light-travel delays, as opposed to adiabatic expansion. As the emission from blazar jets at 43 GHz is dominated by synchrotron radiation, standard synchrotron emission formulae (e.g., Pacholczyk 1970; Longair 2011) yield an expected relation between the emitted flux density and distance down the jet R, $S_{43} \propto R^{-a}$. Using the proper motion of a knot, $\mu = dR/dt$, we can estimate the age of a knot as $T_{\rm age} = \langle R \rangle / \mu$ in the observer's frame. Homan et al. (2002) adopted a decay rate of a knot that is inversely proportional to $T_{\rm age}$:

$$ k = \frac{(dS_{43}/dt)}{S_{43}} = -a \times \frac{(dR/dt)}{R} = -a/T_{\rm age}. \qquad (9) $$

We have already calculated the normalized decay rates of the majority of knots in our sample as $(dS_{43}/dt)/S$ (see Section 5.1). We revise the relation in Equation (9) to a more general form: $k = -aT_{\rm age}^{-b}$, where a and b are constants. We transform the component ages to the source (i.e., host-galaxy) frame (s) through $T_{\rm age}^{s} = T_{\rm age}/(1 + z)$. Figure 28 shows the decay rate k^{s} of all knots in our reliable sample versus the age

Table 13
Typical Physical Parameters of Jets

Source	D_{Gpc} (Gpc)	Fast Knot	δ_{var}	Γ	$\Theta_\circ$ (deg)	θ_p (deg)	$\theta_\circ^A$ (deg)	Slow Knot	$\theta_\circ^B$ (deg)
(1)	(2)	(3)	(4)	(5)	(6)	(7)	(8)	(9)	(10)
0219+428	2.458	B4	12.3 ± 2.8	22.8 ± 3.5	4.1 ± 0.5	18.0 ± 5.5	1.3 ± 0.4	B5	0.4 ± 0.4
0235+164	6.121	B5	37.9 ± 5.4	20.0 ± 2.5	0.7 ± 0.2	13.2 ± 6.8	0.2 ± 0.1	B3	1.2 ± 0.3
0316+413[a]	0.077	…	∼6.9	∼4.8	∼7.2	19.2 ± 0.4	∼2.4	…	…
0336−019	5.422	B5	9.0 ± 4.1	9.6 ± 0.8	6.3 ± 2.8	12.8 ± 4.6	1.4 ± 0.8	B3	0.8 ± 1.6
0415+379	0.215	K22	2.8 ± 0.2	8.5 ± 0.5	15.2 ± 0.4	9.8 ± 2.2	2.6 ± 0.6	K5	11.5 ± 1.3
0420−014	5.928	B3	25.2 ± 3.4	21.2 ± 0.6	2.2 ± 0.4	35.2 ± 3.7	1.4 ± 0.3	B5	2.2 ± 0.6
0430+052	0.145	C15	1.9 ± 0.4	10.0 ± 1.8	17.9 ± 0.8	6.4 ± 2.9	2.0 ± 0.9	C4	4.0 ± 0.6
0528+134	16.109	C2	17.3 ± 2.4	11.7 ± 0.8	2.9 ± 0.6	26.6 ± 6.0	1.4 ± 0.4	B3	0.4 ± 0.4
0716+714	1.553	B13	23.3 ± 3.6	17.1 ± 1.1	2.3 ± 0.4	38.6 ± 3.9	1.5 ± 0.4	B4	0.7 ± 0.7
0735+178	2.327	B3	12.2 ± 3.3	7.2 ± 1.4	3.4 ± 1.6	27.6 ± 10.7	1.6 ± 1.0	B4	1.1 ± 0.8
0827+243	6.129	B6	10.8 ± 1.4	38.0 ± 3.9	3.7 ± 0.2	16.2 ± 5.8	1.0 ± 0.4	B7	0.1 ± 0.3
0829+046	0.840	B5	19.6 ± 6.0	13.6 ± 1.9	2.6 ± 1.2	21.2 ± 5.7	1.0 ± 0.5	B4	4.4 ± 3.0
0836+710	17.185	B3	13.5 ± 0.7	17.8 ± 0.5	4.1 ± 0.2	18.0 ± 3.3	1.3 ± 0.2	B6	0.1 ± 0.3
0851+202	1.589	B12	6.4 ± 1.9	11.8 ± 1.7	7.9 ± 1.3	24.6 ± 1.2	3.4 ± 0.6	B6	2.5 ± 1.5
0954+658	1.969	B14	9.8 ± 1.6	38.8 ± 4.7	3.9 ± 0.2	19.4 ± 2.1	1.3 ± 0.2	B19	5.1 ± 0.8
1055+018	5.722	B3	16.9 ± 3.9	12.8 ± 1.0	3.2 ± 1.0	36.8 ± 6.5	2.1 ± 0.7	B1	1.4 ± 1.1
1101+384[a]	0.131	…	∼65.5	∼16.4	∼1.4	27.8 ± 14.2	∼0.7	…	…
1127−145	8.142	C1	13.6 ± 2.5	12.1 ± 0.5	4.2 ± 0.9	20.8 ± 4.3	1.5 ± 0.4	B2	3.8 ± 0.6
1156+295	4.446	B2	15.0 ± 2.8	10.1 ± 1.0	3.4 ± 1.0	22.2 ± 3.8	1.3 ± 0.4	B3	0.2 ± 0.5
1219+285	0.470	B1	4.5 ± 1.1	5.3 ± 0.3	12.6 ± 2.6	16.0 ± 10.6	3.5 ± 2.4	B3	4.6 ± 4.1
1222+216	2.379	B5	7.0 ± 0.6	34.7 ± 2.7	4.9 ± 0.1	42.8 ± 1.9	3.7 ± 0.2	B3	1.3 ± 0.1
1226+023	0.755	B2	3.2 ± 0.3	15.7 ± 1.1	10.9 ± 0.2	10.8 ± 0.7	2.0 ± 0.1	B16	1.2 ± 0.3
1253−055	3.080	C35	8.2 ± 0.9	59.6 ± 5.6	3.5 ± 0.1	36.8 ± 1.0	2.3 ± 0.1	C31	1.0 ± 0.1
1308+326	6.591	B3	18.5 ± 2.9	14.6 ± 0.7	3.0 ± 0.6	25.8 ± 4.7	1.3 ± 0.4	B1	7.9 ± 1.5
1406−076	10.854	B4	18.4 ± 2.9	18.0 ± 0.7	3.1 ± 0.5	29.0 ± 7.2	1.6 ± 0.5	B2	3.1 ± 0.7
1510−089	1.919	B1	37.0 ± 2.7	25.6 ± 1.1	1.4 ± 0.2	16.0 ± 2.8	0.4 ± 0.1	B10	1.6 ± 0.6
1611+343[b]	10.009	B1	25.7 ± 3.9	14.0 ± 1.8	1.2 ± 0.4	26.2 ± 3.3	0.5 ± 0.2	…	…
1622−297	5.133	B5	21.9 ± 2.8	18.0 ± 0.6	2.6 ± 0.4	23.4 ± 3.3	1.0 ± 0.2	B4	0.7 ± 0.6
1633+382	13.775	B3	23.8 ± 3.9	13.6 ± 1.8	1.6 ± 0.5	18.2 ± 6.1	0.5 ± 0.2	B5	0.4 ± 0.3
1641+399	3.480	B4	13.2 ± 1.7	20.8 ± 1.0	4.1 ± 0.3	17.2 ± 2.6	1.2 ± 0.2	B1	8.5 ± 0.3
1652+398[a]	0.149	…	∼31.5	∼16.4	∼0.7	53.8 ± 11.8	∼0.7	…	…
1730-130	5.817	B6	14.8 ± 3.7	21.3 ± 1.9	3.7 ± 0.7	27.2 ± 1.4	1.8 ± 0.3	B3	2.0 ± 0.5
1749+096	1.685	B7	12.2 ± 1.9	10.8 ± 0.7	4.6 ± 0.8	31.0 ± 2.3	2.5 ± 0.5	B5	1.9 ± 0.5
1959+650[a]	0.209	…	∼30.3	∼16.4	∼1.0	38.2 ± 12.9	∼0.7	…	…
2200+420	0.311	B8	4.3 ± 1.2	14.6 ± 3.0	9.5 ± 0.8	9.0 ± 1.8	1.5 ± 0.3	B6	0.1 ± 2.0
2223-052	10.053	B4	16.3 ± 2.3	10.3 ± 1.0	2.3 ± 0.7	29.4 ± 3.2	1.5 ± 0.4	B2	0.7 ± 1.1
2230+114	6.911	B4	37.5 ± 6.7	23.6 ± 2.6	1.2 ± 0.4	20.2 ± 3.6	0.4 ± 0.1	B2	0.8 ± 0.2
2251+158	5.477	B10	28.8 ± 2.2	15.7 ± 1.0	1.1 ± 0.2	24.4 ± 1.6	0.5 ± 0.1	B9	0.1 ± 0.2

Notes.
[a] Estimates of the parameters are discussed in Section 5.5.
[b] The source contains only one "reliable" knot.

of the feature, T_{age}, separated by blazar subtype. We have fit the generalized equation for the decay rate to each subclass, and show the results by the red dashed, blue dotted–dashed, and green dotted curves for FSRQs, BL Lac objects, and RGs, respectively, in the figure.

Correcting the age for redshift results in different phenomenological fits for all three subtypes. The BL Lac objects have a best-fit exponent b near unity, while FSRQs have $b \sim 0.75$. The exponent for RGs is a factor of 1.6 smaller than for BL Lac objects, with $b = 0.65$. The results for BL Lac objects and FSRQS are similar to those found in Homan et al. (2002), despite the authors' assumption that the flux decay of knots is linear rather than exponential.

We provide the distributions of knot ages for each subclass in the left panel of Figure 29. All three distributions are qualitatively similar, with a substantial peak in the distribution for components that live for ∼1–2 yr. There are several knots in

FSRQs that are long-lived, with $T_{\text{age}}^s > 5$ yr, while no such knots exist in BL Lac objects and RGs. Of the three subtypes, the BL Lac object distribution has the largest fraction of short-lived knots, with 70% of knots having $T_{\text{age}}^s < 1$ yr. A K-S test between the distributions confirms the similarities, with $\mathcal{D} = 0.242$, $p = 0.003$ for FSRQs versus BL Lac objects, $\mathcal{D} = 0.177$, $p = 0.345$ for FSRQs versus RGs, and $\mathcal{D} = 0.130$, $p = 0.786$ for BL Lac objects versus RGs.

If the decay of the flux density of a knot is controlled by the light-crossing time, intrinsically smaller knots should have shorter decay times in the plasma frame. Since the angular sizes of knots are similar for all of the sources (see Table 2), knots in objects with lower redshifts—all of the RGs—should have smaller sizes. Given the lower mean redshift values of the RGs versus the BL Lac objects and FSRQs, this effect must be canceled by the higher Doppler factors found for the BL Lac objects and FSRQs in order to explain the similar 1–2 yr ages of the peaks of the distributions seen in Figure 29. To verify
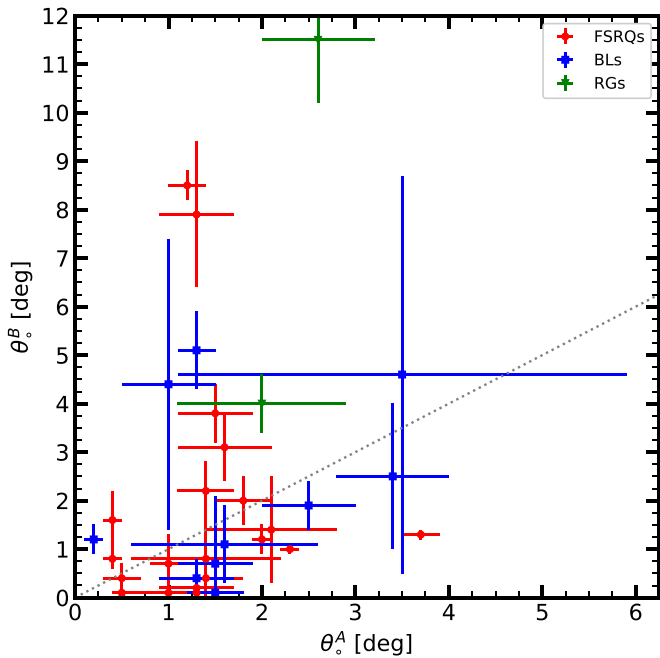
Figure 23. Comparison between opening semi-angles, $\theta_\circ$ of sample sources, derived using methods A and B (see the text for details). The gray dotted line indicates $\theta_\circ^A = \theta_\circ^B$.

this, we calculate the age of components in the plasma frame of each jet by multiplying the redshift-corrected age by the Doppler factor of variability, so that $T_{\rm age}^{\rm plasma} = \delta_{\rm var} T_{\rm age}/(1 + z)$. The distributions for each source type are shown in Figure 29 (right panel). The FSRQ and BL Lac object distributions differ at the $\sim 3\sigma$ level, with $\mathcal{D} = 0.244$ and $p = 0.003$. However, both distributions peak at a knot age ~ 10 yr. A large number of BL Lac object knots have shorter ages, while there are more knots in FSRQs with greater ages. Scaling by $\delta_{\rm var}$ separates the RG distribution from the FSRQ and BL Lac objects ($\mathcal{D} = 0.813$, $p = 3.2 \times 10^{-16}$ and $\mathcal{D} = 0.718$, $p = 4.9 \times 10^{-11}$, respectively). The typical intrinsic age of an RG knot is ~ 1 yr, a factor of ten lower than for FSRQs and BL Lac objects, roughly in accord with the ratios of physical sizes of their knots.

It is important to point out the effect that our roughly monthly observation cadence might have on the observed lifetimes of knots. Very bright components in the jets of blazars are easy to identify in the radio maps and fit with Gaussian profiles (as in Section 2), thus would need to have extremely fast decays (<1 month) to not be seen at other epochs. Given the paucity of short-decay knots seen in the distributions in Figure 29, this scenario is unlikely. However, faint components are difficult to distinguish from noise, especially if such knots travel down the jet quickly with short decay times (e.g., if their decay were <0.25 yr, as we require at least four observations of a knot for it to be properly identified). Such knots would be missed in the above analysis. Fast, faint components have been seen in some sources (e.g., the BL Lac object 0219+428 (3C 66A); Jorstad et al. 2005), but to detect them requires denser temporal sampling.

6.3. Gamma-Ray Connection

It is well established that there exists a connection between the γ-ray state of blazars and their parsec-scale jet behaviors. Nieppola et al. (2011) have shown that there is a statistically significant correlation between the γ-ray and 37 GHz radio light curves. The brightest γ-ray flares tend to coincide with with the early stages of a millimeter-wave outburst (León-Tavares et al. 2011). Such trends are not universal: for example, at 15 GHz a significant correlation was only found in four of 41 analyzed blazars (Max-Moerbeck et al. 2014). However, the F-GAMMA program has found that the radio variations of 54 γ-ray bright blazars lag the γ-ray variations, with delays systematically decreasing as the observed frequency changes from centimeter to millimeter/submillimeter (Fuhrmann et al. 2014). With regard to knots traveling down the parsec-scale jet, studies of individual sources have revealed a wide diversity in the behavior of blazars. The majority of γ-ray outbursts appear to be connected with the propagation of a knot down the jet (e.g., Jorstad et al. 2001a, 2013, 2017; Marscher et al. 2010; Agudo et al. 2011a; Morozova et al. 2014). In several of these cases, the flux profile of the γ-ray outburst can be connected with the passage of superluminal knots through the core or quasi-stationary features (e.g., Agudo et al. 2011a; Weaver et al. 2019; Liodakis et al. 2020). However, these features are usually located parsecs from the central black hole, at odds with the small sizes required by causality arguments from the short timescales of high-energy variability (Aharonian et al. 2007; Tavecchio et al. 2010; Nalewajko et al. 2014). Another problem is the origin of high-energy outbursts known as "orphan" flares (e.g., Krawczynski et al. 2004; Marscher et al. 2010; MacDonald et al. 2015; Sobacchi et al. 2021; Yang et al. 2021). During such flares, the γ-ray flux may increase by a factor ~ 100, and yet little variability is seen at longer wavelengths, with no interaction between moving and stationary features observed in VLBA images.

While a full analysis of the relationship between the parsec-scale jet kinematics of the blazars in our sample and their γ-ray behavior is beyond the scope of this work, here we present some simple relationships and correlations. It has been shown by the MOJAVE survey that the jets of γ-ray bright quasars have faster average apparent motions and brighter parsec-scale cores than those with weaker γ-ray fluxes (e.g., Kovalev et al. 2009; Lister et al. 2009, 2016). This relation implies that the jets of brighter γ-ray quasars have higher Doppler boosting factors. In order to determine if there is a relationship between the observed physical parameters of the sources in our sample and their γ-ray flux, we calculate the maximum γ-ray flux, $S_{\gamma,\rm max}^{\rm obs}$, (ignoring upper limits) of each source according to their 10 yr Fermi-LAT light curves.

In the analyses that follow, we have corrected the fluxes for redshift effects through $S = S^{\rm obs}(1 + z)^{1+\alpha}$, where $S^{\rm obs}$ is the observed flux, z is the redshift, and α is the spectral index of the source at the observed frequency. The $(1 + z)^\alpha$ factor is the k-correction, while the $(1 + z)^1$ factor accounts for the change in frequency interval. In the radio band, $\alpha_{43} \sim 0$. For the γ-ray spectral index, we have taken the observed power-law index p from the Fermi 4th Catalog of AGNs (Ajello et al. 2020), regardless of which spectral model best fits each source. Then, $\alpha_\gamma = |p + 1|$.

Figure 30 shows the relationship between $S_{\gamma,\rm max}$ and the apparent speed $\beta_{\rm app}$ and Doppler factor $\delta_{\rm var}$ of the "typical" knot of each source. The sample as a whole has a weak positive correlation between the physical parameters in the jet and $S_{\gamma,\rm max}$, with Pearson's r correlation coefficients of 0.361 and 0.274 for $\beta_{\rm app}$ and $\delta_{\rm var}$, respectively. The significant scatter is
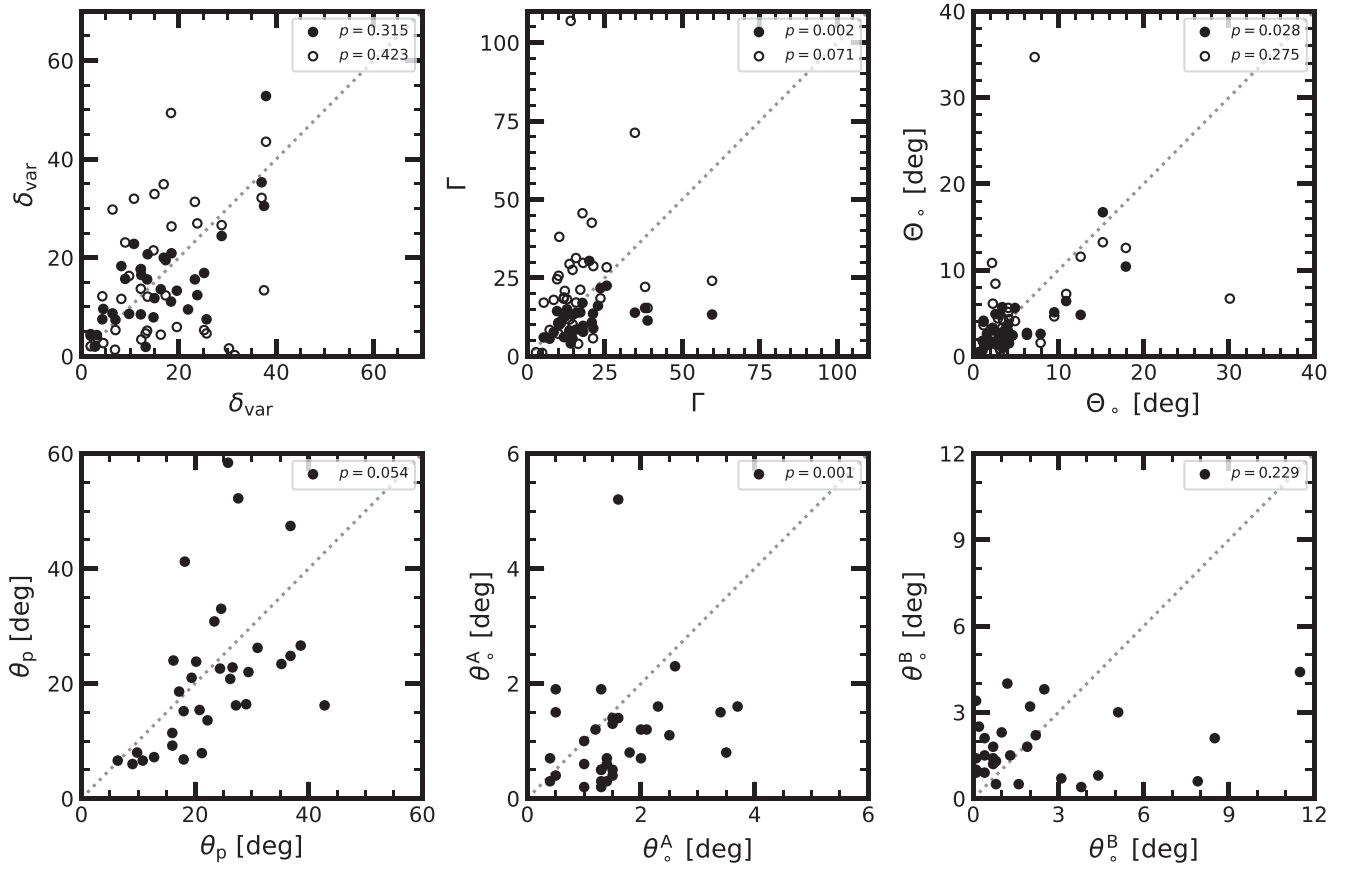
Figure 24. Comparisons of the physical parameters of blazar jets derived in this work (*x*-axis) with those derived in Jorstad et al. (2017; *y*-axis, filled circles) and Liodakis et al. (2018; *y*-axis, open circles). A gray dotted line showing a 1:1 relation is shown in each panel, and the *p*-value of a WRS test between the derived values (from Table 14) is given in the legend.

Table 14
Wilcoxon Rank-sum Test *p*-values between This Work and Previous Results

Parameter	Comparison Work	*p*-value
δ_{var}	Jorstad et al. (2017)	0.315
	Liodakis et al. (2018)	0.423
Γ	Jorstad et al. (2017)	0.002
	Liodakis et al. (2018)	0.071
$\Theta_{\circ}$	Jorstad et al. (2017)	0.028
	Liodakis et al. (2018)	0.275
θ_{p}	Jorstad et al. (2017)	0.054
$\theta_{\circ}^{A}$	Jorstad et al. (2017)	0.001
$\theta_{\circ}^{B}$	Jorstad et al. (2017)	0.229

indicative of the diversity in knot behaviors seen in each jet. Our sample consists of too few sources of each type to determine if there is a difference between the subclasses. However, even at the maxima in their γ-ray light curves, BL Lac objects and RGs are in general fainter than FSRQs, with lower speeds and Doppler factors (as expected in the standard AGN unification scheme; e.g., Urry & Padovani 1995).

To further investigate a connection between the γ-ray and 43 GHz radio behavior, in Figure 31 we show $S_{\gamma,max}$ compared to the maximum flux density of the core component *A0* in each source in Table 13 for which the physical parameters were calculated rather than estimated from the $\Gamma\theta_{\circ} \sim 0.2$ relation.
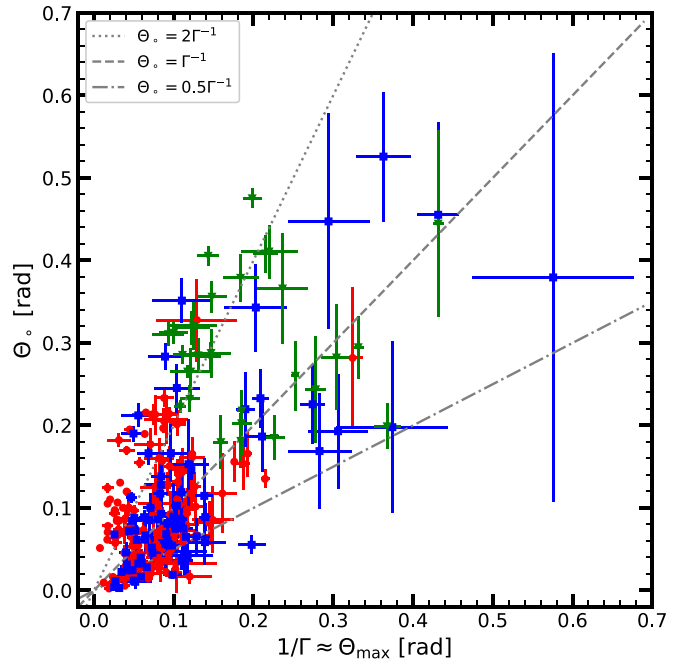
Figure 25. Observed viewing angle $\Theta_{\circ}$ vs. theoretical viewing angle $\Theta_{max} \approx \Gamma^{-1}$ for reliable knots in FSRQs (red circles), BL Lac objects (blue squares), and RGs (green triangles).
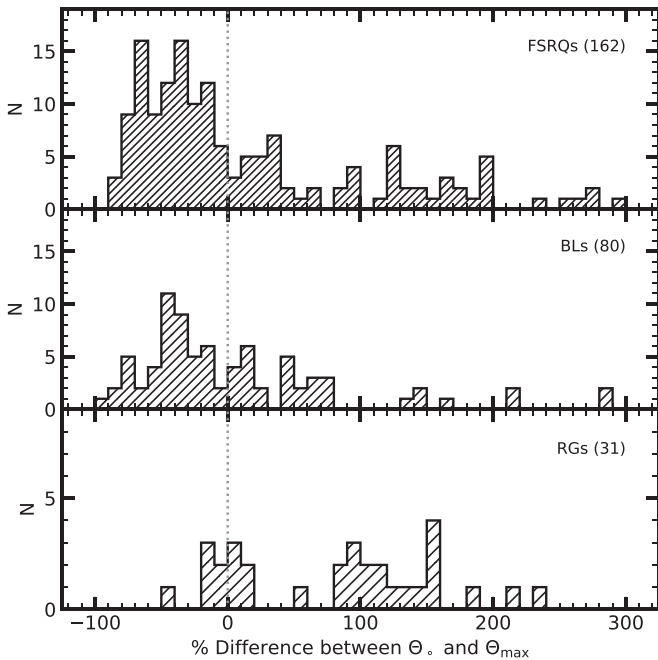
Figure 26. Distributions for FSRQs, BL Lac objects, and RGs of the percent difference between the observed viewing angle Θ_o and expected viewing angle $\Theta_{max} \approx \Gamma^{-1}$. A gray dotted line has been added at zero difference.

We find a $\sim 3\sigma$ positive correlation between $S_{\gamma,max}$ and the maximum core flux density of each source, with a Pearson's r coefficient of 0.465. We also see that the results of the core brightness temperature distributions from Section 3.1 extend to the maximum core flux densities, with the FSRQ cores generally brighter than the BL Lac object and RG cores.

The correlations observed here, while weak, support the conclusion of a connection between the activity states of a blazar at 43 GHz and at γ-ray energies. In general, the brighter the 43 GHz core of a source, and the faster the knots in a source appear to move down the jet, the brighter the jet can be at γ-rays. We plan to perform correlation analyses between the γ-ray and 43 GHz core light curves and comparisons between knot time of ejections and γ-ray outbursts for the whole sample in a future work.

7. Summary

We have presented a new analysis of the jet kinematics in 35 blazars and three RGs observed with the VLBA at 43 GHz over 10 yr under the VLBA-BU-BLAZAR program. The total observed time period is 2007 June through 2018 December, resulting in 3705 total intensity images of the jets. The first 5 yr of data were presented in Jorstad et al. (2017), and are included in this study as well after applying a new analysis procedure. The primary findings and conclusions of the 10 yr of data are summarized as follows:

1. We have implemented a new piecewise linear fitting method to derive the kinematics of moving components in the jets. This algorithm allows us to estimate the distance down the jet at which acceleration (if any) occurs. We have identified 559 distinct emission features, of which 38 are the 43 GHz cores, which are assumed to be stationary. We have further classified 96 components as quasi-stationary, leaving 425 knots that move with respect to the VLBI core. Among these moving knots, 75

exhibit nonlinear motion, for which we calculate the acceleration parallel and perpendicular to the jet direction.

2. To incorporate the presence of lower limits to the brightness temperature of 10.1% of all components into our analysis, we have used the Kaplan–Meier estimator for the survival function of the cores and knots to derive a median value of the brightness temperature for each source. We plan to provide a deeper analysis of the survival functions of the core and knot brightness temperatures, covering the temporal properties and whether all sources can be described with a similar parameterized survival function, in a future work (Z. R. Weaver 2022, in preparation).

3. We find, despite a low significance in a K-S test due to a small number of sources, that FSRQs and BL Lac objects have more intense cores than those of RGs, but the knots in the extended jets of BL Lac objects are significantly less intense than the knots of RGs and FSRQs. The brightness temperature distributions of the noncore components can be explained by Doppler boosting of the expected intrinsic brightness temperature.

4. With 10.5 yr of data, we have analyzed parsec-scale jet position angle variations of each source. We have quantitatively placed the jets into four categories. The majority of jets (23) have jet position angles that are constant with time, while a set of six sources has a very wide jet that is constant in position angle. Two sources, the FSRQs 0420−014 and 1226+023, have jet position angles that change linearly with time. The remaining seven sources have complex variations of position angle, which we have fit with third-order splines.

5. Due to our piecewise linear fitting method, any individual moving knot can have multiple motions over different time periods. We therefore have analyzed a total of 529 knot speeds. These speeds range from $0.01c$ to $78c$. The FSRQs generally have the fastest knots, with a distribution that peaks between $8c$–$10c$ and extends to $\sim 78c$. The distribution of apparent speeds for BL Lac objects peaks between $0c$–$2c$, as well as $8c$–$10c$, but only extends up to $\sim 30c$. RGs have a very narrow distribution of speeds, only extending to $\sim 10c$. We find superluminal motion in at least one knot of the RG 0316+413 of $\beta_{app} = 1.38c \pm 0.03c$, while the remaining superluminal knots in RGs come from 0415+379 and 0430+052. The moving knots in FSRQs tend to travel in the same direction, while knots of BL Lac objects show larger variations in the direction of motion.

6. On average, there exist ~ 2 quasi-stationary features in the jet of each FSRQ, ~ 3 in each BL, and ~ 6 in each RG. Almost half of these features have appeared or disappeared during the 10.5 yr observation period, indicating that they may be transient. The locations of the majority of stationary features are concentrated within 1 mas of the core (projected), independent of the subclass. We have characterized the fluctuations in the positions of these features using confidence ellipses, which show that the stationary features in RGs tend to "slosh" around the average position in a direction parallel to the jet axis. However, there is no clear preference of directional shifts for the stationary features of BL Lac objects and FSRQs.

Table 15
Average Physical Parameters of AGN Jets for Different Subclasses

Subclass	N_s	$\overline{\delta}$	$\overline{\Gamma}$	$\overline{\Theta}_\circ$ (deg)	$\overline{\theta}_\circ^{\mathrm{A}}$ (deg)	$\overline{\theta}_\circ^{\mathrm{B}}$ (deg)
(1)	(2)	(3)	(4)	(5)	(6)	(7)
FSRQ	22[a]	7.1 ± 6.1	16.0 ± 4.7	4.0 ± 2.3	1.2 ± 0.9	1.2 ± 1.5
BL	11	3.7 ± 4.3	5.5 ± 4.1	2.7 ± 2.2	0.7 ± 0.8	1.3 ± 1.1
RG	2	2.6 ± 0.5	8.6 ± 0.6	15.7 ± 1.5	2.4 ± 0.4	5.3 ± 4.0

Note.
[a] Because the source 1611+343 only has one reliable superluminal knot, there is no estimate for $\theta_\circ^{\mathrm{B}}$ for this source, and 21 sources were used to calculate $\overline{\theta}_\circ^{\mathrm{B}}$.
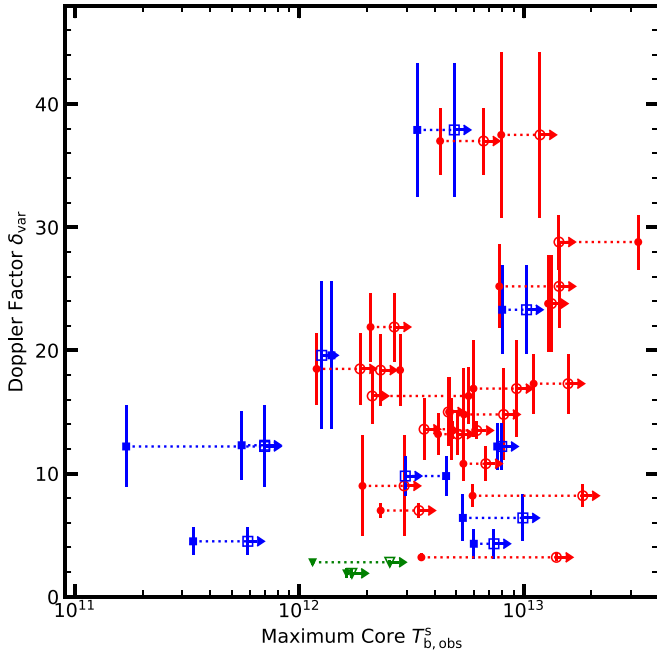
Figure 27. Typical Doppler factor of variability for each source vs. the maximum brightness temperature of the core, $A0$, for resolved (closed symbols) and unresolved (open symbols with right-facing arrows, component size $a \leqslant 0.02$ mas) epochs. FSRQs are shown in red circles, BL Lac objects in blue squares, and RGs in green triangles.
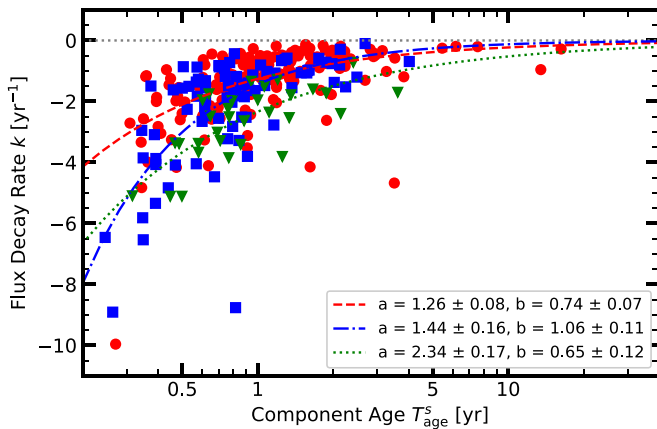
Figure 28. Flux decay rate k for reliable knots vs. the age of the feature in the host-galaxy frame, T_{age}^s, for FSRQ (red circles), BL Lac object (blue squares), and RG knots (green triangles). Fits to the model $k = -a(T_{\mathrm{age}}^s)^{-b}$ are plotted in the same color as the subtype of blazar, with values as indicated in the legend.

7. We have detected 104 different acceleration regions in the sample. Only a few BL Lac objects have knots with discernible acceleration. We find that, statistically, these accelerations are consistent with changes in the Lorentz factor of the knots rather than changes in the jet direction. Parallel to the jet axis, we see an initial positive acceleration close to the core of the jet (<5 pc), while beyond 10 pc, the knots tend to decelerate. Perpendicular to the jet axis, we find an initial positive acceleration for projected distances 0–1 pc from the core and negative acceleration 1–2 pc from the core. Beyond ~ 5 pc, we see very small magnitudes of acceleration. Similar trends are found farther from the core at longer wavelengths (e.g., Homan et al. 2015).

8. To test whether interactions with standing shocks have an effect on the moving knots, we have paired the acceleration regions with the closest (on average) stationary features. We have found that few pairs fail to follow an expected 1:1 relation, indicating that accelerations take place at or beyond the stationary features. Such behavior is expected if the stationary features are structural components, such as recollimation shocks.

9. We have derived Doppler factors of variability, δ_{var}, for a subset of reliable knots in the sample, which, along with the measured apparent speeds, have allowed us to calculate the Lorentz factors Γ and viewing angle $\Theta_\circ$. The flux decays of the knots in our sample are statistically likely to be caused by radiative losses (modulated by light-travel delays) rather than adiabatic expansion.

10. The Lorentz factors of knots in the jets of our sample range from 2–60, with faster knots observed in FSRQs than in BL Lac objects and RGs. Our results agree with the expectation that the jets of RGs lie at larger viewing angles with respect to the line of sight, with an average $\Theta_\circ \sim 15°$–$30°$, compared to the FSRQ and BL Lac object jets with peak viewing angles $\sim 0°$–$4°$.

11. For most of the jets in our sample, we see a wide diversity in the apparent speeds and Doppler factors of knots moving down the parsec-scale jet. For sources with many observed knots (such as the RG 0415+379), we see that this diversity can be explained by a distribution of physical parameters from which a knot's parameters can be drawn statistically. Whether the distributions of knot parameters are similar for different sources remains unclear, as many of our sources will likely require a further 5–10 yr of monitoring for enough knots to be observed to determine their distributions robustly.

12. We have defined the "typical" knot in each jet by choosing the fastest knot with the smallest uncertainty in β_{app} and δ_{var} to represent the jet as a whole. From these typical values, we calculate the Lorentz factor and viewing angle of each jet, and find that, on average,
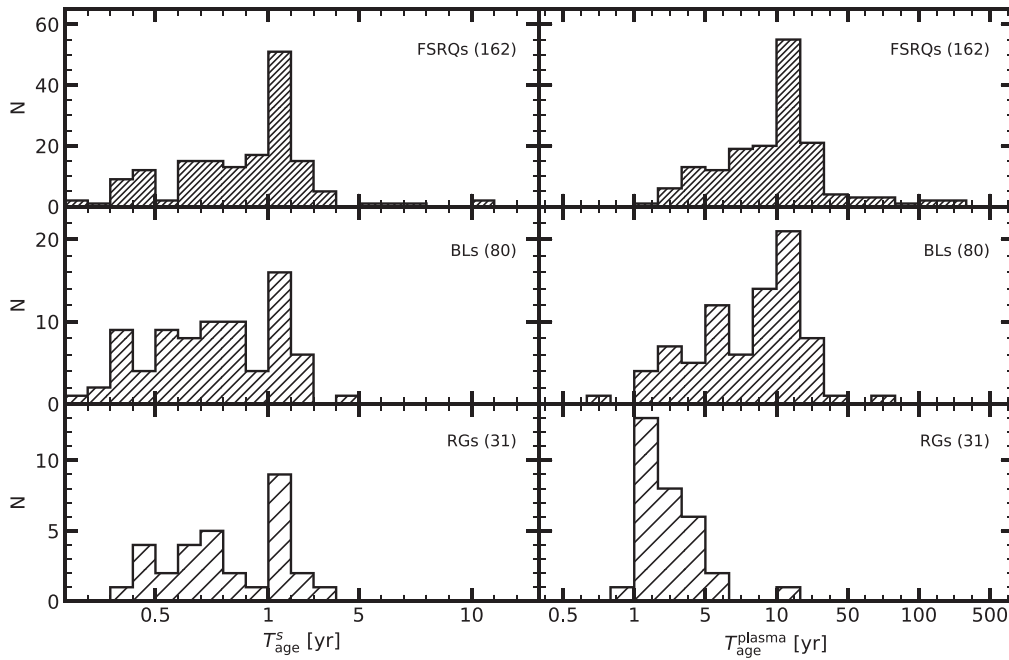
Figure 29. Distributions of the age of reliable knots in the host-galaxy frame, $T_{age}^{s} = T_{age}/(1 + z)$ (left), and plasma frame, $T_{age}^{plasma} = \delta_{var} T_{age}/(1 + z)$ (right), in FSRQs (top), BL Lac objects (middle), and RGs (bottom). Values in parentheses are the number of knots in each distribution. Note that the age scale is neither linear nor logarithmic.
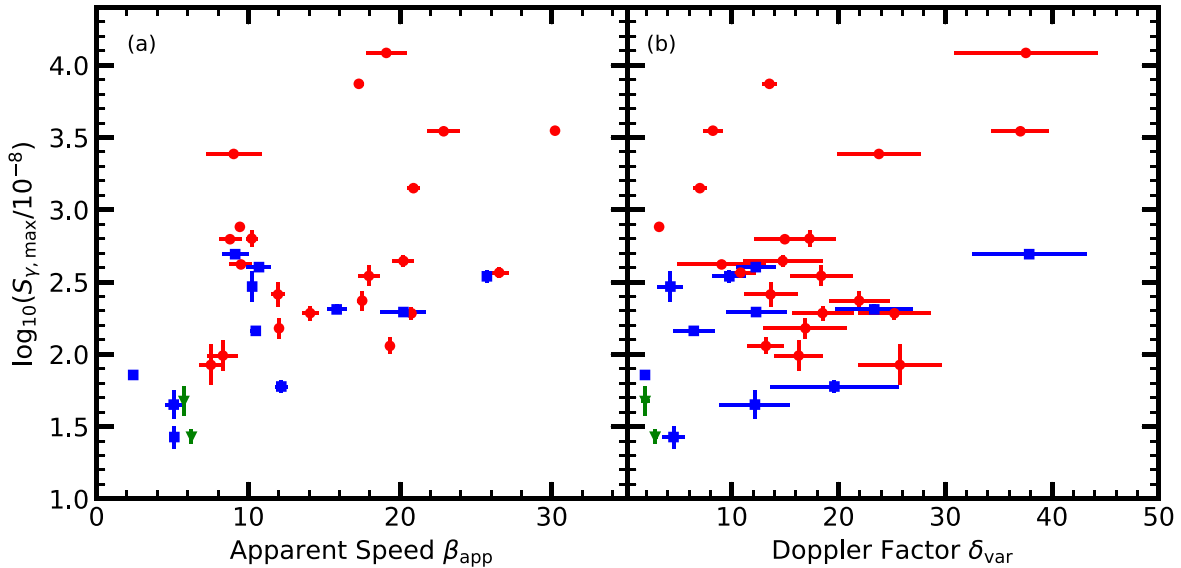

Figure 30. Maximum γ-ray flux $S_{\gamma,max}$ (scaled by 10^{-8} ph cm^{-2} s^{-1}) vs. (a) apparent speed β_{app} and (b) Doppler factor δ_{var} of the "typical" knot in FSRQs (red circles), BL Lac objects (blue squares), and RGs (green triangles).

FSRQ jets have higher values of δ_{var} and Γ compared to BL Lac objects, while knots in RGs are slower and have much wider viewing angles and intrinsic opening semi-angles. The physical parameters of each jet as calculated using the "typical" knot are statistically similar to other estimates of the physical parameters determined through lower-frequency monitoring (e.g., Liodakis et al. 2018), which probes farther distances from the core.

13. In general, the knots of FSRQs are longer lived than the knots of BL Lac objects and RGs, reaching farther projected distances from the core. The knots of FSRQs and BL Lac objects have flux decay rates that are related to their age roughly as $k \sim -2T_{age}^{-1}$ despite the differences

in their age distributions, while RG knots follow $k \sim 2.4T_{age}^{-0.65}$. The distribution of ages of all subclasses peaks in the 1–2 yr range despite large differences in the physical sizes of knots of RGs versus BL Lac objects and FSRQs. This can be explained by the lower Doppler factors of the RGs.

14. We find weak correlations between the maximum γ-ray flux and the typical apparent speeds and Doppler factors of jets in our sample. We also find that the blazars with brighter 43 GHz cores typically reach higher maximum γ-ray fluxes. We plan to perform a temporal analysis comparing the ejection times of knots in our sample with γ-ray outbursts in a future study.
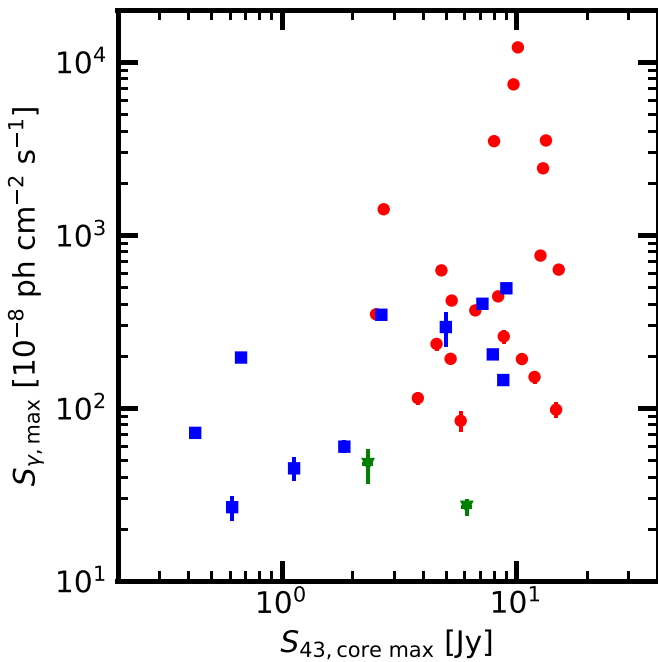
Figure 31. Maximum γ-ray flux, $S_{\gamma,\max}$ vs. maximum core flux density at 43 GHz, $S_{43,\text{core max}}$, for FSRQs (red circles), BL Lac objects (blue squares), and RGs (green triangles).

---

[17] https://www.astropy.org

Appendix
Survival Analysis of Jet Component Brightness Temperatures

Treatment of data with lower and upper limits (or, more generally, right- and left-censored data, respectively) in astronomy has been performed in a number of fashions, of which many are biased or incorrect (Feigelson & Babu 2012). For example, if the number of limits is small, then they are unlikely to change the result of statistical tests; however, they will bias the results as the number of limits in a sample grows. The most statistically rigorous procedures consider all of the data points, both detected values and censored data, to model the properties of a parent distribution of the variable in question under specific mathematical constraints. Such procedures fall under the umbrella of "survival analysis" (Avni et al. 1980; Feigelson & Nelson 1985; Schmitt 1985; Avni & Tananbaum 1986; Isobe et al. 1986; LaValley et al. 1992). A few methods for censored data have been developed specifically for astronomical contexts (Akritas et al. 1995; Akritas & Siebert 1996).

Most survival analysis techniques are based on estimating the "survival function" of an entire data set (observations and censored data), where the survival function of a parameter, x, is

$$\mathcal{S}(x) = \Pr(X > x). \qquad (A1)$$

That is, $\mathcal{S}(x)$ is the probability that the value of x, and X, is above a specified value. Alternatively, one may estimate the "hazard function," $\mathcal{H}(x)$:

$$\begin{aligned} \mathcal{H}(x) &= \frac{d \ln \mathcal{S}(x)}{dx} \\ &= \lim_{\Delta x \to 0} \frac{\Pr(x < X < x + \Delta x | X > x)}{\Delta x}. \end{aligned} \qquad (A2)$$

The focus on the survival and hazard function of data in survival analysis is due to their relation to the common statistical concepts of probability density functions (PDFs), $f(x)$, and cumulative distribution functions, $F(x)$, of data through $f(x) = \mathcal{S}(x)\mathcal{H}(x)$ and $F(x) = 1 - \mathcal{S}(x)$. Thus, estimates of $\mathcal{S}(x)$ and $\mathcal{H}(x)$ can describe the underlying parent distributions of the data, even in the presence of censored or truncated[18] data, depending on the estimator.

In order to determine a "typical" brightness temperature for each source in our sample, we estimate the survival function of the $\log_{10}$ of the brightness temperature of cores and knots, $\mathcal{S}(\log_{10} T_{\text{b,obs}}^{\text{s}})$, using the Kaplan–Meier estimator implemented as part of the lifelines[19] package (Davidson-Pilon 2019). The Kaplan–Meier estimator (Kaplan & Meier 1958) is a nonparametric method to estimate $\mathcal{S}(x)$ and was developed to directly take right-censored data into account:

$$\hat{\mathcal{S}}(x) = \prod_{i:x_i<x} \left(1 - \frac{d_i}{n_i}\right) \qquad (A3)$$

where x_i is a discrete value of the parameter of interest x with at least one observed or censored data point, d_i is the number of "events" (observed data) up to that value, and n_i is the total

---

[18] Truncated data occur when no information, not even an upper or lower limit, is known for a quantity of interest, such as in the case of surveys of astronomical objects being truncated at some sensitivity limit.
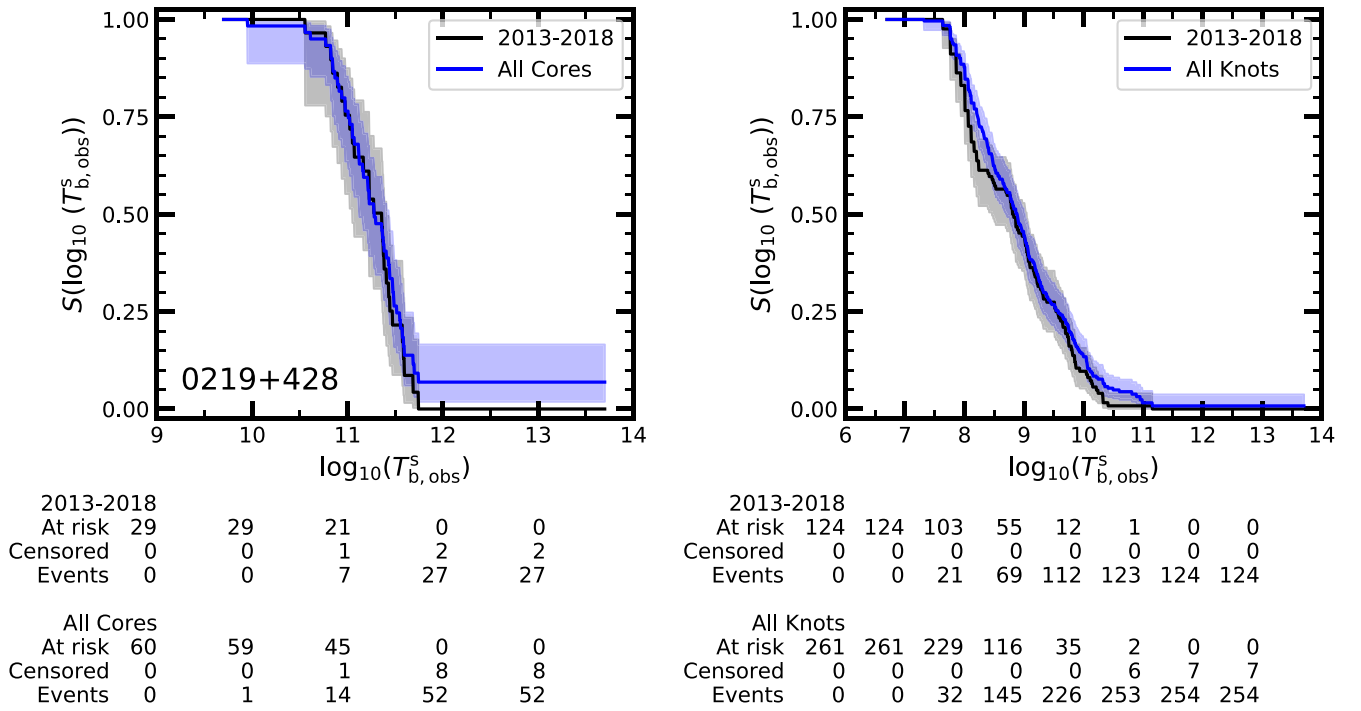[19] https://lifelines.readthedocs.io/en/latest/index.html

Figure 32. Kaplan–Meier estimated survival functions of the brightness temperature of cores (left) and knots (right) in the BL Lac object 0219+428. The survival function for components observed between 2013 January and 2018 December are shown in black, while those observed between 2007 June and 2018 December are shown in blue. Shaded regions represent 95% confidence intervals to the survival function. The tables below each panel show the summary statistics of each survival function in the form of the number of unused ("At risk," both observed and censored), censored, and observed ("event") data points at each major interval (included per the recommendation by Morris et al. 2019).

(The complete figure set (38 images) is available.)

number of data points "known to survive" past x_i (have a value $x > x_i$ or are censored).

Figure 32 shows, as an example, the Kaplan–Meier estimates for the survival function of the cores (left) and knots (right) of the BL Lac object 0219+428 for both the time period presented here (2013 January–2018 December) as well as the total observed time period (2007 June–2018 December). Figure 32 contains similar plots for all sources in our sample. Doubling the number of brightness temperatures used by combining those presented in this work with those presented in Jorstad et al. (2017) yields better estimates for the survival function, increasing the resolution along $T_{b,obs}^s$ and resulting in narrower confidence intervals along the curve. The two sources added after 2013, the BL Lac objects 1652+398 and 1959+650, have the same survival functions presented in the two time periods.

To determine a "typical" brightness temperature for the core and knots of a source, we calculate the median of the survival function, i.e., where $\mathcal{S}(\log_{10} T_{b,obs}^s) = 0.5$, for each time period. These median brightness temperatures, with 95% confidence intervals, are given in Table A1. Due to the low number of core
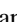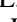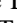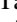
components observed for the BL Lac object 1959+650 ($N = 6$), we use the lower confidence interval as a lower limit to the brightness temperature of the core for the source (among all 13 BL Lac objects, a single lower limit will not significantly affect the results).

We note that this analysis is based on a few approximations, such as nonvariability of the brightness temperature of components and similar properties of sources within each subclass. It is not expected a priori that the survival function of the component brightness temperatures for a source should be the same for different time periods (e.g., the faster decrease in the survival function for knots observed from 2013 January to 2018 December versus knots observed during the entire time period for the BL Lac object 0219+428 near brightness temperatures $\sim 10^8$ K, as in Figure 32). However, temporal analysis of the brightness temperatures in the jets of blazars as well as an investigation into the assumptions outlined above are beyond the scope of this paper, which is focused on the kinematics of the features. We plan to present such an analysis in a separate publication (Z. R. Weaver 2022, in preparation).

Table A1
Median Brightness Temperatures of Source Components as Determined through Survival Analysis

Source	Core Median $T_{\rm b,obs}^{\rm s}$ $\times 10^{10}$ (K)		Knot Median $T_{\rm b,obs}^{\rm s}$ $\times 10^{8}$ (K)	
	2013–2018	2007–2018	2013–2018	2007–2018
(1)	(2)	(3)	(4)	(5)
0219+428	$22.94^{+2.68}_{-11.66}$	$19.08^{+8.00}_{-5.76}$	$6.43^{+4.70}_{-3.51}$	$7.68^{+2.58}_{-2.47}$
0235+164	$29.70^{+15.27}_{-9.54}$	$52.12^{+9.41}_{-10.35}$	$73.47^{+99.32}_{-28.91}$	$178.45^{+97.42}_{-89.28}$
0316+413	$15.43^{+2.29}_{-1.36}$	$14.74^{+0.98}_{-0.92}$	$108.22^{+14.91}_{-16.13}$	$144.69^{+12.15}_{-15.45}$
0336-019	$50.70^{+38.27}_{-16.91}$	$43.34^{+15.41}_{-9.55}$	$121.16^{+133.33}_{-55.53}$	$121.16^{+113.61}_{-59.63}$
0415+379	$13.82^{+4.07}_{-4.52}$	$15.87^{+4.30}_{-2.05}$	$35.55^{+9.01}_{-9.81}$	$34.42^{+8.72}_{-8.68}$
0420-014	$62.10^{+29.36}_{-19.15}$	$62.67^{+18.46}_{-11.03}$	$23.75^{+21.53}_{-14.43}$	$159.39^{+215.45}_{-65.80}$
0430+052	$14.47^{+5.33}_{-3.08}$	$15.87^{+3.75}_{-4.48}$	$40.45^{+13.63}_{-13.43}$	$34.42^{+8.03}_{-15.16}$
0528+134	$68.72^{+19.42}_{-11.04}$	$102.16^{+25.30}_{-27.49}$	$29.29^{+15.27}_{-14.89}$	$45.28^{+16.25}_{-11.95}$
0716+714	$292.24^{+158.50}_{-119.45}$	$180.94^{+66.61}_{-29.07}$	$43.14^{+132.46}_{-16.12}$	$49.09^{+46.03}_{-18.84}$
0735+178	$10.77^{+\infty}_{-7.37}$	$3.02^{+0.89}_{-0.46}$	$4.03^{+3.17}_{-0.71}$	$3.48^{+1.57}_{-0.47}$
0827+243	$38.45^{+15.63}_{-9.82}$	$36.71^{+19.39}_{-6.46}$	$54.96^{+62.35}_{-19.98}$	$104.78^{+35.31}_{-49.82}$
0829+046	$19.26^{+5.22}_{-3.54}$	$11.92^{+4.69}_{-2.54}$	$20.54^{+47.24}_{-8.67}$	$13.94^{+6.60}_{-2.07}$
0836+710	$70.65^{+40.35}_{-16.58}$	$63.84^{+15.81}_{-10.26}$	$72.30^{+35.92}_{-21.60}$	$43.14^{+18.39}_{-8.72}$
0851+202	$396.16^{+140.87}_{-139.31}$	$292.24^{+158.50}_{-72.65}$	$106.49^{+139.92}_{-55.79}$	$115.43^{+68.87}_{-38.31}$
0954+658	$174.39^{+276.35}_{-69.36}$	$104.06^{+18.78}_{-25.14}$	$62.53^{+25.21}_{-23.99}$	$63.54^{+12.34}_{-20.40}$
1055+018	$203.98^{+119.45}_{-75.34}$	$184.30^{+56.49}_{-36.58}$	$357.13^{+1494.43}_{-235.97}$	$184.30^{+818.63}_{-102.04}$
1101+384	$3.73^{+0.71}_{-0.66}$	$3.47^{+0.63}_{-0.39}$	$1.46^{+0.52}_{-0.42}$	$1.80^{+0.45}_{-0.34}$
1127-145	$8.55^{+9.66}_{-3.11}$	$28.62^{+10.90}_{-8.08}$	$17.48^{+18.07}_{-12.82}$	$17.76^{+6.38}_{-9.17}$
1156+295	$94.03^{+23.29}_{-14.38}$	$94.90^{+23.50}_{-15.25}$	$26.16^{+26.20}_{-9.51}$	$35.55^{+17.66}_{-11.41}$
1219+285	$5.06^{+1.93}_{-2.57}$	$4.13^{+1.17}_{-1.64}$	$13.72^{+9.65}_{-7.60}$	$8.59^{+3.47}_{-2.94}$
1222+216	$14.34^{+15.64}_{-5.62}$	$41.39^{+18.46}_{-13.29}$	$29.77^{+8.15}_{-8.56}$	$39.16^{+16.69}_{-6.89}$
1226+023	$36.71^{+10.38}_{-10.13}$	$39.89^{+11.75}_{-5.47}$	$140.09^{+56.50}_{-33.60}$	$117.31^{+25.06}_{-15.85}$
1253-055	$317.52^{+340.27}_{-89.68}$	$281.66^{+38.81}_{-60.03}$	$517.59^{+208.74}_{-111.26}$	$485.24^{+195.69}_{-78.91}$
1308+326	$36.04^{+26.63}_{-12.46}$	$33.79^{+9.55}_{-6.46}$	$127.17^{+202.28}_{-89.25}$	$485.24^{+163.52}_{-213.78}$
1406-076	$37.05^{+12.72}_{-9.47}$	$31.10^{+6.64}_{-11.12}$	$44.56^{+95.53}_{-15.27}$	$42.45^{+19.08}_{-13.63}$
1510-089	$84.96^{+58.73}_{-22.86}$	$70.65^{+15.89}_{-20.42}$	$73.47^{+62.17}_{-33.67}$	$84.96^{+26.81}_{-34.26}$
1611+343	$22.52^{+8.01}_{-10.93}$	$16.92^{+11.97}_{-6.45}$	$137.85^{+156.42}_{-73.27}$	$15.36^{+12.10}_{-4.93}$
1622-297	$8.32^{+26.10}_{-3.49}$	$8.71^{+4.00}_{-3.56}$	$90.62^{+136.69}_{-51.46}$	$109.98^{+86.61}_{-36.51}$
1633+382	$166.53^{+26.47}_{-34.28}$	$156.12^{+18.26}_{-22.65}$	$18.64^{+6.69}_{-4.47}$	$14.87^{+7.04}_{-3.19}$
1641+399	$147.72^{+50.69}_{-46.50}$	$105.02^{+26.01}_{-23.90}$	$36.13^{+7.71}_{-7.31}$	$27.91^{+4.88}_{-3.77}$
1652+398	$0.72^{+0.38}_{-0.22}$	$0.72^{+0.38}_{-0.22}$	$2.69^{+0.63}_{-0.61}$	$2.69^{+0.63}_{-0.61}$
1730-130	$209.70^{+151.57}_{-77.45}$	$153.27^{+85.32}_{-52.98}$	$60.54^{+24.42}_{-18.09}$	$61.53^{+30.56}_{-14.76}$
1749+096	$221.62^{+92.98}_{-64.06}$	$247.55^{+69.97}_{-74.76}$	$46.02^{+69.41}_{-17.20}$	$55.85^{+111.45}_{-18.54}$
1959+650	$1.64^{+\infty}_{-0.00}$	$1.64^{+\infty}_{-0.00}$	$1.58^{+3.47}_{-1.27}$	$1.58^{+3.47}_{-1.27}$
2200+420	$329.45^{+270.41}_{-138.22}$	$259.23^{+85.76}_{-49.53}$	$6.64^{+1.68}_{-1.08}$	$9.78^{+1.35}_{-0.90}$
2223-052	$10.77^{+2.06}_{-1.81}$	$12.14^{+2.06}_{-1.67}$	$19.26^{+8.65}_{-5.32}$	$40.45^{+22.08}_{-13.43}$
2230+114	$335.58^{+154.15}_{-96.99}$	$145.02^{+93.57}_{-23.30}$	$24.53^{+15.27}_{-7.88}$	$28.36^{+12.74}_{-6.45}$
2251+158	$149.09^{+80.86}_{-55.06}$	$256.85^{+128.50}_{-94.86}$	$1122.85^{+669.92}_{-212.45}$	$774.75^{+212.13}_{-204.55}$

ORCID iDs

Zachary R. Weaver ⓘ https://orcid.org/0000-0001-6314-0690
Svetlana G. Jorstad ⓘ https://orcid.org/0000-0001-6158-1708
Alan P. Marscher ⓘ https://orcid.org/0000-0001-7396-3332
Daria A. Morozova ⓘ https://orcid.org/0000-0002-9407-7804
Ivan S. Troitsky ⓘ https://orcid.org/0000-0002-4218-0148
Iván Agudo ⓘ https://orcid.org/0000-0002-3777-6182
José L. Gómez ⓘ https://orcid.org/0000-0003-4190-7613
Anne Lähteenmäki ⓘ https://orcid.org/0000-0002-0393-0647
Joni Tammi ⓘ https://orcid.org/0000-0002-9164-2695
Merja Tornikoski ⓘ https://orcid.org/0000-0003-1249-6026

References

Abdo, A. A., Ackermann, M., Ajello, M., et al. 2010, ApJS, 188, 405
Acero, F., Ackermann, M., Ajello, M., et al. 2015, ApJS, 218, 23

Agudo, I. 2009, in ASP Conf. Ser. 402, Approaching Micro-Arcsecond Resolution with VSOP-2: Astrophysics and Technologies, ed. Y. Hagiwara et al. (San Francisco, CA: ASP), 330
Agudo, I., Bach, U., Krichbaum, T. P., et al. 2007, A&A, 476, L17
Agudo, I., Jorstad, S. G., Marscher, A. P., et al. 2011a, ApJL, 726, L13
Agudo, I., Marscher, A. P., Jorstad, S. G., et al. 2011b, ApJL, 735, L10
Agudo, I., Marscher, A. P., Jorstad, S. G., et al. 2012, ApJ, 747, 63
Aharonian, F., Akhperjanian, A. G., Bazer-Bachi, A. R., et al. 2007, ApJL, 664, L71
Ajello, M., Angioni, R., Axelsson, M., et al. 2020, ApJ, 892, 105
Akritas, M. G., Murphy, S. A., & Lavalley, M. P. 1995, J. Am. Stat. Assoc., 90, 170
Akritas, M. G., & Siebert, J. 1996, MNRAS, 278, 919
Aleksić, J., Antonelli, L. A., Antoranz, P., et al. 2011, ApJL, 730, L8
Angel, J. R. P., & Stockman, H. S. 1980, ARA&A, 18, 321
Asada, K., Nakamura, M., Inoue, M., Kameno, S., & Nagai, H. 2010, ApJ, 720, 41
Astropy Collaboration, Price-Whelan, A. M., Sipőcz, B. M., et al. 2018, AJ, 156, 123

Astropy Collaboration, Robitaille, T. P., Tollerud, E. J., et al. 2013, A&A, 558, A33
Attridge, J. M., Roberts, D. H., & Wardle, J. F. C. 1999, ApJL, 518, L87
Avni, Y., Soltan, A., Tananbaum, H., & Zamorani, G. 1980, ApJ, 238, 800
Avni, Y., & Tananbaum, H. 1986, ApJ, 305, 83
Bach, U., Krichbaum, T. P., Ros, E., et al. 2005, A&A, 433, 815
Beskin, V. S., & Kuznetsova, I. V. 2000, NCimB, 115, 795
Blandford, R. D., McKee, C. F., & Rees, M. J. 1977, Natur, 267, 211
Blandford, R. D., & Payne, D. G. 1982, MNRAS, 199, 883
Blandford, R. D., & Znajek, R. L. 1977, MNRAS, 179, 433
Blasi, M. G., Lico, R., Giroletti, M., et al. 2013, A&A, 559, A75
Bowker, A., & Lieberman, G. 1972, Engineering Statistics (Englewood Cliffs, NJ: Prentice-Hall)
Britzen, S., Fendt, C., Witzel, G., et al. 2018, MNRAS, 478, 3199
Britzen, S., Fendt, C., Zajacek, M., et al. 2019, Galax, 7, 72
Britzen, S., Qian, S. J., Steffen, W., et al. 2017, A&A, 602, A29
Britzen, S., Witzel, A., Krichbaum, T. P., et al. 2005, MNRAS, 362, 966
Bruni, G., Gómez, J. L., Vega-García, L., et al. 2021, A&A, 654, A27
Casadio, C., Gómez, J. L., Jorstad, S. G., et al. 2015, ApJ, 813, 51
Casadio, C., MacDonald, N. R., Boccardi, B., et al. 2021, A&A, 649, A153
Celotti, A., Ghisellini, G., & Chiaberge, M. 2001, MNRAS, 321, L1
Cerruti, M., Zech, A., Boisson, C., et al. 2019, MNRAS, 483, L12
Chatterjee, K., Liska, M., Tchekhovskoy, A., & Markoff, S. B. 2019, MNRAS, 490, 2200
Chatterjee, R., Marscher, A. P., Jorstad, S. G., et al. 2011, ApJ, 734, 43
Chen, L. 2018, ApJS, 235, 39
Clausen-Brown, E., Savolainen, T., Pushkarev, A. B., Kovalev, Y. Y., & Zensus, J. A. 2013, A&A, 558, A144
Cohen, M. H., Cannon, W., Purcell, G. H., et al. 1971, ApJ, 170, 207
Cohen, M. H., Kellermann, K. I., Shaffer, D. B., et al. 1977, Natur, 268, 405
Conway, J. E., & Wrobel, J. M. 1995, ApJ, 439, 98
D'Arcangelo, F. D., Marscher, A. P., Jorstad, S. G., et al. 2009, ApJ, 697, 985
Davidson-Pilon, C. 2019, JOSS, 4, 1317
Event Horizon Telescope Collaboration, Akiyama, K., Alberdi, A., et al. 2019, ApJL, 875, L1
Fan, J.-H., Bastieri, D., Yang, J.-H., et al. 2014, RAA, 14, 1135
Fan, J.-H., Yang, J.-H., Liu, Y., & Zhang, J.-Y. 2013, RAA, 13, 259
Feigelson, E. D., & Babu, G. J. 2012, Modern Statistical Methods for Astronomy (Cambridge: Cambridge University Press)
Feigelson, E. D., & Nelson, P. I. 1985, ApJ, 293, 192
Fromm, C. M., Ros, E., Perucho, M., et al. 2013, A&A, 557, A105
Fuhrmann, L., Larsson, S., Chiang, J., et al. 2014, MNRAS, 441, 1899
Gabuzda, D. C., Reichstein, A. R., & O'Neill, E. L. 2014, MNRAS, 444, 172
Ghisellini, G., Padovani, P., Celotti, A., & Maraschi, L. 1993, ApJ, 407, 65
Ghisellini, G., Tavecchio, F., & Chiaberge, M. 2005, A&A, 432, 401
Giovannini, G., Savolainen, T., Orienti, M., et al. 2018, NatAs, 2, 472
Giroletti, M., Giovannini, G., Feretti, L., et al. 2004, ApJ, 600, 127
González-Morán, A. L., Chávez, R., Terlevich, E., et al. 2021, MNRAS, 505, 1441
Hallum, M. K., Jorstad, S. G., Larionov, V. M., et al. 2022, ApJ, 926, 180
Hartman, R. C., Bertsch, D. L., Bloom, S. D., et al. 1999, ApJS, 123, 79
H.E.S.S. Collaboration, Abdalla, H., Adam, R., et al. 2021, A&A, 648, A23
Homan, D. C., Kadler, M., Kellermann, K. I., et al. 2009, ApJ, 706, 1253
Homan, D. C., Kovalev, Y. Y., Lister, M. L., et al. 2006, ApJL, 642, L115
Homan, D. C., Lister, M. L., Kovalev, Y. Y., et al. 2015, ApJ, 798, 134
Homan, D. C., Ojha, R., Wardle, J. F. C., et al. 2002, ApJ, 568, 99
IceCube Collaboration, Aartsen, M. G., Ackermann, M., et al. 2018a, Sci, 361, 147
IceCube Collaboration, Aartsen, M. G., Ackermann, M., et al. 2018b, Sci, 361, eaat1378
Isler, J. C., Urry, C. M., Bailyn, C., et al. 2015, ApJ, 804, 7
Isobe, T., Feigelson, E. D., & Nelson, P. I. 1986, ApJ, 306, 490
Jekel, C. F., & Venter, G. 2019, pwlf: A Python Library for Fitting 1D Continuous Piecewise Linear Functions, https://github.com/cjekel/piecewise_linear_fit_py
Jorstad, S., & Marscher, A. 2016, Galax, 4, 47
Jorstad, S. G., Marscher, A. P., Lister, M. L., et al. 2004, AJ, 127, 3115
Jorstad, S. G., Marscher, A. P., Lister, M. L., et al. 2005, AJ, 130, 1418
Jorstad, S. G., Marscher, A. P., Mattox, J. R., et al. 2001a, ApJ, 556, 738
Jorstad, S. G., Marscher, A. P., Mattox, J. R., et al. 2001b, ApJS, 134, 181
Jorstad, S. G., Marscher, A. P., Morozova, D. A., et al. 2017, ApJ, 846, 98
Jorstad, S. G., Marscher, A. P., Smith, P. S., et al. 2013, ApJ, 773, 147
Joshi, M., Marscher, A. P., & Böttcher, M. 2014, ApJ, 785, 132
Kaplan, E. L., & Meier, P. 1958, J. Am. Stat. Assoc., 53, 457

Keivani, A., Murase, K., Petropoulou, M., et al. 2018, ApJ, 864, 84
Kellermann, K. I., Lister, M. L., Homan, D. C., et al. 2004, ApJ, 609, 539
Kellermann, K. I., Vermeulen, R. C., Zensus, J. A., & Cohen, M. H. 1998, AJ, 115, 1295
Komissarov, S. S. 2001, MNRAS, 326, L41
Komissarov, S. S. 2005, MNRAS, 359, 801
Königl, A. 1981, ApJ, 243, 700
Kovalev, Y. Y., Aller, H. D., Aller, M. F., et al. 2009, ApJL, 696, L17
Kovalev, Y. Y., Kardashev, N. S., Kellermann, K. I., et al. 2016, ApJL, 820, L9
Kovalev, Y. Y., Pushkarev, A. B., Nokhrina, E. E., et al. 2020, MNRAS, 495, 3576
Krawczynski, H., Hughes, S. B., Horan, D., et al. 2004, ApJ, 601, 151
Lähteenmäki, A., & Valtaoja, E. 1999, ApJ, 521, 493
Lähteenmäki, A., & Valtaoja, E. 2003, ApJ, 590, 95
Larionov, V. M., Jorstad, S. G., Marscher, A. P., et al. 2013, ApJ, 768, 40
Larionov, V. M., Jorstad, S. G., Marscher, A. P., et al. 2020, MNRAS, 492, 3829
LaValley, M., Isobe, T., & Feigelson, E. 1992, in ASP Conf. Ser. 25, Astronomical Data Analysis Software and Systems I, ed. D. M. Worrall, C. Biemesderfer, & J. Barnes (San Francisco, CA: ASP), 245
León-Tavares, J., Chavushyan, V., Lobanov, A., Valtaoja, E., & Arshakian, T. G. 2015, in IAU Symp. 313, Extragalactic Jets from Every Angle, ed. F. Massaro et al. (Cambridge: Cambridge University Press), 43
León-Tavares, J., Chavushyan, V., Patiño-Álvarez, V., et al. 2013, ApJL, 763, L36
León-Tavares, J., Valtaoja, E., Tornikoski, M., Lähteenmäki, A., & Nieppola, E. 2011, A&A, 532, A146
Li, X., An, T., Mohan, P., & Giroletti, M. 2020, ApJ, 896, 63
Liodakis, I., Blinov, D., Jorstad, S. G., et al. 2020, ApJ, 902, 61
Liodakis, I., Hovatta, T., Huppenkothen, D., et al. 2018, ApJ, 866, 137
Liodakis, I., & Pavlidou, V. 2015, MNRAS, 454, 1767
Liodakis, I., Pavlidou, V., Hovatta, T., et al. 2017a, MNRAS, 467, 4565
Liodakis, I., Zezas, A., Angelakis, E., Hovatta, T., & Pavlidou, V. 2017b, A&A, 602, A104
Liska, M., Hesp, C., Tchekhovskoy, A., et al. 2018, MNRAS, 474, L81
Lister, M. L. 2001, ApJ, 561, 676
Lister, M. L., Aller, M. F., Aller, H. D., et al. 2013, AJ, 146, 120
Lister, M. L., Aller, M. F., Aller, H. D., et al. 2016, AJ, 152, 12
Lister, M. L., Aller, M. F., Aller, H. D., et al. 2018, ApJS, 234, 12
Lister, M. L., Cohen, M. H., Homan, D. C., et al. 2009, AJ, 138, 1874
Lister, M. L., Homan, D. C., Hovatta, T., et al. 2019, ApJ, 874, 43
Lister, M. L., & Marscher, A. P. 1997, ApJ, 476, 572
Lobanov, A. P., & Roland, J. 2005, A&A, 431, 831
Longair, M. S. 2011, High Energy Astrophysics (Cambridge: Cambridge University Press)
Lyubarsky, Y. 2009, ApJ, 698, 1570
MacDonald, N. R., Jorstad, S. G., & Marscher, A. P. 2017, ApJ, 850, 87
MacDonald, N. R., Marscher, A. P., Jorstad, S. G., & Joshi, M. 2015, ApJ, 804, 111
MAGIC Collaboration, Acciari, V. A., Ansoldi, S., et al. 2021, A&A, 647, A163
Mann, H. B., & Whitney, D. R. 1947, Ann. Math. Stat., 18, 50
Marscher, A. P. 1987, in Superluminal Radio Sources, ed. J. A. Zensus & T. J. Pearson (Cambridge: Cambridge University Press), 280
Marscher, A. P. 1990, in Parsec-scale Radio Jets, ed. J. A. Zensus & T. J. Pearson (Cambridge: Cambridge University Press), 236
Marscher, A. P., & Gear, W. K. 1985, ApJ, 298, 114
Marscher, A. P., Jorstad, S. G., Gómez, J.-L., et al. 2002, Natur, 417, 625
Marscher, A. P., Jorstad, S. G., Larionov, V. M., et al. 2010, ApJL, 710, L126
Marti-Vidal, I., Marcaide, J. M., Alberdi, A., & Brunthaler, A. 2013, arXiv:1301.4782
Max-Moerbeck, W., Hovatta, T., Richards, J. L., et al. 2014, MNRAS, 445, 428
McHardy, I. M., Marscher, A. P., Gear, W. K., et al. 1990, MNRAS, 246, 305
Meier, D. L. 2012, Black Hole Astrophysics: The Engine Paradigm (Chichester: Springer-Praxis Publishing)
Mertens, F., Lobanov, A. P., Walker, R. C., & Hardee, P. E. 2016, A&A, 595, A54
Mignone, A., Rossi, P., Bodo, G., Ferrari, A., & Massaglia, S. 2010, MNRAS, 402, 7
Mimica, P., Giannios, D., Metzger, B. D., & Aloy, M. A. 2015, MNRAS, 450, 2824
Moll, R., Spruit, H. C., & Obergaulinger, M. 2008, A&A, 492, 621

Morozova, D. A., Larionov, V. M., Troitsky, I. S., et al. 2014, AJ, 148, 42
Morris, T., Jarvis, C., Cragg, W., et al. 2019, BMJ Open, 9, e030215
Murase, K., Oikonomou, F., & Petropoulou, M. 2018, ApJ, 865, 124
Nagai, H., Haga, T., Giovannini, G., et al. 2014, ApJ, 785, 53
Nakamura, M., Uchida, Y., & Hirose, S. 2001, NewA, 6, 61
Nalewajko, K., Begelman, M. C., & Sikora, M. 2014, ApJ, 789, 161
Nieppola, E., Tornikoski, M., Valtaoja, E., et al. 2011, A&A, 535, A69
O'Sullivan, S. P., & Gabuzda, D. C. 2009, MNRAS, 400, 26
Pacholczyk, A. G. 1970, Radio Astrophysics. Nonthermal Processes in Galactic and Extragalactic Sources (San Francisco, CA: W. H. Freeman)
Pelletier, G., & Roland, J. 1989, A&A, 224, 24
Perucho, M., Kovalev, Y. Y., Lobanov, A. P., Hardee, P. E., & Agudo, I. 2012, ApJ, 749, 55
Planck Collaboration, Aghanim, N., Akrami, Y., et al. 2020, A&A, 641, A6
Pu, H.-Y., Nakamura, M., Hirotani, K., et al. 2015, ApJ, 801, 56
Pushkarev, A. B., Gabuzda, D. C., Vetukhnovskaya, Y. N., & Yakimov, V. E. 2005, MNRAS, 356, 859
Pushkarev, A. B., Kovalev, Y. Y., Lister, M. L., & Savolainen, T. 2009, A&A, 507, L33
Pushkarev, A. B., Kovalev, Y. Y., Lister, M. L., & Savolainen, T. 2017, MNRAS, 468, 4992
Qian, S. J., Britzen, S., Krichbaum, T. P., & Witzel, A. 2019, A&A, 621, A11
Raiteri, C. M., Villata, M., Acosta-Pulido, J. A., et al. 2017, Natur, 552, 374
Raiteri, C. M., Villata, M., Larionov, V. M., et al. 2021, MNRAS, 504, 5629
Readhead, A. C. S. 1994, ApJ, 426, 51
Richards, J. L., Max-Moerbeck, W., Pavlidou, V., et al. 2011, ApJS, 194, 29
Riess, A. G., Macri, L. M., Hoffmann, S. L., et al. 2016, ApJ, 826, 56
Rodrigues, X., Fedynitch, A., Gao, S., Boncioli, D., & Winter, W. 2018, ApJ, 854, 54
Savolainen, T., Wiik, K., Valtaoja, E., Jorstad, S. G., & Marscher, A. P. 2002, A&A, 394, 851
Savolainen, T., Wiik, K., Valtaoja, E., & Tornikoski, M. 2006, A&A, 446, 71

Schmitt, J. H. M. M. 1985, ApJ, 293, 178
Seabold, S., & Perktold, J. 2010, in Proc. 9th Python in Science Conf. 92, http://conference.scipy.org/proceedings/scipy2010/seabold.html
Shepherd, M. C. 1997, in ASP Conf. Ser. 125, Difmap: An Interactive Program for Synthesis Imaging, ed. G. Hunt & H. Payne (San Francisco, CA: ASP), 77
Sobacchi, E., Nättilä, J., & Sironi, L. 2021, MNRAS, 503, 688
Sol, H., Pelletier, G., & Asseo, E. 1989, MNRAS, 237, 411
Stirling, A. M., Cawthorne, T. V., Stevens, J. A., et al. 2003, MNRAS, 341, 405
Tavecchio, F., & Ghisellini, G. 2008, MNRAS, 386, 945
Tavecchio, F., Ghisellini, G., Bonnoli, G., & Ghirlanda, G. 2010, MNRAS, 405, L94
Tchekhovskoy, A., Narayan, R., & McKinney, J. C. 2010, ApJ, 711, 50
Terasranta, H., & Valtaoja, E. 1994, A&A, 283, 51
Urry, C. M., & Padovani, P. 1995, PASP, 107, 803
Valtaoja, E., & Terasranta, H. 1995, A&A, 297, L13
van Moorsel, G., Kemball, A., & Greisen, E. 1996, in ASP Conf. Ser. 101, AIPS Developments in the Nineties, ed. G. H. Jacoby & J. Barnes (San Francisco, CA: ASP), 37
Vermeulen, R. C., & Cohen, M. H. 1994, ApJ, 430, 467
Villata, M., & Raiteri, C. M. 1999, A&A, 347, 30
Vlahakis, N., & Königl, A. 2003, ApJ, 596, 1080
Wardle, J. F. C., Moore, R. L., & Angel, J. R. P. 1984, ApJ, 279, 93
Weaver, Z. R., Balonek, T. J., Jorstad, S. G., et al. 2019, ApJ, 875, 15
Weaver, Z. R., Williamson, K. E., Jorstad, S. G., et al. 2020, ApJ, 900, 137
Wehrle, A. E., Marscher, A. P., Jorstad, S. G., et al. 2012, ApJ, 758, 72
Williamson, K. E., Jorstad, S. G., Marscher, A. P., et al. 2014, ApJ, 789, 135
Xie, W., Lei, W.-H., Zou, Y.-C., et al. 2012, RAA, 12, 817
Yang, S., Yan, D., Zhang, P., Dai, B., & Zhang, L. 2021, ApJ, 907, 105
Zhang, L., Chen, S., Xiao, H., Cai, J., & Fan, J. 2020, ApJ, 897, 10